Edited by
Yannick Champion, Hans-Jörg Fecht

WILEY-VCH

Nano-Architectured and Nanostructured Materials

Fabrication, Control and Properties

EUROMAT
Publications

Nano-Architectured and Nanostructured Materials

Fabrication, Control and Properties

Edited by
Y. Champion and H.-J. Fecht

WILEY-VCH Verlag GmbH & Co. KGaA

Nano-Architectured and Nanostructured Materials

Edited by
Y. Champion and H.-J. Fecht

WILEY-VCH Verlag GmbH & Co. KGaA

DGM
Deutsche Gesellschaft
für Materialkunde e.V.

Euromat is the biennal meeting of the Federation of European Materials Societies (FEMS) constituted by its 24 member societies in Europe. The 2003 meeting took place in Lausanne, Switzerland, and was organised by the French, the German and the Swiss member societies:

Société Française de Métallurgie et de Matériaux (SF2M)
Dezutsche Gesellschaft für Materialkunde (DGM)
Schweizerischer Verband für Materialtechnik (SVMT)

The scientific programme of the EUROMAT 2003 congress was divided into 16 topics that in turn were substructured into 47 symposia. There will be no publication of a complete set of proceedings. The present volume of the Euromat Publication series refers to selected papers of the symposia

Fabrication, Control and Properties of Nano-Architectured Materials (E1)

and

Nanostructured Materials (E4)

Nano-Architectured and Nanostructured Materials

Fabrication, Control and Properties

Edited by
Y. Champion and H.-J. Fecht

WILEY-VCH Verlag GmbH & Co. KGaA

Editors:
Dr. Yannik Champion
Centre d'Etudes de Chimie Métallurgique (CECM)
UPR 2801-CNRS
15, rue Georges Urbain
F-94407 Vittry-sur-Seine
France

Prof. Dr. Hans-Jörg Fecht
Werkstoffe der Elektrotechnik
Universität Ulm
Albert-Einstein-Allee 47
D-89081 Ulm
Germany

Library of Congress Card No.: applied for

British Library Cataloguing-in-Publication Data:
A catalogue record for this book is aailable from the British Library

Bibliografic information published by Die Deutsche Bibliothek
Die Deutsche Bibliothek lists this publication in the Deutsche Nationalbibliografie;
detailed bibliografic data is available in the Internet at <http://dnb.ddb.de>.

ISBN 3-527-31008-8

Composition: W.G.V. Verlagsdienstleistungen GmbH, Weinheim
Printing: betz-druck GmbH, Darmstadt
Bookbinding: J. Schäffer GmbH, Grünstadt

Printed in the Federal Republic of Germany

Preface

Nanotechnology is the creation and utilisation of materials, devices and systems through the control of matter on the nanometer-length scale. This is of great interest for science and engineering since fundamental physical properties change dramatically when the characteristic length scale of a particular property coincides with the structural length scale of the nanostructure of a material. This fundamental behaviour can generally be found for objects with different dimensionalities: 0-D (nanosized clusters), 1-D (nanowires), 2-D (thin-film-multilayers) and 3-D (bulk nanostructures) when the length scale of a microstructure is on the order of a few nanometers.

In all these cases, interfaces and surfaces which separate the different particles, layers and crystalline or non-crystalline domains from each other play the crucial role in controlling the properties and stability of nanostructures. Two effects are critical here:

- The atomic structure of the interface separating two domains and increasing the disorder in a nanostructure and
- Finite size effects of the domains themselves.

These two structural aspects are in general inherently coupled with each other. Thus, it is necessary to develop a fundamental understanding of the correlation between a property and the characteristic length scale of a nanostructure in order to improve a particular property and develop specific applications, such as for example, sensors, actuators, safety systems etc.. Though extremely promising, the use of nano(structured) materials is still marginal because the fabrication of devices remains a challenge.

The table below summarises a few examples regarding the particular property of interest (in alphabetical order), the relevant physical phenomena and possible technological applications.

Size effects in interface controlled nano-architectured and nanostructured materials

Properties	Size dependent phenomena in a nanostructure	Applications
Atomic transport	Interface-to-volume ratio	Sensors, batteries
Electronic	Screening length of an electron	Nanoelectronics
Magnetic	Exchange coupling distance	Magnetic storage
Mechanical	Strain field of a dislocation	High-strength materials
Optical	Electronic band gap	Lasers / Scintillators
Thermodynamic	Surface-to-volume ratio	Hydrogen storage
Tribological	Radius of curvature of the tip	Microsurgical knifes

To attain these special properties, a complex architecture of the materials is generally necessary, obtained through unusual synthesis techniques and specific processing. Complexity stems from the nanometric size and the related surface and grain boundary energies, producing phenomena such as reaction, grain growth, interdiffusion, sintering, coalescence, agglomeration and that the process has to deal with.

This book contains 19 papers, selected from two symposia devoted to the science and engineering of nanomaterials and presented at the Euromat 2003 conference held in Lausanne (1-3 September).

The symposium « Nanostructured Materials » (organised by Hans-Jörg Fecht, Universität Ulm and Forschungszentrum Karlsruhe / Institute of Nanotechnology, Germany) was focused on materials and devices with a characteristic length scale (for example grain or cluster size, thickness of multilayer structures, quantum dots or wires) of less than 100 nanometers. The symposium aimed at reviewing the progress in the field of nanostructured materials and materials for nanotechnologies in terms of their synthesis and processing, as well as their structural, electronic, optical, mechanical, chemical and biological properties and, thus will further promote contact between basic research efforts and technological needs.

More specifically, objectives of the symposium « Fabrication, Control and Properties of Nano-Architectured Materials » (organised by Yannick Champion, CNRS, Vitry-sur Seine, France) were to identify new nanometric architectures that would be of particular interest for applications and the technological route to reach them. Nano-architectures of interest are for optical, electrical, magnetic, mechanical properties and reactivity as well as for specific applications such as catalysis and medical diagnostic and drug delivery. Nano-architectures are metals, alloys, ceramics, semi-conductors, polymers or hybrids inorganic-polymers materials. The symposium placed special emphasis on crucial technical aspects of the fabrication, the control and the characterisation of complex nano-architectures. One session was devoted to the synthesis and properties of carbon nanotubes and Yannick Champion gratefully acknowledges Philippe Poulin, from the Centre de Recherche Paul Pascal (CNRS-Bordeaux) for organising this part of the symposium.

Fields and communities concerned by symposia were: - Synthesis and processing for the fabrication of complex architectures - Properties controlled by the architectures - Characterisation and instruments - Simulation and Modelling. Related aspects were: - exploitation of the new properties of nanomaterials - versatility and ease of adaptation - nanostructure control for optimisation of properties - stability, manufacturing, ageing.

Articles in this book cover main topics discussed during the symposia and bring a good insight of our commitment which is to always produce more outstanding, well controlled and more realistic nano-architectured and nanostructures materials.

The editors wish to thank the authors for their contributions and the publishers for their help in organising the book.

Yannick Champion, Hans-Jörg Fecht

September, 2004

Contents

Multiwall Carbon Nanotubes Produced by Underwater Electric Arc

Zsolt E. Horváth, Lajos Szalmás, Antal A. Koós, Krisztián Kertész, György Radnóczi, László P. Biró
Research Institute for Technical Physics and Materials Science, Hungarian Academy of Sciences, Budapest
Zsolt Kerner
KFKI Atomic Energy Research Institute, Hungarian Academy of Sciences, Budapest
Dóra Méhn, János B.Nagy
Laboratoire de RMN, Facultés Universitaires Notre-Dame de la Paix, Namur

1 Introduction

The submerged arc discharge in liquid media seems to be a cost effective and possibly upscalable method for growth of high quality multiwall carbon nanotubes (MWCNTs) and other nanomaterials. Using liquid nitrogen [1], water [2–8] or aqueous salt solution [2,5] instead of the traditional low pressure neutral gas atmosphere as reaction medium no sealed vacuum chamber is needed, the removal of the product and the replacement of the consumed electrodes is much easier.

In a previous paper [6] we reported an implementation of a continuous MWCNT production method based on underwater AC electric arc. The benefit of AC method compared to DC arc is that there is no deposition on the cathode, the product can be removed from the reaction container by the streaming water if suitable filtration is applied. Computer controlled stepper motors regulated the distance of the electrodes in order to maintain the arc, the voltage between the electrodes was used as feedback signal.

The problem of elimination of the impurities and side products occurs in case of most nanotube production methods. The suitable purification procedures usually depend on the method of nanotube production. High yield, low cost production methods of carbon nanotube raw material have only limited industrial significance if the selectivity can not be achieved or a cheap purification method is not available.

In this contribution we report some further observations on the properties of the underwater AC arc as nanotube synthesis method and the produced carbon nanostructures. Our efforts in purification of the raw material led to conclusions on the limitations of the conventional methods and the possible directions of further optimization of the process.

2 Experimental

An AC electric arc was generated between two identical electrodes submerged in deionised water in a glass vessel. In one case the electrodes were high purity graphite, in other case high purity carbon rods with 6 mm diameter. Two different geometries were compared, one is described in [6], in the other case the electrodes were in one line aligned horizontally. The temperature of the water in the vessel was monitored far from the arc. The arc was stable in the di-

scharge current range of 40–80 A with discharge voltage between 20–24 V. The stability was achieved after an initial period lasting 10–20 minutes depending on the supplied power if we started with room temperature water. Pre-heating the water up to 80 °C the period of initial instability was shortened down to a few minutes. It was possible to keep the apparatus running for 1–2 hours continuously. The current fluctuation was not more than 10 %.

The product was filtered and dried at 100 °C for an hour. The weight of the dried product and the remained pieces of the electrodes was measured.

Three different chemical purification procedures were tried and we made some preliminary experiments for separation of the MWCNTs by sedimentation. Before these treatments, the product powder was carefully ground in agate mortar. The first method of purification was oxidation in flowing air at different temperatures. In the second case, 500 mg powder was dispersed in 100 ml of 1 M H_2SO_4. Then 1.75g $KMnO_4$ was gradually added to the mixture. The solution was boiled for 5 hours then filtered. During the reaction MnO_2 condensed, which was eliminated by dissolution in hydrochloric acid. Finally the sample was washed with distilled water, filtered and dried. Another way to purify the crude sample was the following: 150 mg powder was dispersed in mixed solution of 60 ml H_2SO_4 (98 %) and 40 ml of HNO_3 (70 %). The solution was ultrasonicated then heated and kept at 150 °C and refluxed for 2 and 4 hours in two different experiments, respectively. Then the solution was filtered, the sample was washed with distilled water and dried. For the sedimentation experiments, 20 mg of crude product was added to 50 ml distilled water in a cylindrical glass flask. The flask was sonicated in an ultrasound bath with 70 W power for an hour then left to sediment for 1, 2 and 4 hours in three different experiments, respectively. The upper 2/3 of the suspension was carefully removed by pipette and examined separately.

Crude samples produced with different arc parameters, chemically purified samples and a control sample of the applied graphite electrode were analyzed with a differential thermogravimeter (Luxx NETZSCH STA 409 PC). The measurements were carried out at temperature rate of 2.5 °C/min from 20 °C to 1000 °C in 40 ml/min air and 20 ml/min He mixture flow.

The as prepared, purified and separated samples as well as the material of the graphite and carbon electrodes after grinding were characterized by Transmission Electron Microscopy (TEM) using a Philips CM 20 (Twin) microscope operating at 200 kV. For TEM investigations the powders were suspended in ethanol by ultrasonication and drop-dried on holey carbon film coated copper grids.

3 Results and Discussion

The TEM study showed no obvious difference in the composition of the material floating on the water surface, suspended in the water and the sediment product. The MWCNTs occur always agglomerated with carbon nano-onions, the so-called bucky onions. These agglomerations of MWCNTs and bucky onions (AMBs) ranging from a few hundred nanometers to several microns are bonded together chemically, presumably due to the presence of extra atomic oxygen and hydrogen in the arc plasma [7] as compared to the conventional arc growth technique. It is highly probable that the formation of agglomerated MWCNTs and nano-onions took place in the same time close to each other. The MWCNTs are well graphitized, closed at the ends with typical outer diameter of 10–35 nm and length of a few microns, however, the outer 1–2 walls are often damaged and they are partly covered with thin disordered material. This can also be

the consequence of the reactive formation ambient. Most of the bucky onions are nearly spherical with more or less polyhedral character; their typical dimensions are in the 20–50 nm range. Some nanoparticles are elongated, showing transitional shape towards MWCNTs. A TEM image of a part of a typical AMB is presented in Figure 1.

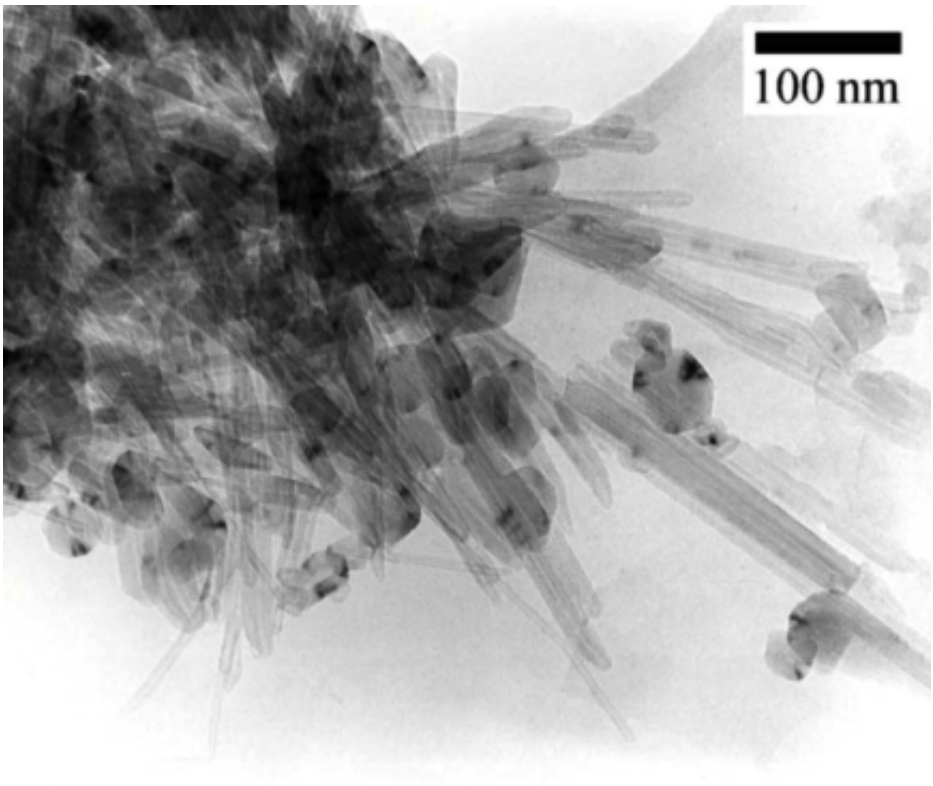

Figure 1: TEM image of an agglomeration of MWCNTs and bucky onions from a sample grown using 40 A arc current

In case of the graphite rods as starting material the samples consist also of graphite flakes with a wide range of dimensions: from a few ten nanometers to several ten microns. There are some clusters of amorphous carbon (soot) present in the samples but their amount is relatively small. While the proportion of MWCNTs and bucky onions in AMBs was found to be nearly constant (50–50 vol%) by TEM observations in all cases, the graphite flake content of the samples depends on the production conditions. Figure 2 shows a TEM image of an area where graphite flakes are dominant. Beyond the dependence on the arc current [6], we found that the instability of the arc leads to increased graphite flake amount. When the growth process was interrupted in the initial, unstable period, the rate of graphite was found as high as 80–90 % in the sample. This fact had raised the idea that graphite flakes were simply crumbled from the electrodes. Comparing the TEM images of the starting graphite electrode material to the underwater

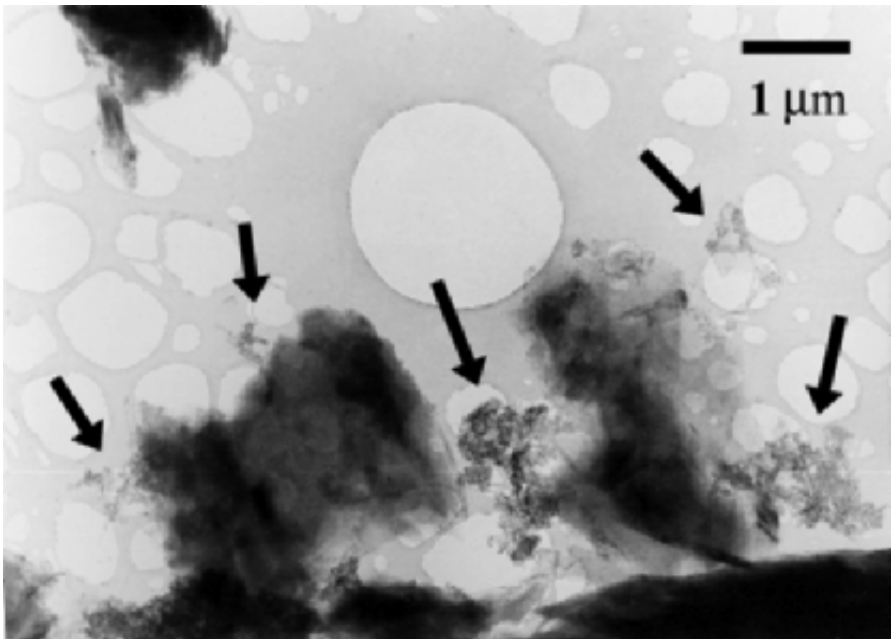

Figure 2: TEM image of an underwater arc grown sample with 60 A arc current made of graphite electrodes. AMBs (agglomerations of MWNTs and bucky onions) are denoted by arrows. The other, bigger objects are graphite flakes. The graphite electrodes contain similar flakes.

arc product samples the graphite flakes seem to be very similar, they are not distinguishable. Using carbon electrodes instead of graphite ones, no such graphite particles occur in the product. However, smaller and larger pieces of the carbon electrode material consisting of disordered carbon forms as well as polyhedral graphitic carbon nanoparticles (see Figure 3) appear in significant amount depending on the process parameters. All these lead to the conclusion that a part of the product can be identified as the fragments of the starting material. Nano-onions similar to the ones presented in figure 3 were reported in the literature as results of arc growth process. To decide the origin of these objects in a safe way, the starting material has to be satisfactorily characterized.

Practically no selectivity of the oxidation in flowing air was found. At lower temperatures, no difference was observed in the rate of the different constituents compared to the initial one. At higher temperatures, when the mass loss was above 50 %, the powder was enriched in graphite grains, the amount and average size of the AMBs gradually decreased. In the last experiment when 1 % of the starting material remained, only graphite flakes were found in the sample. Similarly, no selectivity was found in case of the $H_2SO_4/KMnO_4$ and the H_2SO_4/HNO_3 treatment except that the amorphous carbon was eliminated completely. The very similar chemical character of the graphite, the arc grown MWCNTs and the bucky onions makes these oxidative processes not suitable for proper purification of the corresponding samples. The longer survival time of the graphite can be the consequence of the different grain sizes and the bigger surface area of the AMBs and due to the fact that graphite is the most stable form of carbon under ambi-

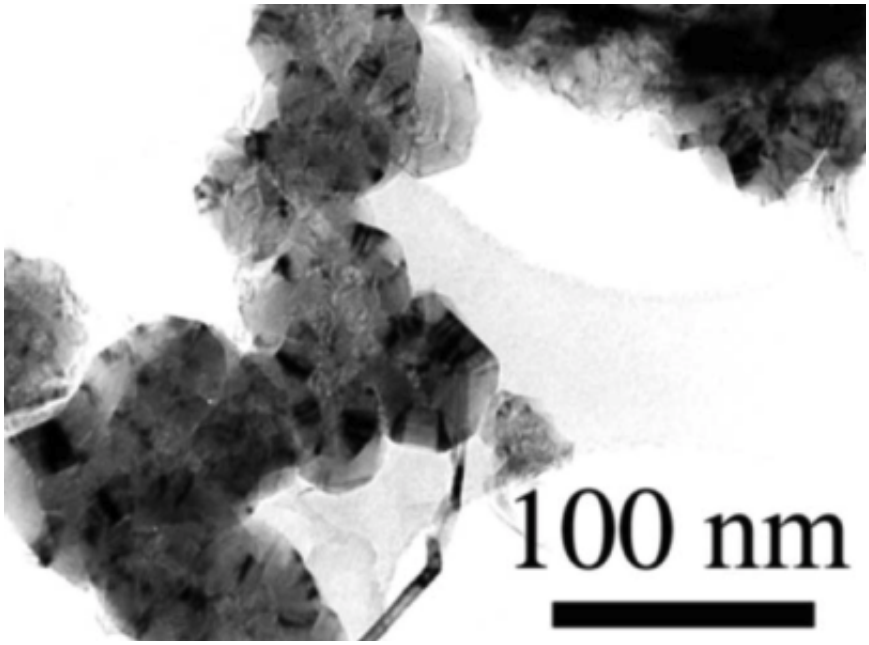

Figure 3: TEM image of the material of the carbon rod used as electrode in the underwater arc nanotube growth experiment. The samples made of this starting material contain similar forms of carbon including polyhedral carbon nano-onions.

ent conditions. The oxidation of the largest graphite pieces several ten microns in diameter takes longer time as compared with the MWCNTs.

Some selected results of the Differential Thermo-gravimetry measurements are presented in Figure 4. Spectra of the applied graphite electrode, an as prepared sample (arc current: 40 A), the same sample after H_2SO_4 / HNO_3 treatment for 2 hours and, as comparison, a catalytic, purified MCWNT sample (see details of production in [9]) are shown. It is obvious that the oxidation properties of the as prepared sample and the graphite electrode are very similar. Their oxidation takes place between 600 and 830 °C. The acidic treatment makes no significant changes; the slight shift of the peak to lower temperatures can be the consequence of some surface effects and/or the decrease of the particle size. The similarity of the chemical character of the as prepared sample and the graphite electrode can be related to the different behavior of the catalytically grown nanotube sample, the oxidation of which completely finishes below 600 °C.

Sedimentation experiments showed the possibility of separating the particles of the sample by their size. Most of the biggest graphite flakes situated in the lower part of the suspension even after the shortest 1 hour time of sedimentation. However, most of the big AMBs, containing considerable part of the produced MWCNTs were also in this fraction. Effective decrease of the graphite content of the sample by sedimentation can be achieved only if the big AMBs can be broken up to much smaller pieces. A suitable way of this can be the chemical elimination of the functional groups responsible for the binding of the agglomerates and/or a more powerful ultrasonication.

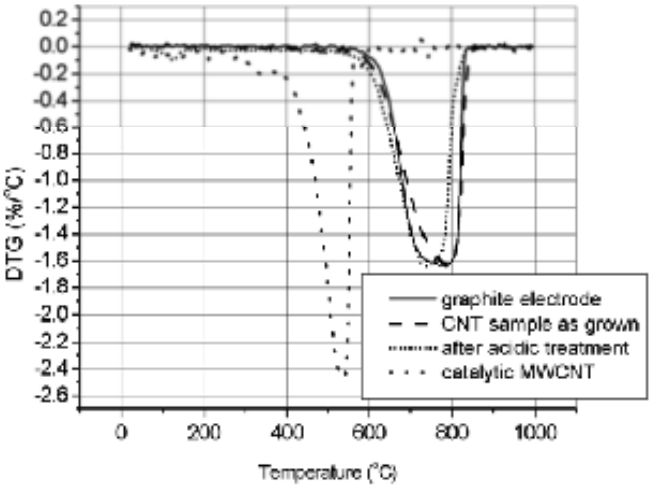

Figure 4: Differential Thermogravimetry curves of the applied graphite electrode, the as prepared sample (arc current: 40 A), the same sample after H_2SO_4 / HNO_3 treatment for 2 hours and, as comparison, a catalytic, purified MCWNT sample

4 Conclusion

The underwater AC arc discharge was demonstrated to be a cost effective and possibly up-scalable method for growth of high quality multiwall carbon nanotubes. However, side products and impurities like polyhedral carbon nano-onions, amorphous carbon and the material of the starting electrodes occur always in the samples. Nano-onions grow together with the MWCNTs, but the material crumbled from the electrodes can contain other nano-objects. This makes the proper characterization of the starting material necessary for the correct understanding of the processes.

Oxidative methods of the crude nanotube material purification are unsuccessful because of the very similar chemical behavior of the MWCNTs and the impurities, sedimentation fails because most of the MWCNTs are in big and strongly bonded agglomerates. The combination of chemical and physical treatments can be the way of producing high purity MWCNT material.

5 Acknowledgement

This work was supported by Hungarian OTKA grant T043685. Krisztián Kertész acknowledges the financial support provided through the European Community's Human Potential Programme under contract HPRN-CT-2002-00209, (Fullmat).

6 References

[1] M. Ishigami, J. Cumings, A. Zettl, S. Chen, Chem. Phys. Lett. 2000, 319, 457–459

[2] Y. L. Hsin, K. Ch. Hwang, F. R. Chen, J.J. Kai, Adv. Mater. 2001, 13, 830–833

[3] N. Sano, H. Wang, M. Chhowalla, I. Alexandrou, G. A. J. Amaratunga, Nature 2001, 414, 506–507

[4] N. Sano, H. Wang, I. Alexandrou, M. Chhowalla, K. B. K. Teo, G. A. J. Amaratunga, K. Iimura, J. Appl. Phys. 2002, 92, 2783–2788

[5] H. W. Zhu, X. S. Li, B. Jiang, C. L. Xu, Y. F. Zhu, D. H. Wu, X. H. Chen, Chem. Phys. Lett. 2002, 366, 664–669

[6] L. P. Biró, Z. E. Horváth, L. Szalmás, K. Kertész, F. Wéber, G. Juhász, G. Radnóczi, J. Gyulai, Chem. Phys. Lett. 2003, 372, 399–402

[7] H. Lange, M. Sioda, A. Huczko, Y. Q. Zhu, H. W. Kroto, D. R. M. Walton, Carbon 2003, 41, 1617–1623

[8] N. Sano, M. Naito, M. Chhowalla, T. Kikuchi, S. Matsuda, K. Iimura, H. Wang, T. Kanki, G. A. J. Amaratunga, Chem. Phys. Lett. 2003, 378, 29–34

[9] A. Fonseca, K. Hernadi, P. Piedigrosso, J.-F. Colomer, K. Mukhopadhyay, R. Doome, S. Lazarescu, L. P. Biró, Ph. Lambin, P. A. Thiry, D. Bernaerts, J. B.Nagy, Appl. Phys. A 1998, 67, 11–22

Synthesis of Polyaniline Nanotubes in the Channels of Anodic Alumina Membrane

S. M. Yang, K. H. Chen and Y. F. Yang
Department of Chemical and Materials Engineering, National Central University, Chung-Li, Taiwan

1 Introduction

Recently, there is a considerable interest in nanoscale materials, since they are expected to possess unique properties. These properties lead to wide range application to variety of areas including chemistry, physics, electronics, optics, material science and biomedical sciences. Nanotubes and nanowires of conducting polymer are interesting due to the potential application for nano-electronic device and biosensers [1]. Conducting polymer nanotubes synthesized by template method and template free methods were reported in the literature [2–14]. Martin et al. [2–6] have synthesized polypyrole, polythiophene and polyaniline by using commercial particle track-etched (PTM) polycarbonate membranes and anodic alumina membranes as templates. They reported that oxidative polymerization of aniline in the pore of PC particle track-etched membrane by sodium vanadate form more uniform tubes than using ammonia persulfate as the oxidant [6]. By controlling the polymerization time they can obtain hollow polypyrrole tubules or solid fibrils, but only hollow polyaniline tubules can be obtained even at long polymerization time. Previous results show enhancements in conductivity were obtained for polypyrrole, poly(3-methylthiophene), polyacetylene and polyaniline synthesized in PC membrance. Polarized infrared absorption spectroscopy results show that the polymer deposited directly on the pore wall is highly ordered relative to subsequently deposited polymer [15]. Demoustier-Champagne et al. reported the chemical and electrochemical synthesis of polyaniline nano-tubules in particle tract-etched PC membrance [10]. The conductivity increases sharply when the diameter of the nano-tubules decreases below 100 nm. Most of the previous works are reported on the synthesis of conducting polymer in the channels of PC membranes. No comparison between the nano-tubules formed in different templates. In this study, we report the synthesis of polyaniline nano-tubules in anodic alumina membrane and particle track-etched PC membrane by chemical and electrochemical method. We also study the degree of delocalization of polarons in nano-tubules of different sizes by electron paramagnetic resonance spectroscopy (EPR).

2 Experimental

2.1 Synthesis of Anodic Alumina Membrane

Synthesis procedure is similar to Masuda's two-step anodizing process. Aluminum foil (99.99 %~99.999 %) was annealed at 500 °C for 4 hours and was then rinsed with acetone or methanol to clean the surface. In the first step, the aluminum foil was anodizing at 40V at 17 °C for 5 hours in a solution containing 0.3 M oxalic acid. The product was immersed in 6 % phosphoric acid at 50 °C for 2 hours to remove the alumina layer. In the second step, the aluminum

foil was then anodizing at 60 V at 17 °C for 5 hours. Saturated mercury (II) chloride solution was used to remove the barrier layer and alumina membrane was immersed in 6 % phosphoric acid at 30 °C for 1.5 hours for pore widening. Alumina membrane of 60 nm pores can be obtained by the above condition. Alumina membrane of 200 nm was purchased from Whatman under the trade name Anodisc^{TM} 13 which is 13 mm diameter and 60 ìm thickness with 200 nm pore diameter.

Polycarbonate membranes of pore diameter 200 nm, 100 nm and 50 nm were obtained from Whatman.

2.2 Synthesis of Polyaniline in the Templates

Polyaniline synthesized by chemical method was obtained by immersing the membrane in 100 mL 1M HCl containing 0.03 mol aniline (purified by distillation over Zn powder). After stirring for 20 min., 0.01 mol ammonia peroxydisulfate (APS) was added and stirred for 3 hours. Remove the membrane and rinse the membrane several times with distilled water. Anodic alumina membrane was removed by dissolving in 6M NaOH. Polycarbonate membrane was removed by dissolving in dichlomethane. The product was dried at 60 °C under vacuum.

Electrochemical synthesis was performed by attaching the membrane to a Pt electrode with a little bit of Ag paste, another Pt electrode was used as the counter electrode and Ag/AgCl was used as the reference electrode. The electrolysis solution contains 0.3 M annilinium ions in 1 M HCl. A voltage of 0.7 V was applied. After the electrochemical synthesis, the electrode was rinsed with distilled water and was immersed in acetone to remove the membrane from the electrode.

2.3 Characterization

The products are characterized by FE SEM (Hitachi S-800), TEM (Jeol JEM-2000 FXII), FTIR, and EPR (Bruker ER 200D-SRC).

2.4 Conductivity Measurement

Conductivity measurement follows the procedure reported previously. Two-probe method is used. After polishing off most of the polyaniline synthesized outside the channel, a thin layer of polyaniline (less than 100 nm) is left for the electric contact. After washing with deionized water and acetone, the sample is redoped with 1M HCl. After drying at 60 °C in a vacuum oven, the sample was put on a flat Pt sheet. Two probes are connected to the Pt sheet and the sample and 0.3 V dc voltage is applied, the current is measured. The conductivity of the template itself is negligible. $1/R = n/R_{i,}$ where R_i is the resistance of a single tube, n is the number of tubes in measured area. The conductivity is calculated from $\sigma = L/ R_i\delta[(\Phi_o^2 - \Phi_1^2)/4]$, where L is the thickness of the template, Φ_o and Φ_1 is the outer and inner diameter of the pore measured from SEM photographs.

3 Results and Discussion

3.1 Morphology

SEM photographs of polyaniline synthesized in commercial anodic alumina membrane of 200 nm pore diameter by chemical methods are show in figure 1. Broken tubes are observed in the photograph of large magnification. On the other hand polyaniline tubes synthesized by electrochemical method show better morphology as indicated in figure 2. SEM photographs of self-made alumina membrane are shown in figure 3. Uniform pores of 60 nm diameter in hexagonal arrangement are observed. The pore density is around 10^{10} pores/cm^2. Polyaniline synthesized inside the channels of self-made alumina membrane are shown in figure 4. Better tubes (or wire) are observed by electrochemical synthesis. TEM photographs of polyaniline tubes synthesized in 200nm alumina membrane show tubular structure, but those synthesized in 60 nm alumina template show rod-like structure as shown in figure 5.

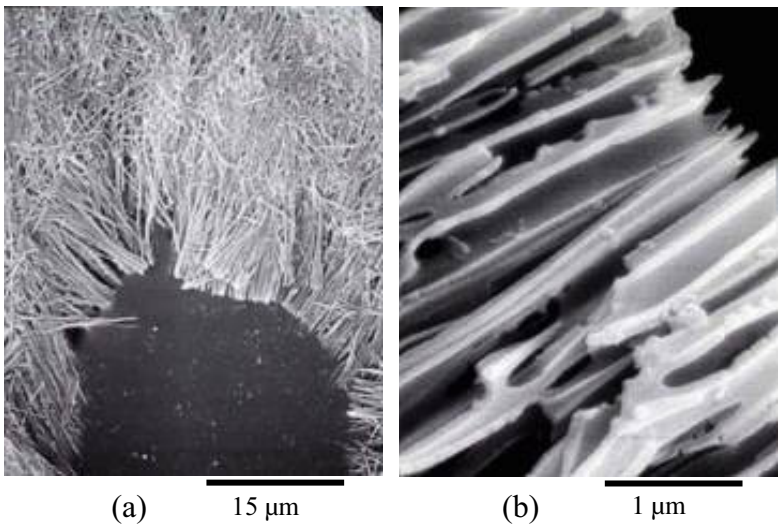

Figure 1: SEM photographs of polyaniline formed in 200 nm anodic alumina membrane by chemical method

Polyaniline tubes synthesized electrochemically in PC PTM of pore diameters of 200 nm, 100 nm and 50 nm are shown in figure 6. Similar to the results reported previously that tubes of cigar shape are formed with smaller diameter ends and larger diameter in the middle part. Stripes are also found on the wall of the tube. These irregularities of the tube shape came from the channel of commercial polycarbonate PTM membranes. Sections of polyaniline were formed from chemical synthesis.

Comparison of the polyaniline synthesized in alumina membrane and polycarbonate PTM membrane of similar pore diameter show better morphology are obtained for those synthesized in alumina membrane.

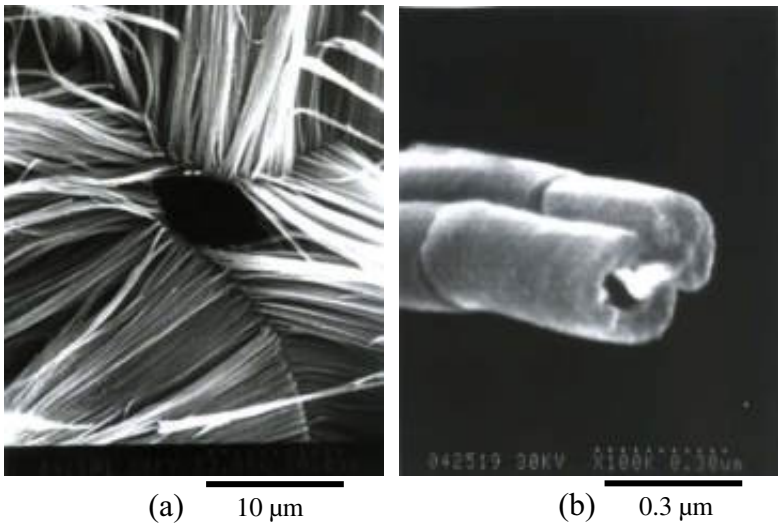

Figure 2: SEM photographs of polyaniline formed in 200 nm anodic alumina membrane by electrochemical method

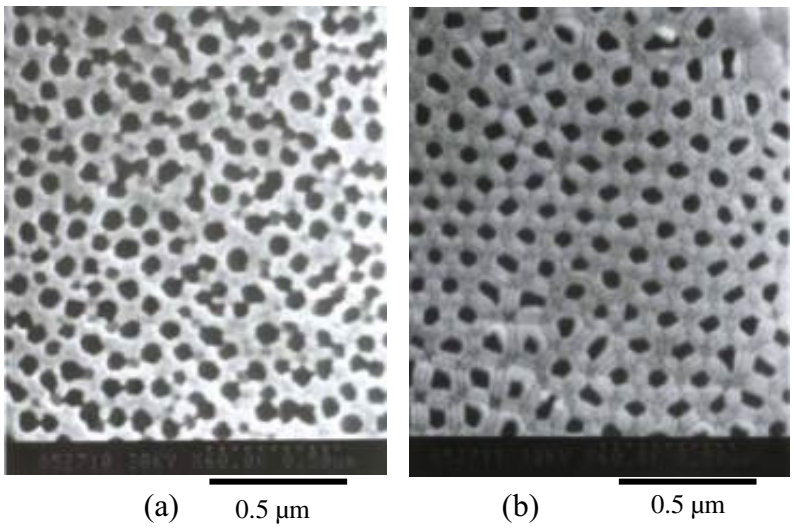

Figure 3: SEM photographs of self-made alumina membrane, (a) side in contact with solution, (b) side in contact with electrode

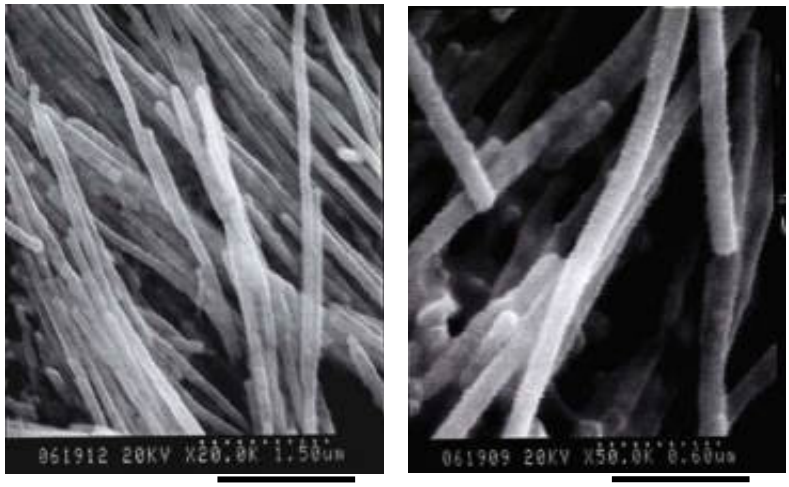

Figure 4: SEM photographs of polyaniline formed in 60 nm self-made anodic alumina membrane by electrochemical method

Figure 5: TEM photographs of polyaniline formed in (a) 200 nm commercial, and (b) 60 nm self-made anodic alumina membrane by electrochemical method

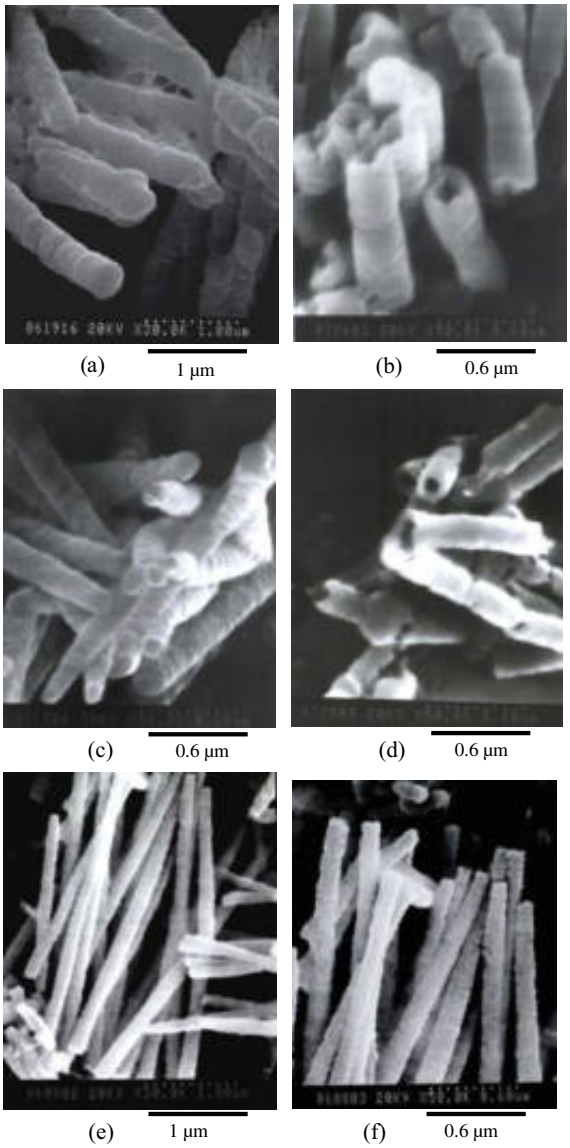

Figure 6: SEM photographs of polyaniline formed in (a) (b) 200 nm, (c) (d) 100 nm, (e) (f) 50 nm polycarbonate particle track etched membranes by electrochemical method

3.2 Structure

FTIR spectra of polyaniline synthesized chemically or electrochemically in anodic alumina membrane all show the structure of emeraldine salts. The sample synthesized electrochemically

for 6000 sec show an additional sharp peak at 1380 cm^{-1} but after synthesis for 9600 sec, this peak disappeared. The result indicates that polymerization is not complete after electrochemical synthesis for 6000 sec.

EPR spectra were studied in order to compare the degree of delocalization of polarons. A single peak is observed at g value close to that of free electron for all the samples measured. The peak to peak linewidths and g values of polyaniline tubes by electrochemical synthesis in channels of PC PTM of different pore diameters are shown in table 1. The linewidth decreases with decreasing pore diameter of the template channels. The results indicate better delocalization of polarons in polyaniline chain synthesized in smaller pore channels. More regular conformation of the polymer chain in small pore channel are expected which agrees with the results reported previously by Raman spectra. The linewidth of polyaniline by electrochemical synthesis in 200nm diameter channels of anodic alumina membrane is smaller than those in 200 nm PC PTM membrane. From SEM photographs, more uniform and regular tubes are obtained in anodic alumina membrane than PC PTM. Polyaniline synthesized for 6000 sec show larger linewidth than those synthesized for 9600 sec. FTIR spectra show incomplete polymerization for 6000 sec sample. On the other hand chemical synthesized samples in PC PTM show larger linewidth than those synthesized by electrochemical method as shown in table 2. Segments of polyaniline are obtained by chemical synthesis in PC PTM. In anodic alumina membrane, the difference in linewidth for chemical and electrochemical synthesized samples is small. Although broken tubes are also obtained, but the continuity is much better than those samples in PC PTM. The linewidth of polyaniline tubes is slightly larger than those of bulk material. Polymerization of aniline in a confined channel may result in smaller molecular weight than those in the bulk material.

Table 1: Peak to peak linewidth and g value of polyaniline synthesized electrochemically

	ΔH_{pp} (Gauss)	g value
polyaniline in 200 nm PC PTM	2.398	2.0039
polyaniline in 100 nm PC PTM	2.035	2.0034
polyaniline in 50 nm PC PTM	1.235	2.0032
polyaniline in 200 nm alumina membrane	1.012	2.0037
polyaniline in 60 nm alumina membrane	1.017	2.0035
polyaniline in 200 nm alumina membrane (synthesis for 6000 sec)	1.529	2.0032
polyaniline bulk material	1.09	2.0033

Table 2: Peak to peak linewidth and g value of polyaniline synthesized chemically

	ΔH_{pp} (gauss)	g value
polyaniline in 200 nm PC PTM	5.087	2.0052
polyaniline in 100 nm PC PTM	4.070	2.0047
polyaniline in 50 nm PC PTM	4.100	2.0041
polyaniline in 200 nm alumina membrane	1.526	2.0034
polyaniline bulk material	1.09	2.0038

3.3 Conductivity

The conductivities of polyaniline synthesized as bulk material or in the channels of the templates are listed in table 3. Samples synthesized by electrochemical method in the templates usually show higher conductivity than the bulk material. However, the samples synthesized by chemical method in templates show lower conductivity than the bulk material. The results may come from more uniform tubes are formed by electrochemical method than chemical method. Accurate conductivity measurement is difficult due to the estimation of thickness of the pore wall, pore density, irregularity of the tube shape and two probe method. More accurate measurement of the conductivity is under development.

Table 3: Conductivity of polyaniline

	synthesis method	conductivity (S/cm)
polyaniline in 200 nm alumina membrane	Electrochemical	$1.07 \cdot 10^{-1}$
polyaniline in 200 nm PC PTM	Electrochemical	$9 \cdot 10^{-2}$
polyaniline in 100 nm PC PTM	Electrochemical	$1.04 \cdot 10^{-1}$
polyaniline in 50 nm PC PTM	Electrochemical	$3.3 \cdot 10^{-2}$
polyaniline bulk material	Electrochemical	$5.7 \cdot 10^{-2}$
polyaniline in 200 nm PC PTM	Chemical	$4 \cdot 10^{-2}$
polyaniline in 100 nm PC PTM	Chemical	$1.9 \cdot 10^{-1}$
polyaniline in 50 nm PC PTM	Chemical	$6.8 \cdot 10^{-2}$
polyaniline bulk material	Chemical	$1.49 \cdot 10^{-1}$

4 Acknowledgement

The authors thank the assistance of G. D. Lin and S. J. Ueng from instrumental center, National Central University for SEM and TEM measurements. The financial support from National Science Council, Taiwan under the project NSC 92-2113-M-008-008 is greatly acknowledged.

5 References

[1] (a)A. Kros, S. W. F. M. van Hovell, N. A. J. M. Sommerdijk, R. J. M. Nolte, Adv. Mater. 2001,13,1555–1557
(b) A. Kros, R. J. M. Nolte, N. A. J. M. Sommerdijk, Adv. Mater. 2002,14,1779–1782
[2] C. R. Martin, Science, 1994, 266, 1961–1966
[3] C. R. Martin, Acc. Chem. Res., 1995, 28, 61–68
[4] J. C. Hulteen, C. R. Martin, J. Mater. Chem., 1997, 7, 1075–1087
[5] C. R. Martin, Chem. Mater. 1996, 8, 1739–1746
[6] R. V. Parthasarathy, C. R. Martin, Chem. Mater. 1994, 6, 1627–1632
[7] J. Duchet, R. Legras, S. Demoustier-Champagne, Synth. Met. 1998, 98, 113–122
[8] L. Dauginet, A. S. Duwez, R. Legras, S. Demoustier-Champagne, Langmuir, 2001, 17, 3952–3957

[9] J. L. Duvail, P. Retho, S. Garreau, G. Louarn, C. Godon, S. Demoustier-Champagne, Synth. Met. 2002, 131, 123–128
[10] M. Delvaux, J. Duchet, P-Y Stavaux, R. Legras, S. Demoustier-Champagne, Synth. Met. 2000, 113, 275–280
[11] S. Demoustier-Champagne, P-Y Stavaux, Chem. Mater. 1999, 11, 829–834
[12] S. Demoustier-Champagne, E. Ferain, C. Jerome, R. Jerome, R. Legras, Eur. Polym. J. 1998, 34, 1767–1774
[13] M. Fu, Y. Zhu, R. Tan, G. Shi, Adv. Mater. 2001, 13, 1874–1877
[14] (a) H. Qiu, M. Wan, B. Mattews, L. Dai, Macromol. 2001, 34, 675–677
(b) Z. Wei, Z. Zhang, M. Wan, Langmuir, 2002, 18, 917–921
[15] (a) Z. Cai, J. Lei, W. Liang, V. Menon, C. R. Martin, Chem. Mater. 1991,3,960–967
(b) V. P. Menon, J. Lei, C. R. Martin, Chem. Mater. 1996, 8, 2382–2390

Electrical Properties of Single-Walled Carbon Nanotube Fiber under Electron Irradiation

Cs. Mikó, M. Milas, J.W.Seo, E. Couteau, N. Barišiæ, R. Gaál, L. Forró
Institute of Physics of Complex Matter, Ecole Polytechnique Fédérale de Lausanne, Lausanne, Switzerland

1 Introduction

Carbon nanotubes have allured much attention because of their unique physical properties. In the last decade, literature has reported considerable progress in the large-scale synthesis [1–3] as well as the purification of CNTs using different techniques. In order to exploit their feasible application, one of the major challenges is the processing of CNTs on macroscopic scale, for instance into a macroscopic fiber.

For an individual single-walled carbon nanotubes an exceptionally high Young's modulus has been demonstrated both in theory and in experiments; therefore, the CNT-based composite materials are expected to have extraordinary mechanical properties as well. Unfortunately the single-walled nanotubes (SWNTs) preferentially form bundles, where tubes interact via van der Waals force, and therefore easily slide along their axis. Hence, the mechanical strength of a macroscopic SWNT fiber is dominated by their shear modulus and not by their Young's modulus, accordingly not as high as expected.

Recently, it has been demonstrated that electron beam irradiation can create covalent bonds between surfaces of SWNTs [4] just as cross-linked CNTs within SWNTs rope resulting in a considerable increase of Young's modulus.

Kis et al. [5] pointed out that both 80 and 200 kV beam energy could displace carbon atoms, and induce cross-links between the single CNTs, enhancing the shear modulus for low electron irradiation dose.

In this contribution, we report on effect of electron irradiation on electrical properties of macroscopic fibers consisting of SWNTs. From electrical point of view, CNT can show either semiconducting or metallic behavior depending on their chirality's. Ropes of SWNTs assembled to a macroscopic fiber show semiconducting properties due to the predominant presence of semiconducting nanotubes (≈ 70 %). As single CNTs are much shorter than the contact electrodes on the fiber it can be considered as random resistor network of many weakly connected nanotubes.

2 Experimental Details

SWNT bundles were assembled to a macroscopic fiber according to Gommans et al. [6] For *in-situ* transport measurements, a sample of 3 mm length was cut from a long rope and mounted on a TEM Cu ring with four gold electrodes, which were glued by conducting silver paint and electrically isolated from the supporting Cu ring by mica. This configuration enabled the *in situ* measurement of the resistance in a TEM (Hitachi TE 700 operating at 200 kV) during irradiati-

on as well as ex situ measurements by interrupting the irradiation and placing the sample in a He cryostat for resistivity vs temperature measurements in the 4.2–300 K temperature range.

The irradiation was carried out for approximately 29 h at a constant electron flux of about $2.4 \cdot 10^{13}$ electrons cm^{-2} s^{-1}. In order to avoid long exposure time, the incident beam was focused to a diameter of 15 μm, increasing the flux to $2 \cdot 10^{16}$ electrons cm^{-2} s^{-1}, and this spot was moved step by step along the fiber between the two center electric contacts.

3 Results and Discussion

Our result of the in-situ measurement is shown in figure 1, presenting the resistivity of the SWNT fiber vs irradiation time.

Before the irradiation the ropes had a typical 4-probe resistivity of 0.2 Ωcm ± 0.08 Ωcm, which agrees with Vigolo et al [7]. At the beginning, the resistivity fell approximately to 0.07 Ωcm ± 0.02 Ωcm and reached a minimum after about 35 minutes of irradiation time. Past this minimum, the resistivity increased linearly with the irradiation time with a slope of about 1.15 Ω/min. This dependence remained the same for many hours. We focused then the beam to a 15-micron diameter spot and irradiated each part until the resistivity saturated, then we moved to a neighboring section along the fiber axis. This gives rise to the step-like time dependence shown in figure 1.

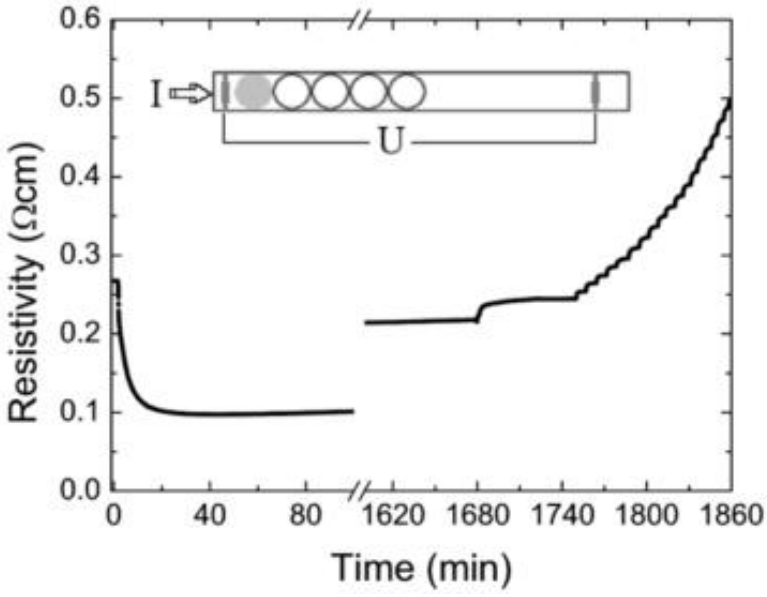

Figure 1: The resistivity of a SWNT fiber as function of electron irradiation time. The schematic drawing in the inset shows the contact arrangement and the irradiated spot size with respect to sample dimensions. The step-like variation towards the end of the irradiation is the result of the stepwise moving of the irradiated zone along the sample.

Besides measuring the resistivity during irradiation, we measured the resistance as function of temperature before the irradiation, at the minimum resistivity point and after the irradiation. Figure 2 shows these three curves. As it can be seen, except for the magnitude of the resistance, there is no significant change in their behavior.

The temperature dependence of the resistivity is well described by $\rho \propto \exp(T_0/T)^{1/2}$ indicating Coulomb-repulsion limited hopping conduction like in many granular carbon materials [8].

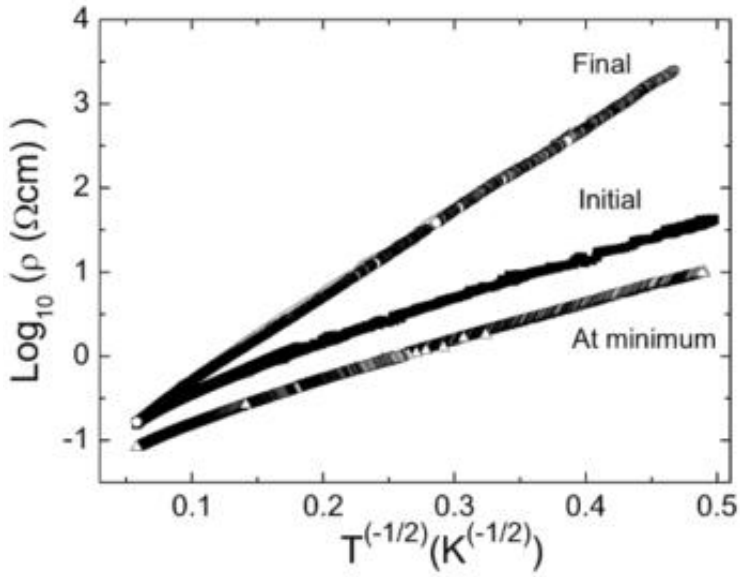

Figure 2: The resistivity of pristine and irradiated nanotubes as a function of temperature. The temperature dependence indicates hopping like conduction.

The results of the measurements can be explained as follows. The electron irradiation creates displacements of the carbon atoms in nanotubes, leading to very reactive broken chemical bonds. This has a two-fold effect on the resistivity: one process is the cross-linking of nanotubes in a bundle, improving its electric conductivity by decreasing the individual tube-tube distance. The other effect however is the damage of the graphite layer by these point defects, increasing the resistivity with increasing incident electron as well as defect concentration. This increase is linear at the beginning, but it gets saturated when the system is completely transformed into amorphous carbon. Consequently, for low damage level, the creation of covalent bonds between two nanotubes dominates and leads to an improvement in the conductivity while the point defects have little effect on the on-tube conduction.

4 Summary

We carried out *in-situ* resistivity measurements on macroscopic oriented ropes of single wall carbon nanotubes in a transmission electron microscope.

Our results suggest that the cross-links created by electron irradiation also change the electronic conductivity of the fiber significantly yielding a dramatic decrease of the resistance. As electron irradiation continues, the irradiation is destructive to the CNT wall structure and leads to an increase of the resistance.

5 References

[1] S. Iijima, Mater. Sci. Engin. B 1993, 19, 172
[2] C. Journet, W. K. Maser, P. Bernier, A. Loiseau, M. L. Delachapelle, S. Lefrant, P. Deniard, R. Lee, J. E. Fischer, Nature 1997, 388, 756
[3] K. Hernadi, A. Fonseca, P. Piedigrosso, M. Delvaux, J. B. Nagy, D. Bernaerts, J. Riga, Catalysis Letters 1997 48, 229
[4] B. Smith and D. E. Luzzi, J. Appl. Phys. 2001, 90, 3509
[5] A. Kis, J.-P. Salvetat, Thien-Nga Lee, E. Ljubovic, A. Kulik, W. Benoit, J. Brugger, L. Forro, accepted to Nature
[6] H. H. Gommans, J. W. Alledredge, H. Tashiro, J. Park, J. Magnuson, G. A. Rinzler, J. Appl. Phys 2000, 88, 2509
[7] B. Vigolo, A. Penicaud, C. Coulon, C. Sauder, R. Pailler, C. Journet, P. Bernier, P. Poulin, Science, 2000, 290, 1331
[8] A. W. P. Fung, Z. H. Wang, M. S. Dresselhaus, G. Dresselhaus, R. W. Pekala, M. Endo, Phys. Rev. B 1994, 49, 17325

Localization of Charge Carriers and Magneto-Transport in Nanocomposites based on Carbon Nanotubes

O. Chauvet [1], J.M. Benoit [2], B. Corraze [1]
[1] Institut des Materiaux Jean Rouxel, Nantes, France
[2] Max Planck Institute, Stuttgart, Germany

1 Abstract

In this paper, we investigate the transport and magneto-transport properties of polymethylmetacrylate/singlewalled carbon nanotubes nanocomposite thin films. Intrinsic localization of the charge carriers at the bundle size is evidenced from the conductivity measurements. Magnetoresistance measurements reveal two different regimes which depends on the temperature and on the field range. The analysis of the data confirms that the localization length is about 7 nm.

2 Introduction

Singlewalled carbon nanotubes (SWNT) are nanomaterials which possess remarkable physicochemical properties thanks to their nanometric size. The potential application field of these nanosystems is very broad, ranging from nanodevices to MEMS, actuators or sensors, chemical reactors… Still most of the practical sensing applications will involve an ensemble of SWNT rather than isolated nano-objects. To understand the evolution of the properties when putting the SWNT together is thus essential. This is the purpose of this paper in which we investigate the electrical transport and magneto-transport properties of an ensemble of SWNT embedded into an insulating polymer matrix in order to build a nanocomposite.

3 Experimental

The SWNT have been obtained by arc discharge [1]. Transmission electron microscopy shows that they are of high quality with an average diameter close to 1.3 nm and a typical bundle size between 7 and 10 nm. They have been ultrasonically dispersed with polymethylmetacrylate (PMMA) in toluene. The nanocomposite 10 µm thick films are formed by drop casting the solution onto a glass plate. Composites with a SWNT volume fraction f = 0.1–8 % have thus been obtained. All the electrical measurements (resistivity, magneto-resistance, non linear field effects) have been performed within a planar four probe configuration with gold evaporated electrodes. Non linear $I(V)$ characteristics have been obtained with a standard pulse technique in order to avoid self-heating.

4 Electrical Conductivity and Transport Mechanism

The temperature dependence of the electrical conductivity $\sigma(T)$ of three different samples (f = 0.4, 0.9 and 4 % respectively) is shown in Fig. 1(a) as solid lines. Indeed, it is found that the room temperature conductivity strongly depends on the SWNT content. In Ref. 2, we show that it follows a critical percolation behavior with a percolation threshold $f_c = 0.33 \pm 0.03$ %. Here, only three examples are shown.

It is clear from Fig. 1(a) that the conductivity σ is not metallic like. Actually, it follows a hopping law $\sigma \alpha \exp[-(T_0 / T)^{1/2}]$ at low temperature which means that conduction occurs by hopping in presence of Coulomb interactions [3]. It suggests that the charge carriers are strongly localized on a length ξ in the nanocomposites. The T_0 characteristic temperature increases from 200 to 1000 K when f decreases from 8 % to 1 %, then it saturates for lower f values. It is possible to extract the localization length from the T_0 parameter and by using the effective density of states of the SWNT. $\xi \sim 7$ nm is found whatever the SWNT content (i.e. whatever the sample) [4]. It shows that localization does not depend on the tube tube contact distance (and thus on f) as it might have been expected. Conversely, it suggests that localization is intrinsic to the SWNT conducting network.

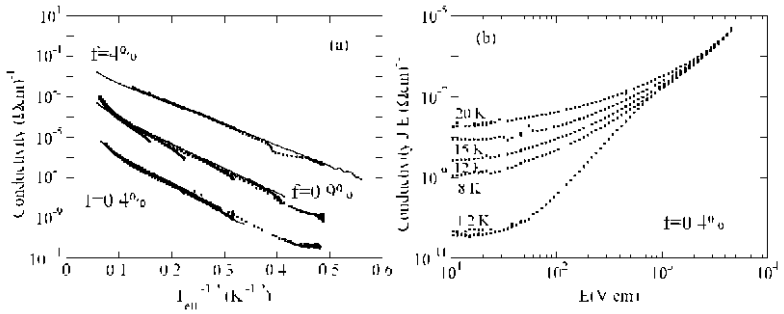

Figure 1: (a) Ohmic conductivity σ (lines) and (isothermal) non ohmic conductivity J/E (dots) versus $T_{\text{eff}}^{-1/2}$ for the samples f = 0.4, 0.9, 4 %. For the ohmic conductivity curves, $T_{\text{eff}} = T$ is the thermal bath temperature while for the non ohmic conductivity curves, $T_{\text{eff}} = T + \beta E$ is the effective temperature (see text). **(b)** Non linear conductivity J/E versus electric field E characteristics of the f = 0.4 % sample at T = 4.2, 8, 12, 15 and 20 K respectively.

The intrinsic character of the localization length is confirmed by the non linear $I(V)$ isothermal characteristics of the composites. An example of these characteristics at T = 4.2, 8, 12, 15 and 20 K is shown in Fig. 1(b) for the f = 0.4 % sample where the conductivity J / E (J the current density, E the electric field) is shown to increase by up to 5 orders of magnitude when the electric field increases from 10 to 6000 V/cm. The same kind of isothermal characteristics are obtained at T = 4.2, 6, 10, 20 and 40 K for sample f = 0.9 % and at T = 4.2, 10, 20 and 40 K for sample f = 4 % respectively.

In Ref. 4, we suggest that the non linearities originate from a redistribution of the (localized) conduction electrons energy induced by the electric field. Such an effect is analog to a thermal effect if one defines an electrical temperature $T_{\text{el}} = \beta E = \gamma \xi E / k_B$ where γ is a numerical parameter close to 1, k_B the Boltzmann constant. At finite temperature and large electric field, in-

stead of the thermal bath temperature we should consider an *effective temperature* [5] for which the simplest expression is given by:

$$T_{\text{eff}} = T + T_{\text{el}} = T + \beta E = T + \gamma \xi E / k_{\text{B}} \tag{1}$$

A fit of the curves of Fig. 1(b) gives $\beta = 0.035$ K.cm/V for all the investigated temperatures. Since β depends only on the localization length ξ which was found to be intrinsic to the SWNT network, we plot all the ohmic conductivity curves $\sigma(T_{\text{eff}} = T)$ and the non ohmic isothermal characteristics J / E ($T_{\text{eff}} = T + \beta E$) versus $T_{\text{eff}}{}^{-1/2}$ with a fixed value of $\beta = 0.035$ K.cm/V in Fig. 1(a). For a given sample, all the curves merge into a single one which accounts for the validity of the effective temperature model. The fact that a unique β parameter allows to do this confirms that the localization length is independent of the SWNT content. The linearity of the curves shows also that conduction occurs by hopping in presence of Coulomb interactions even in the non ohmic regime. The Coulomb interactions likely come from the Coulomb charging energy which is required to transfer a charge from a SWNT bundle to another in the transport process. This charging effect is progressively screened when the amount of SWNT increases which accounts for the decreases of T_0 when f increases [4]. From $\beta = 0.035$ K.cm/V, a localization length $\xi \sim 25$ nm is extracted with $\gamma = 1$. This value is three times bigger but still of same order of magnitude than the length which is extracted from the $\sigma(T)$ dependencies.

5 Magnetotransport and Localization

Magnetoresistance (MR) in the strongly localized regime can provide an independent estimate of the localization length. Above 10 K, the magnetoresistance $R(H) / R$ ($H = 0$) is essentially negative and small in the magnetic field range $H = 0$–12 T as shown in Fig.2 for samples $f = 4$ % and $f = 8$ % where $R(H)$ is the sample resistance at field H. Above 40 K, the MR is quadratic in field with a maximum effect of 2–2.5 % at 40 K and 12 T. In the 10–40 K temperature range, the MR is negative and linear in field up to a characteristic field H_{m} (arrows in Fig. 2) above which it becomes positive.

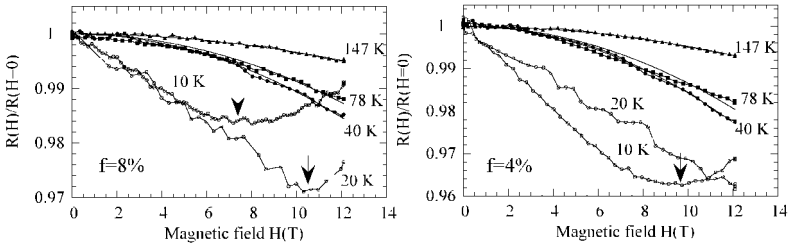

Figure 2: Magnetoresistance $R(H) / R(H = 0)$ versus magnetic field H for the samples $f = 8$ % (left pannel) and $f = 4$ % (right pannel) between 10 K and 147 K. $R(H)$ is the sample resistance at field H. The arrows indicate the field H_{m} above which a positive contribution to the MR sets in. The solid lines correspond to a quadratic dependence of the MR with the field.

A negative MR is quite usual in strongly localized hopping systems. It is due to the partial destruction of the quantum interferences which occur along the hopping path due to forward scattering. This phenomenon is the strong localization counterpart of the negative MR observed in weak localization systems. It leads to a linear or quadratic negative MR in absence of spin orbit coupling as found here [6,7]. It is interesting to note that the transition from a linear to a quadratic dependence occurs in a temperature range where the temperature is high enough to wash out the Coulomb interaction effects leading thus to a $\ln(\sigma) \propto T^{-1/4}$ instead of $\ln(\sigma) \propto T^{-1/2}$ temperature dependence.

The maximum negative MR effect is observed when the magnetic flux enclosed in the hopping area scales with the flux quantum ϕ_0 *i.e.* when $H_m \cdot S_{hop} = \phi_0$ where S_{hop} is the hopping area. By making use of the standard formula for S_{hop}, H_m is thus related to the localization length in the Efrös Shklovskii regime through Eq. (2).

$$\xi \sim [\phi_0 (T/T_0)^{3/4} / H_m]^{1/2} \tag{2}$$

Application of Eq. (2) allows to estimate the localization length where the experimental values of T_0 and H_m are obtained from the conductivity curves and from the MR dependencies respectively. The results are listed in Table 1.

Table 1: Localization length of the different samples obtained from the magnetoresistance data

	Temperature	From Eq. 2	From Eq. 3 (ohmic)	From Eq. 3 (non ohmic)
	T = 20 K	8.6 nm		
	T = 10 K	7.8 nm		
f = 8 %	T = 4.2 K		6.3 nm	
	T = 1.5 K		7.2 nm	
f = 4 %	T = 10 K	5.0 nm		
	T = 3.0 K	(T_{eff} = 8.6 K)		4.5 nm
f = 2 %	T = 2.2 K	(T_{eff} = 5.1 K)		4.9 nm
	T = 3.0 K		5.3 nm	
	T = 2.2 K		5.1 nm	

We find ξ values in the range 5-8 nm which corroborates the result obtained from the conductivity measurement. Indeed, Eq. (2) shows also that H_m increases with the temperature. It may explain why we do not observe the negative to positive MR transition in our field range at higher temperatures.

When the magnetic field H exceeds H_m, a positive contribution to the MR becomes visible. This positive MR is easier to observe at low temperature where H_m is smaller and the effect bigger in magnitude. It is shown in Fig. 3 for samples f = 8 % and f = 2 % respectively, where $ln[R(H) / R(0)]$ is plotted versus H^2. The effect reaches 70 % at H = 14 T and T = 1.5 K for sample f = 8 % and 25 % at H = 13 T and T = 2.2 K for sample f = 2 %.

In the strongly localized regime and above H_m such a positive MR may come from the orbit shrinkage induced by the high magnetic field which reduces the transfer from site to site. In the Efrös Shklovskii regime, it results in a positive MR described by [3]:

$$\ln\left[R(H)/R(0)\right] = t_{ES}\frac{\xi^4}{(\hbar/e)^2}\left[\frac{T_0}{T}\right]^{3/2} H^2 \tag{3}$$

with $t_{ES} \sim 0.0015$. In Fig. 3 the linearity of $ln[R(H)/R(0)]$ with H^2 is verified at low H values (thick lines) which suggests that this model is valid. The slope of the linear part gives localization lengths which are reported in Table 1 for both samples in the ohmic regime ($E < 1$ V/cm). Once more, ξ is found to be in the range 5–8 nm.

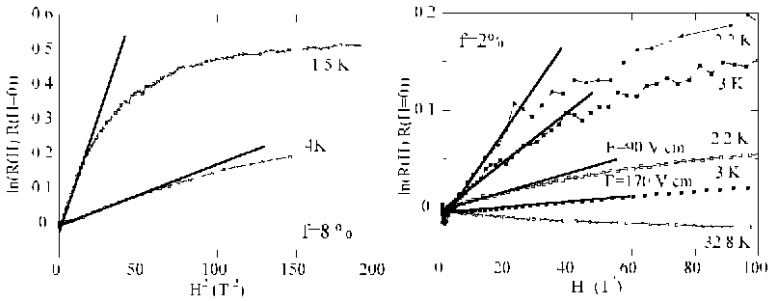

Figure 3: Low temperature magnetoresistance behavior of sample $f = 8$ % (left pannel) and sample $f = 2$ % (right pannel). For the $f = 2$ % sample, the curves with $E = 90$ or 170 V/cm are obtained in the non ohmic regime. It corresponds to an effective temperature of 5.1 and 8.6 K respectively.

We have also tried to investigate the MR behavior in the non ohmic regime. This is shown for sample $f = 2$ % at $T = 2.2$ K and 3 K and for electric field strength of $E = 90$ V/cm and 170 V/cm respectively in Fig. 3. The same behavior is observed with a reduced magnitude which is associated to an effective temperature higher than the thermal bath temperature. The associated effective temperatures are found to be $T_{eff} = 5.1$ K and 8.6 K respectively by extrapolation of the conductivity temperature dependence (Eq. (1) with $\beta = 0.035$ gives 5.3 and 8.9 K). The slope of the linear part of the curves yields $\xi \sim 5$ nm (see Table 1) in agreement with previous results.

6 Conclusion

In this paper, we investigate the electrical transport and magnetotransport properties of nanocomposites SWNT/PMMA thin films. In this nanocomposites, transport occurs by hopping of localized carriers in presence of Coulomb interactions due to the Coulomb charging effect [2, 4]. The analysis of the ohmic conductivity temperature dependence suggests an intrinsic localization on a typical length of 7 nm. The non ohmic behavior confirms the intrinsic localization however the estimated length scale is three times bigger.

Here, we show that the magnetoresistance behavior is in agreement with the strong localization picture. Different regimes are encountered in the magnetoresistance depending on the magnetic field strength and on the temperature. In small fields, a negative and small MR is

encountered which is attributed to the partial destruction of the quantum interferences occuring along the hopping path. This negative MR saturates when the magnetic flux enclosed into the hopping area scales with the flux quantum. In higher field, orbit shrinkage occurs which induces a positive MR. These two regimes yields a typical localization length in the range of 5–8 nm.

An interesting point is the intrinsic character of the localization which is found to be independent of the SWNT volume fraction into the nanonomposite. Since the localization length is comparable to the typical bundle size, we suggest that localization occurs at the bundle boundaries. Indeed, it suggest as well that transport along the bundle is not limiting. It may reveal the ballistic nature of the charge transport in the SWNT.

7 Acknowledgements

We acknowledge P. Bernier for providing us with the SWNT. This work was partly supported by the EEC COMELCAN HPRN-CT-2000-00128 contract.

8 References

[1] C. Journet et al., Nature 1997, 388, 756
[2] O. Chauvet, J.M. Benoit, B. Corraze, to appear in Carbon 2004
[3] B.I. Shklovskii, A.L. Efrös, Electronic properties of doped semiconductors, Springer Verlag, Berlin, 1984
[4] J.M. Benoit, B. Corraze, O. Chauvet, Phys. Rev. B 2002, 65, 241405(R)
[5] S. Marianer, B.I. Shklovskii, Phys. Rev. B 1992, 46, 13100; B. Cleve et al., Phys. Rev. B 1995, 51, 16705
[6] V.L. Nguyen, B.Z. Spivak, B.I. Shklovskii, Sov. Physic. JETP 1985, 62, 1201
[7] U. Sivan, O. Entin-Wolman, Y. Imry, Phys. Rev. Lett. 1988, 60, 1566

Fabrication, Control and Properties of Nanocrystalline Copper

Lembit Kommel, Jakob Kybarsepp, Renno Veinthal, and Rainer Traksmaa
Department of Materials Engineering, Tallinn Technical University, Tallinn

1 Abstract

Test specimens with nanostructure of pure copper were fabricated using the Equal-Channel Angular Pressing (ECAP) method. After nine passes under of Severe Plastic Deformation (SPD), at 90° between two channels of the die, grain size was reduced to 40 nm. We describe the mechanism of transformation related to the structure and properties in the ECAP deformed region at the first pass. Special experiments covered the structure, physical and mechanical properties of nanostructure materials. The paper compares the effect of different structure conditions on the mechanical properties of copper.

2 Introduction

Metallic materials are composed of crystalline grains whose arrangement and characteristics can be altered by casting, deformation or/and heat treatment. Structurally, these materials are mostly mono-, micro- or nanocrystalline. Structural features, including size, shape, distribution and orientation of grains and grain boundaries in the structure, determine the properties of the metals. It is obvious that structure has a major influence on the values of state parameters of a material. For example ”whiskers” strengths will reach the theoretical strength of their metals. Real engineering metals and alloys have microcrystalline structure with relatively lower mechanical properties. Hot, warm or cold deformation under severe plastic deformation (SPD) of a metal is commonly used to form a nanocrystalline structure, required for a directional change of metal properties.

Segal [1] was the first to manufacture fine-grained and nanocrystalline metals and alloys in 1977. By help of the Equal Channel Angular Extrusion (ECAE) or – Pressing (ECAP) method, a technique of the Severe Plastic Deformation (SPD), fine-grained or nanocrystalline structures in metals can be obtained.

Kopylov [2] used this method for large billets manufacturing and showed that grains refinement depends on the ECAP process temperature and strain rate conditions. He also showed that after the ECAP treatment, the mechanical properties of materials, such as hardness, yield stress, ultimate strength, elongation and reduction of area, increase up to three-four times. Kim et al. [3] used the elastoplastic finite element method to estimate the effect on the overall elastic and plastic properties of nanocrystalline copper. In his calculations he used the properties of crystallites and grain boundaries. He showed that the yield stress of copper can be increased up to 760 MPa, with a decrease in grain size to 2 nm. The microsample [4] tensile testing of nanocrystalline copper with high-angle grain boundaries shows the identical yield strength and low ductility. Therefore, it is surprising that nanocrystalline materials have a lower elastic modulus (E) than coarse-grained materials. Depending on the decrease in grain size, the ratio of the bounda-

ry region in the structure increases, resulting in a lower elastic modulus and higher yield strength than that in the coarse-grained materials. Using a classical molecular dynamics simulation and a many-body potential function of the second-moment approximation of the tight-binding scheme by Jeong Won Kang et al. [5, 6], the thermal properties of ultra-thin copper nanobridges and atomic-scale simulations of copper polyhedral nanorods were investigated. Papers [7, 8] describe the influence of the ECAP on the structure and properties of pure copper forming, and their evolution during SPD. Maximal increases in the indentation modulus and elastic parts of the indentation work can be obtained during the first ECAP pass. These parameters do not increase so rapidly during the next passes.

Thus, based on previous investigations [1–8], nanocrystalline metallic materials have relatively higher mechanical properties at relatively low temperatures than simple microstructures. In nanostructure forming, the route scheme [9] has an influence on the properties. In [10] it was shown that an increase in the deformation temperature depends on the ECAP processing parameters, i.e., deformation route scheme and the preheating temperature of die.In [11] the tensile and shear stress, strain path and in [12] large-strain work hardening/softening during the cyclic deformation of nanocrystalline pure copper with and without heat treatment were studied. These properties were compared with the properties of coarse-grained pure copper. The structure evolution during the formation of the nanostructure state by SPD in the atomic scale and dynamic atomic displacements of a material were described in [13]. In [13] it was shown that the Debye temperature is lower, up to 22–23 %, in the nanostructure of Cu and Ni. In [14] the triple junction of nanocracks forming in nanocrystalline materials was discussed and a theoretical model of grain boundary sliding through these junctions was suggested.

In conclusion, ultra-fine grained metallic materials (high strength and plastic material) can be used for different purposes. Examples [15] include medical implants manufactured from pure titanium, the properties of which are comparable to the alloyed titanium alloy Ti-6Al-4V. Experimental [1, 2, 4–13] and theoretical [3, 14] investigations of the state of nanomaterials parameters are very complex. No satisfactory solution has been reached.

Therefore, by help of experiments, we attempt to describe the structure and properties of nanocrystalline pure copper fabrication and control. The aim is to discuss changes in the structure and mechanical properties, such as micro-, plastic- and universal hardness, indentation work (total, plastic and elastic parts), creep and relaxation in the ECAP deformed region during the first pass and after five passes. The data of the tested mechanical properties of materials are presented to compare the structure up to its nanocrystalline state. The properties of the ECAP-processed up to the nanocrystalline structure are compared with those of coarse-grained cold-drawn and recrystallized pure copper.

3 Experimental

3.1 Fabrication Features of Nanocrystalline Copper

We used a pure copper rod with a diameter of 16 mm and a length of 150 mm. Cold-drawn and annealed state of pure copper had a coarse-grained structure with grain sizes up to 150 μm and 250 μm, respectively. These specimens served for comparison. For the ECAP processing, annealing at 650°C during 1.5 hours was used. The chemical composition of the material was de-

termined by help of the atomic-emission spectroscopy (SPECTROLAB-M). Our analysis showed that the material contained Fe = 0.0238 wt.% and Al = 0.0084 wt.%.

The diameter of the channels in the ECAP die was 16 mm and the angle between the two channels was 90°. During the ECAP processing under pressure of the hydraulic press, the load was in the range of 400 to 560 kN. The actual speed of the uniaxial pressure was 5 mm/s. In this work, the route B_A scheme [9] was chosen. At room temperature, a maximum of up to twelve passes were conducted. During the first pass of the processing, three specimens and during the fifth pass, two specimens of the ECAP processing were stopped to determine the mechanisms of structure and the properties formed at SPD in the ECAP deformation region. The other pure copper rods number 30 were divided into three main groups for specimen manufacturing. The first group included specimens after recrystallization annealing at 650 °C during 1.5 hours, the second group contained specimens in the cold-drawn condition (for comparison), and in the third large group, the specimens had a different SPD microstructure condition up to 40 nm of grain size. To determine the structure and mechanical properties, the same specimens were used.

3.2 Testing Apparatus

During the first pass of the ECAP processing, the microstructural features in the ECAP deformed region were determined by means of the optical microscope (OM) Nikon CX. The scanning electron microscope (SEM) Gemini LEO Supra-35 was used for nanostructure investigation. The X-ray diffractometer (XRD) D5005 Bruker AXS with the Win-Crysize (in the Single Line method) computing program was used to define the mean grain size of nanocrystallites. To find out changes in material hardness and mechanical properties in the ECAP deformed region, the universal hardness tester (HU) Zwick Z2.5/TS1S was used, and microhardness was analyzed by the measuring load 50 gr and test time 12 s on the microhardness tester (HM) Mikromet-2001. The tensile stress, ratcheting rate, and viscoplastic behavior (during HCV [12] deformation) of pure copper specimens with different structure conditions were tested on the Instron Corporation Series IX Automated Materials Testing System 8.15.00.

4 Mechanism of Transformation of the Microstructure in the ECAP Deformed Region

First, for the ECAP processing, the annealed bulk bars of pure copper were used. In the ECAP deformed region (thickness is 2.6 mm on the optical picture) in Figure 1, during the first pass at the ECAP processing, the microstructure changes by SPD took place. In this part in the ECAP deformed region the „clear ECAP“ [2] of metal was formed.On the left side of the optical picture (Figure 1), the equiaxed structure is shown. The structure consists of white, brown and dark grains, accordingly. The color of grains depends on the impurity levels (Fe, Al), like with doped crystals, and on the orientation of crystals to the polished surface. The impurities of Fe and Al content in black grains are maximal.

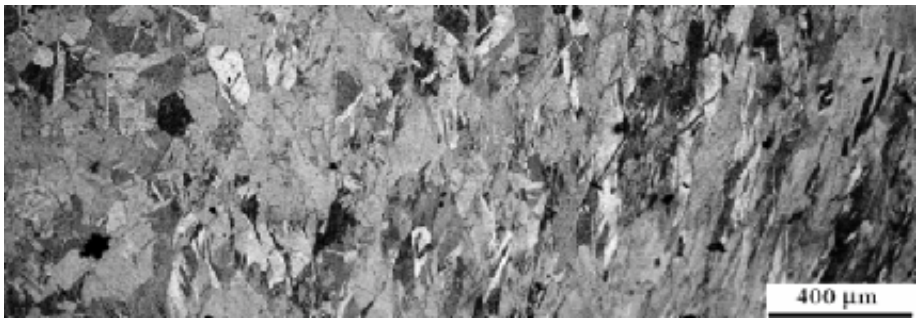

Figure 1: The microstructure transformation in the ECAP deformed region on optical micrograph during first pass is shown. The thickness of this region is 2.6 mm on this optical photo.

In the middle part of the photo, equiaxed structure changes in the grains occurred. On the right side of the photo, the grains have a different axis, as a result of SPD and their orientation corner (directivity angle) increased up to 45° to specimen axis, in alignment to metal plastic flow. SPD took place by grain deformation, with their thinning. After the first pass, the lamellar microstructure of a metal had a very directional character. Depending on the rotation scheme and passes number [8]; the mechanism of microstructure transformation may be different.

5 Mechanism of Transformation of Mechanical Properties of Recrystallized Copper in the ECAP Deformed Region

Microstructure investigations showed that up to eight ECAP passes the metal had a compulsory crystallization structure. The white grains of copper had a smeared image and therefore they were first refined. Light grains had lower microhardness than black ones. The results of microhardness test of copper in the ECAP deformed region during the first pass and after five passes are shown (Figure 2). The thickness of the indentation test region in metal is 20 mm. On avera-

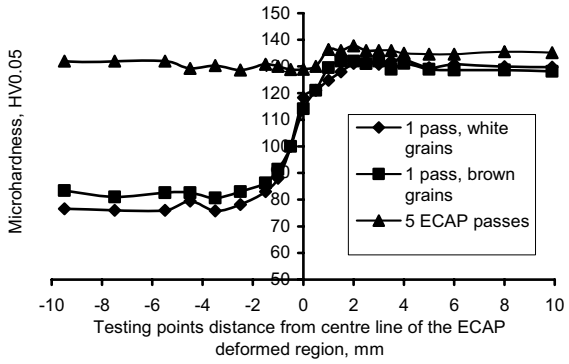

Figure 2: Effect of the SPD in the ECAP deformed region at the first pass and at the fifth passes on copper microhardness change. Curves: 1 pass, white grains, 1 pass, brown grains and 5 ECAP passes.

ge, the measured microhardness of recrystallized copper was about 63HV0.05. Grain microhardness differed in the limits of ±4HV0.05 to ±10HV0.05. The microhardness of the dark grains of coarse-grained cold-drawn copper was up to 110HV0.05.

A maximal increase in microhardness was reached during the first pass. After pressing in the ECAP die by strength 2800 N/mm^2 until emergence of SPD (left side of the graph in Figure 2, curves 1 pass, white grains and 1 pass, brown-black grains, respectively), the average value of microhardness increased up to 77HV0.05 for white grains and up to 82HV0.05 for dark (brown and black on color photo)grains. During the first pass, the microhardness of annealed copper increased to 116HV0.05–120HV0.05 on the centre line of the ECAP region. During the first pass, microhardness increased on 2-3 mm from the centre line of the ECAP region up to maximal values 136HV0.05 and then decreased slightly (Figure 2). We mean that the decrease of microhardness depends on the relaxation process at the temperature of deformation [11] increase.

After five passes, microhardness of pure copper increased up to 137HV0.05 and after ten ECAP passes, the maximal measured value of hardness was maximal (average value), only 145HV0.05 in this work. The measured values of microhardness depend on the direction of specimen sections and the ECAP pass number. As the number of passes increases, the differences of microhardness levels in sections decrease from 10HV0.05 to 4HV0.05, after the first pass and after ten passes, respectively.

The universal (HU) and plastic (HU_{plast}) hardness (load application point 30 N) of copper (Figure 3) and microhardness (Figure 2) were identical in terms of distribution in the ECAP deformed region. These parameter increases were maximal during the first pass, from HU 30 = 908 N/mm^2 up to HU 30 = 1494 N/mm^2 at a distance of about 4 mm from the centre line of the ECAP deformed region.

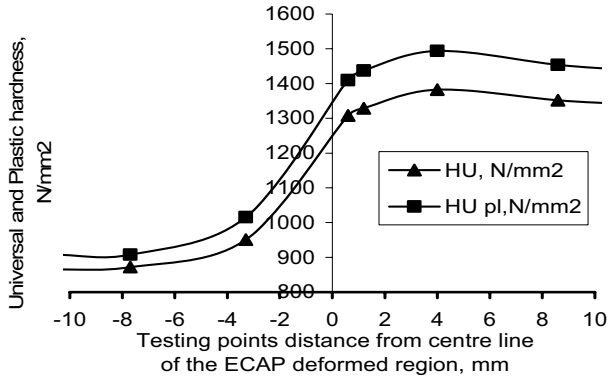

Figure 3: Effect of the SPD in the ECAP deformed region at the first pass on the universal (HU) and plastic (HU_{pl}) hardness of copper increase

The indenter indentation work (W total) changes during testing at the first ECAP pass show (Figure 4) that the elastic properties of copper increased. This parameter shows the changes on the level of the atomic scale of the material [13]. Test results show that during the SPD of copper, in the ECAP deformed region, the elastic part of indentation work was formed (Figure 4,

curve W elastic). As a result of this testing, the ratio of the elastic part to the total indentation work or the ratio of elasticity (ηHU) was determined. The ratio of elasticity has a pulsating character of changes, and the average curve during the first pass of the ECAP is shown in Figure 5. Up to seven passes of the ECAP, plasticity and elasticity increases were very small. For nanocrystalline copper, this parameter increased up to 5–6 %. The ratio of elasticity (Figure 5) of copper during SPD increased up to 2-3 times and had a maximum value on the centre line of the ECAP region. This parameter of the material is different and changes during the deformation of the material at the ECAP region.

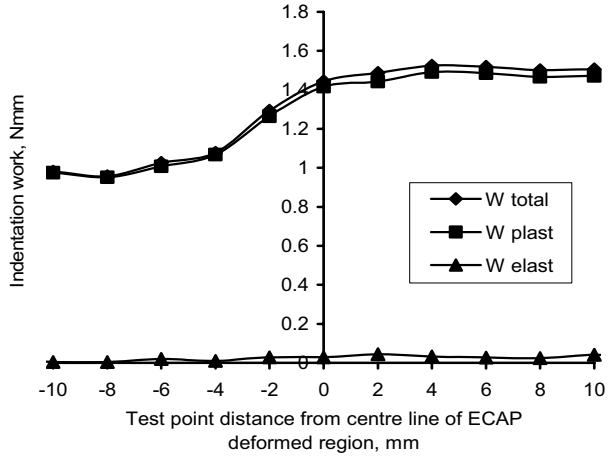

Figure 4: Indentation work (W total, W plastic and W elastic parts) increases at the ECAP deformed region during first pass

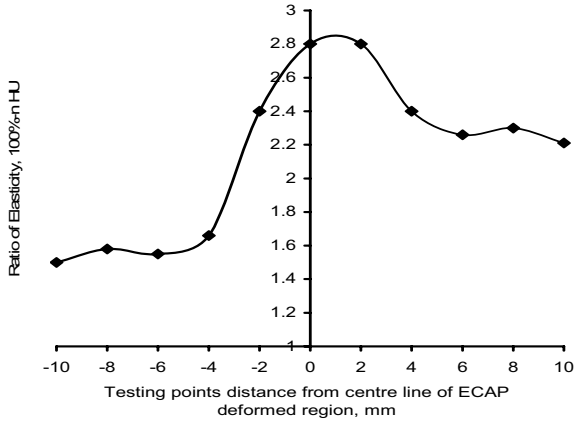

Figure 5: The elastic part of indentation work (ηHU) change in the ECAP deformed region at the first pass

The effect of the first pass on the changes of material relaxation (RHU) and creep (CHU) at the ECAP deformed region is shown on the diagram (Figure 6). These parameter changes have a pulsating and increasing character, which depends on the distribution of slip plains of the metal on the test point. The micro- and universal hardness decreases after their maximal value. Properties decreasing depend on the relaxation increase on this distance from the centre line of ECAP deformed region.

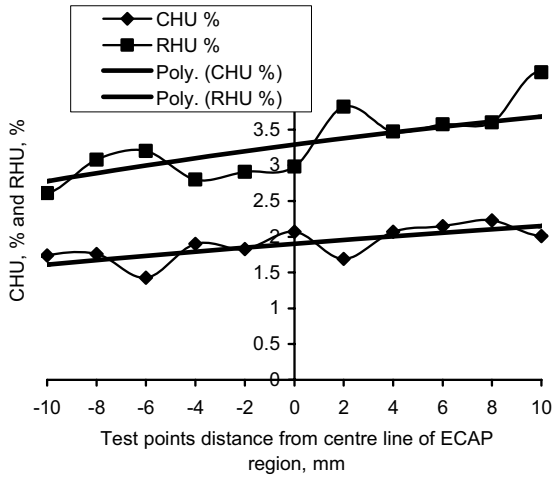

Figure 6: Creep (CHU) and relaxation (RHU) changes in the ECAP deformed region at the first pass

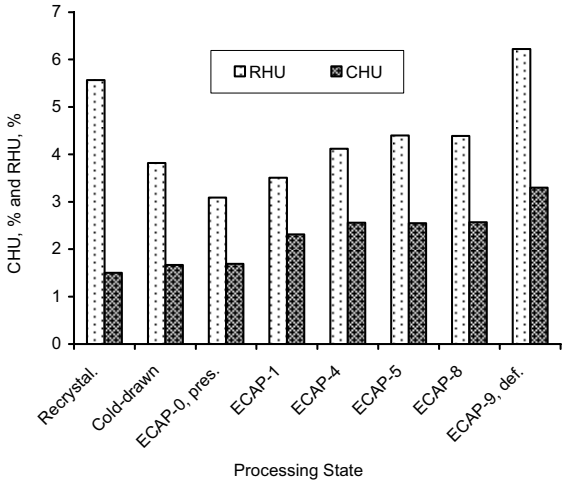

Figure 7: Effect of ECAP processing up to nine (with cold forging) passes on relaxation (RHU) and creep (CHU) of pure copper is shown. The recrystallized and cold-drawn copper for comparison is shown.

To compare creep and relaxation recrystallized and cold-drawn coppers were used (Figure 7). Creep and relaxations properties of recrystallized copper were about two times lower than the ECAP-9 processed copper with post-cold forging (Figure 7, ECAP-9, def). Under high pressure, relaxation decreases were maximal (Figure 7, ECAP-0, pres.). During the ECAP at compressive stress 2800 N/mm^2, relaxation decreased to 3.1 %. The relaxation of cold-drawn copper was RHU = 3.8 % and that of recrystallized copper RHU = 5.6 %, respectively. During SPD, the maximum value of relaxation RHU = 4.4 % was obtained. After nine passes of the ECAP, followed by cold forging from the diameter of 16 mm to the diameter of 9 mm (Figure 7, ECAP-9, def.), the relaxation of nanocrystalline copper and maximal values of creep were 6.2 % and 3.3 %, respectively. Relaxation increases during SPD influence the mechanical properties, decreasing after each ECAP passes. To decrease the relaxation of nanocrystalline structure material, heat treatment was used.

6 Structure and Mechanical Properties of Nanocrystalline Pure Copper

As was shown above, the structure and mechanical properties forming at SPD occur in the ECAP deformed region. The grain size of the nanostructure of pure copper was reduced to 40 nm. As shown in the SEM picture (Figure 8, cross-section of the specimen), during ten ECAP passes, step-by–step the coarse-grained microstructure of recrystallized copper (Figure 1, left

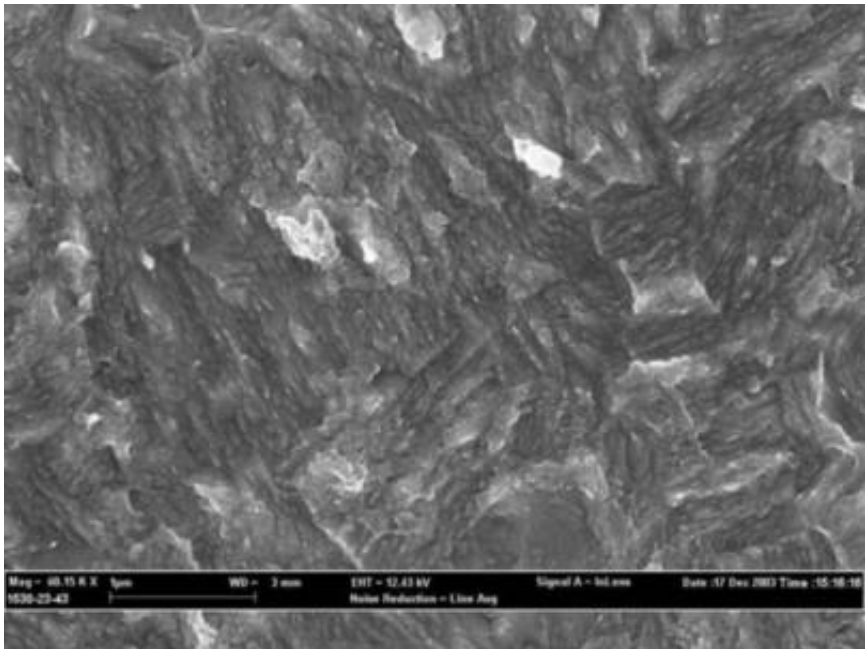

Figure 8: SEM picture of the nanocrystalline copper on cross-section of specimen is shown

side) was turned to the nanocrystalline form, with the mean grain size less than 40 nm (Figure 9, axial section of the specimen). The white areas in the picture are defect zones (without sticking). This grain size was also determined in the direction of the plane (111) at 43.4° in the 2-Theta-scale of the X-ray picture. During ten ECAP passes at the room temperature, in the condition of SPD, the nanostructure (Figure 9) was formed in copper. The nanocrystals of this structure are elliptical. In the axial section of the specimen, the angle of grains is identical to the metal plastic flow during the ECAP processing.The metal nanostructure in the axial section has a directional character. As shown in the SEM pictures, the nanostructure on all the surfaces in the direction of specimen cross-section contains blocks with different angles between their orientations (Figure 8). The inside of the blocks with nanocrystals of ellipsoid are not of a different orientation. The biggest axes oriented mainly in the direction of the metal plastic flow. These crystals have the highest interatomic attraction energy [13] in a nanocrystalline metal.

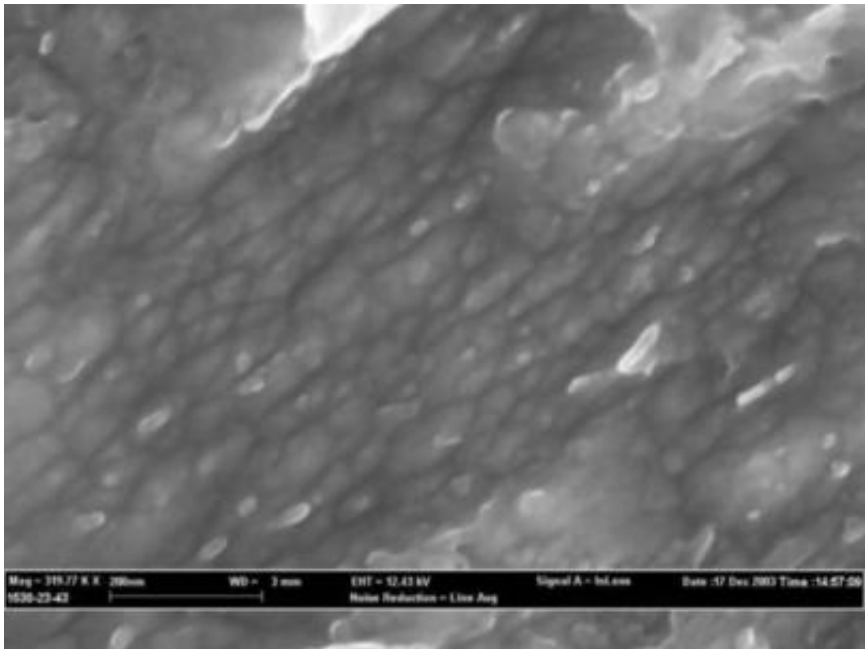

Figure 9: SEM picture of the nanocrystalline copper on axial section of specimen is shown

As a result of this nanograins forming, the tension stress of nanocrystalline copper was increased up to 430 MPa. As was shown (Figures 6 and 7), the relaxation of the metal (during the ECAP processing at the increased deformation temperature 220 °C) increased too. The relaxation of the material increasing with a decrease in grain size depends on intergranular interaction and friction [14].

To stabilize the mechanical properties obtained during SPD, the metal was subjected to a heat treatment. The low heating speed at 1 °C/min up to 200 °C and at 2°C/min up to 400 °C was used. After heat treatment, nanograins size was increased only up to 2.5 times. For exam-

ple, after heat treatment up to 400 at the heating rate 2 °C/min, an average grain size was 100.6 nm, whereas the tension stress decreased about 15 % only. The test results at the hard cyclic viscoplastic (HCV) deformation [15] show that the deformation hardening of metal was maximal after heat treatment at 400 °C. The coarse-grained cold-drawn metal showed only deformation softening and coarse-grained recrystallized copper deformation hardening. The highest and excellent stable mechanical properties during the HCV deformation show the metal, which was heat treated at the temperature up to 200 °C by the heating rate at 1 °C/min [12].

7 Discussion

The microstructure of recrystallized pure copper had an average equal-axed grain size up to 250 μm. During the first pass, grains were deformed in the view of thin laminations (Figure 1). They were oriented under 45° to specimen longitudinal axis, in the direction of the metal flow at SPD. The mechanical properties of the material were identical to the mechanical properties of a cold-drawn material. During nine passes at the ECAP processing, the grain size of the structure was refined to nanomeasures.The increase in micro- and universal hardness in the ECAP deformed region and the tension strength [4–8] of the material were identical in character. As the tests results received show, the maximum microhardness increased from 63HV0.05 for the recrystallized state of copper up to 145HV0.05 for the nanocrystallized copper at ten ECAP passes. These parameters increase quicker than other parameters of a metal. During the first passes, the strain hardening of the metal took place. The cold-drawn metal (average grain size up to 150 μm) has a relative high tension stress at low plasticity [7, 8]. After the first pass of the ECAP, the tension stress was increased. The stress-strain curves were identical to the nanocrystalline structure metal; however, the viscoplastic properties were very different. During the first cycles of cyclic deformation, the material had viscoplastic properties, similarly to the cold-drawn material. This softening is quicker than with a heat treated nanocrystalline structure material. After ECAP deformed region (Figure 2, right side) on the distance of 4–6 mm at the centre line of the ECAP region, mechanical properties decreased and as a result of deformation, structural recrystallization took place.

8 Conclusions

- At the first pass of the ECAP, maximum changes in the structure and mechanical properties of the material took place in the ECAP deformed region. The ratio of microhardness, universal hardness, indentation work, elastic work to the total work of the material increased up to 1.5–2 times.
- After the ECAP region, at the deformation temperature increase, the mechanical properties relaxation and structure recrystallization took place. These processes were maximal after the first pass.
- During ten passes of the ECAP, grain size decreased on average from 250 μm to 40 nm. The universal hardness (HU, HU_{plast}, and HV) by the SPD of the material increased up to three times.

- Nanocrystalline materials can be subjected too much higher stresses at cyclic (ratcheting and hard cyclic viscoplastic) deformation without marked plastic deformation as compared to the same coarse-grained materials in the recrystallized and cold-drawn state.
- Therefore, a marked economy of materials can be achieved using nanostructure materials for manufacturing machine parts subjected to the highest cyclic loading during exploitation.

9 Acknowledgements

The authors are grateful to the Estonian Science Foundation for support; Grant N5878.

10 References

[1] V. M. Segal, USSR Patent 575 892, 1977
[2] V. I. Kopylov, in Investigations and Applications of Severe Plastic Deformation (Ed.: T.C.Lowe and R.Z.Valiev), Kluwer Academic Publishers, Dordrecht / Boston / London, 2000, Chapter 1
[3] H. S. Kim, C. Suryanarayana, S.-J.Kim, and B. S.Chun, Powder Metallurgy 1998, 41, 3, 217–220
[4] Y. M. Wang, K. Wang, D. Pan, K. Lu, K. J. Henker, E. Ma, Scripta Materialia, 2003, 48, 1581–1586
[5] Jeong Won Kang and Ho Jung Hwang, Nanotechnology 2002, 13, 503–509
[6] Jeong Won Kang and Ho Jung Hwang, Nanotechnology 2002, 13, 524–532
[7] L. Kommel, K. Kenk and R. Veinthal in Proceedings of the 3rd Intern. Conference Industrial Engineering-New Challenges to SME, ISBN, 9985-59-272-7 (Eds.: J.Papstel and B.Katalinic), Tallinn, Estonia, 2002, Chapter C
[8] L. Kommel, K. Kenk and R. Veinthal, Materials Science, 2002, 8, 4, 396–398
[9] Terence G. Langdon, M. Furukawa, Z. Horita, and M. Nemoto, in Investigations and Applications of Severe Plastic Deformation, (Ed.: T.C.Lowe and R.Z.Valiev), Kluwer Academic Publishers, Dordrecht / Boston / London, 2000, Chapter 3
[10] W. H. Huang, C. Y. Yu, P. W. Kao, C. P. Chang, Materials Science & Engineering, 2003, 1–8 (Article in Press)
[11] J. Chen, W. Wang, L. H. Qian, K. Lu, Scripta Materialia, 2003, 49, 645–650
[12] L. Kommel. Ultra-fine Grained Materials III (Ed.: Y.T.Zhu, T.G. Langdon, R.Z. Valiev, S.L. Semiatin, D.H. Shin, and T.C. Lowe) TMS, 2004 (Article in Press)
[13] I. V. Alexandrov and R. Z. Valiev, NanoStructured Materials, 1999, 12, 709–712
[14] I. A. Ovid'ko, A. G. Sheirman, Acta Materialia, 2004, 1–9 (Article in Press)
[15] R.Z.Valiev, V.V.Stolyarov, H.J.Rack, Terry C. Lowe, Advanced Materials & Processes, 2003, 161, 12, 33–34

Synthesis and Processing of Silver Doped Copper Nanopowders

Cécilie Duhamel, Jean-Louis Bonnentien, Michael Walls, Martin Hÿtch and
Yannick Champion
Centre d'Etude de Chimie Métallurgique – CNRS, 15, rue Georges Urbain, 94407 Vitry-sur-Seine, France

1 Abstract

Silver doped copper nanoparticles were produced using the cryomelting technique and then densified. The influence of the sintering temperature on the final microstructure was studied with a particular attention paid to the localization of silver in the material.

2 Introduction

Recent work on the mechanical properties of bulk nanocrystalline copper (nc-Cu) obtained from powder metallurgy have revealed a near perfect elastoplastic behavior and high tensile strength at room temperature [1]. To further the understanding of the mechanisms involved in the deformation process, the mechanical behavior of nanostructured metals needs to be investigated for a range of temperatures. Before carrying out such tests, however, it may be necessary to improve the thermal stability of samples in order to limit grain growth, particularly at moderate temperatures.

In this context, we have investigated the doping nc-Cu with Ag. The aim is to stimulate silver segregation and to saturate grain boundaries with the doping element, thus impeding grain growth. In addition, modifications of grain boundary structure due to segregation will be of particular interest in relation to mechanical properties. To this end, sintering conditions of $Cu_{99.75}Ag_{0.25}$ nanoparticles have been explored and the microstructures characterized by X-ray diffraction (XRD) and transmission electron microscopy (TEM). Chemical information will be obtained using electron energy-loss spectroscopy (EELS) on a dedicated scanning transmission electron microscopy (STEM).

3 Experimental Details

3.1 Sample Preparation

The synthesis of nanopowders of controlled composition is carried out in two steps. First, a Cu-0.25 at.% Ag master alloy is prepared by heating copper and silver in nominal proportions, in levitation, by radio frequency induction. Secondly, a sample of the as-prepared alloy is used to produce the nanopowders by cyrogenic evaporation-condensation [2]. Briefly, a droplet of approximately 30g is heated and maintained in levitation within an atmosphere of liquid nitrogen. The droplet is fed regularly by a metal bar of the master alloy in order to compensate the loss of weight during evaporation. Nanoparticles are produced by the instantaneous condensation of

the metal vapor surrounding the molten metal. After their formation, they are conveyed towards linen filters where they are collected. Nanopowders are pyrophoric, due to their large surface area, and are therefore stored in hexane in order to allow slow passivation. The powders are then compacted under 450 MPa using cold-uniaxial pressing to obtain pellets with a diameter of 13 mm and a thickness of about 1 mm. Samples with a relative density around 60 % are sintered under hydrogen, from room temperature up to temperatures ranging between 250 °C and 400 °C, with a linear heating rate of 1 °C min^{-1}.

3.2 Characterization Techniques

The average composition of the nanopowders was determined by Inductively Coupled Plasma / Optical Emission Spectroscopy (ICP/OES) revealing a silver content of 0.25 at%. In spite of the difference in the vapor pressure of the two metals (Cu and Ag), no deviation from the expected composition was observed. The crystalline structure and grain size were determined by X-ray diffraction (XRD) line width analysis, the measurements carried out using a Philips generator operating at 40 kV and 30 mA. The Co Kα radiations ($\lambda\alpha_1$ = 1.78896 Å and $\lambda\alpha_2$ = 1.79285 Å) were selected using a curved graphite monochromater. XRD line profiles were analyzed using the software EVA (Brüker) to determine mean particle size and internal strain. The microstructure of the sintered samples was observed using a LEO 1530 field emission scanning electron microscope (FEG-SEM) operating at an accelerating voltage of 3 kV. Transmission electron microscopy (TEM) was carried out using a Jeol 2000 EX microscope operating at 200 kV for conventional observations and a VG STEM (HB5) with a cold FEG operating at 100 kV for EELS experiments. Chemical maps of Cu, Ag and O were obtained by analyzing the L, M and K edges respectively of each element at each position of the STEM probe (probe size: 1 nm, step size: 2 nm).

4 Results

4.1 Nanopowders Preparation and Characterization

Bright field TEM images show that the particles are spherical in shape (Figure1) with sizes ranging from 30 to 110 nm. Weak bonding between particles tends to connect them in chains. Twins are often present and a 2–3 nm thick oxide layer coats the particles due to their passivation in hexane. Electron diffraction shows the characteristic rings of the copper fcc structure with two rings corresponding to the oxide layer. However, no rings corresponding to Ag is detected. To complete these local observations, XRD experiments were carried out. The X-ray diffraction pattern on Figure 2 confirms the copper fcc structure with a lattice parameter equal to 0.3616 ± 0.0001 nm, consistent with that obtained for pure copper nanoparticles. Moreover, Cu_2O is detected, showing that the oxide layer is well-crystallized and accounts for 24 % of the volume fraction of the particles (determined from integrated peak intensities in XRD spectrum). This is consistent with measured oxide layer width with respect to particles size. As before, no additional line due to Ag is detected.

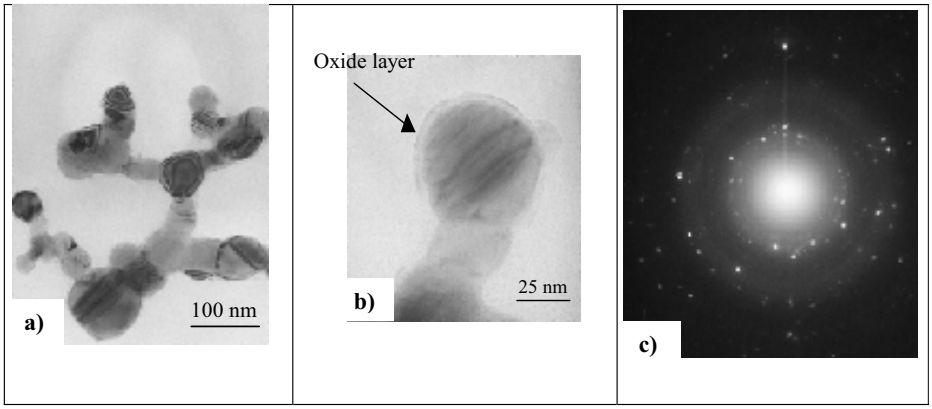

Figure 1: a) and b) TEM micrographs of Cu(Ag) nanopowders, c) electron diffraction

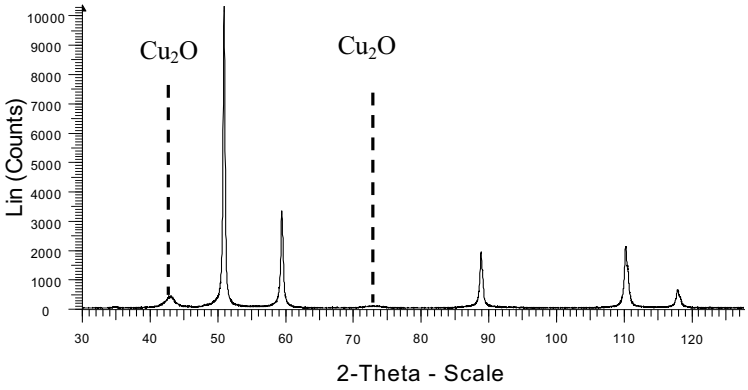

Figure 2: X-Ray diffraction pattern of Cu(Ag) nanopowders

Besides the structural information extracted from this pattern, X-ray lines broadening analysis is used to estimate the average particles size and lattice distortions. Each peak of the pattern is fitted by a pseudo-Voigt function. For each line, the integral breadth, defined as the ratio of the peak area to the peak intensity, is measured and then corrected from the instrumental contribution. The standard reference material used to determine the instrumental breadth is LaB_6. The Halder-Wagner method is then applied to estimate the size of single diffracting domains [3]. As shown on the TEM micrographs, most of the particles correspond to a single diffracting domain but some of them contain twins. In order to have a better approximation of the particles size, twins contribution is removed by using the method developed by Warren leading to a twin boundaries density equal to 0.6 % [4]. The average particle size is found to be 56 nm ± 3 nm which is in agreement with the sizes measured on TEM images. No lattice distortion is found in the powders.

4.2 Densification

Sintering conditions need to be optimized in order to obtain a highly densified material without too much grain growth. Sintering is carried out under a H_2 atmosphere from room temperature to temperatures ranging from 250 °C to 400 °C. Reduction of the oxide layer is necessary before densification can occur and can be monitored by XRD (Figure 3). The volume fraction of oxide, estimated from XRD spectra, is plotted as a function of temperature on Figure 4. Most of the cuprite is reduced between 250 °C and 300 °C, and by 350 °C, oxide is no longer detectable.

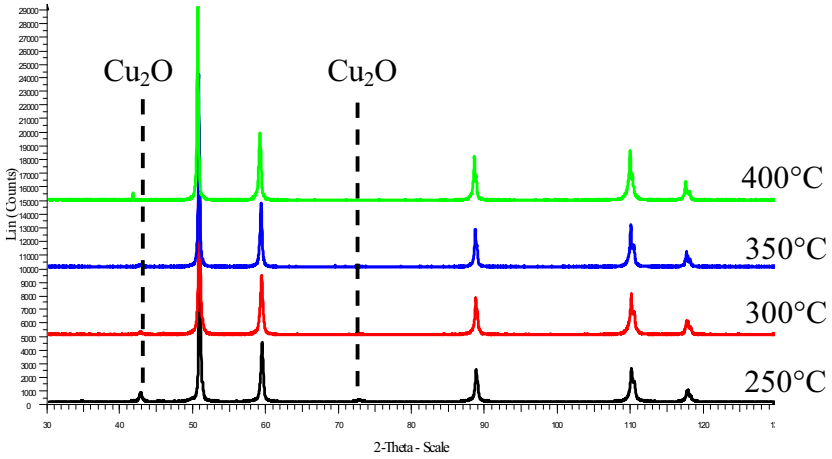

Figure 3: X-Ray diffraction patterns of sintered nanopowders

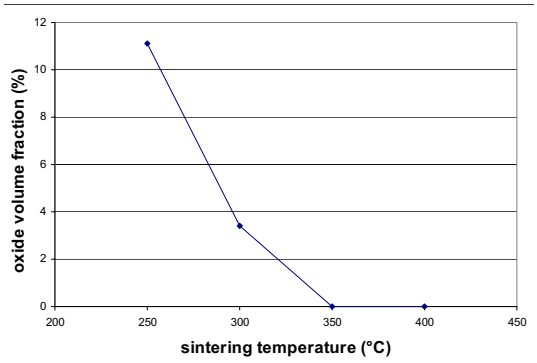

Figure 4: variation of the oxide volume fraction with the sintering temperature

Figure 5 gathers together the results obtained on relative densities measured by picnometry, Vickers microhardness and grains size measurements (XRD) for the samples. Grain size was determined using the Halder-Wagner method corrected for twins, as for the powders. It can be seen that whatever the sintering temperature, grains size remains in the nanometer range, vary-

ing between 90 and 100 nm. For the sample heated to 350 °C, grains size is a little higher because the sample was cooled in the oven. A similar trend is observed for densification with the relative final density approximately constant for all samples. Shrinkage reaches 10% for the sample heated to 400 °C, the green density being of 58 %. Microhardness, however, decreases between 250 °C and 300 °C and then tends to stabilize around 400 °C. This is not due to any variation in grain size or density, but corresponds to reduction of the oxide. Cuprite being harder than pure copper, the more cuprite the sample contains the harder it is. Between 250 °C and 300 °C, the volume fraction of Cu_2O falls from 11 % to 3 % explaining the microhardness decrease and after 300 °C, when the oxide layer is completely removed, microhardness stabilizes.

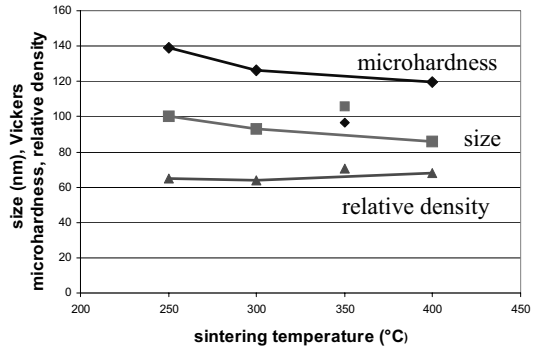

Figure 5: Variation of grain size, Vickers microhardness and relative density with the sintering temperature

The final microstructure of the samples depends on the sintering temperature. Figure 6 are SEM micrographs of the fracture surface of pellets broken after sintering. For $T < 300$ °C, Figure 6 a) reveals that the grains keep their spherical shape. Consolidation has begun but without shrinkage: the material remains porous. TEM images (Figure 7 a)) show that grains size is still in the nanometer range. The contrast inside each grain is homogeneous, and no Ag precipitates are detected. In this temperature range, oxide reduction takes place but densification has not be-

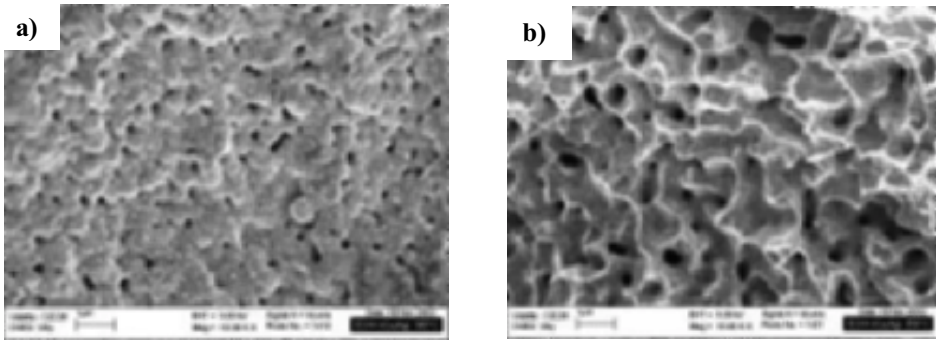

Figure 6: SEM micrographs of sintered nanopowders: a) sintering temperature of 300 °C, b) sintering temperature of 400 °C

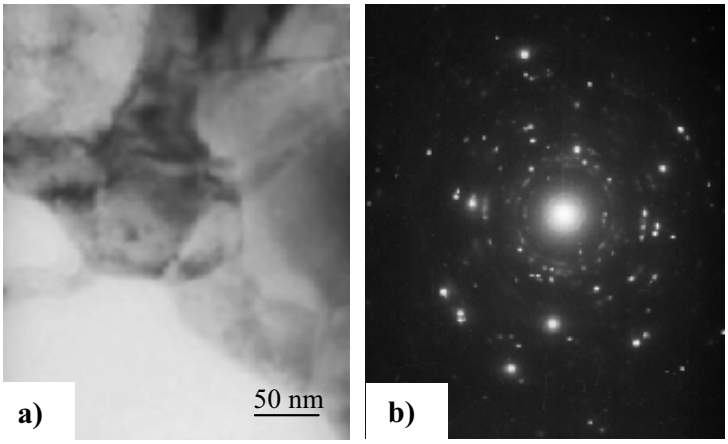

Figure 7: a) TEM micrographs of sintered nanopowders (T = 250 °C), b) corresponding electron diffraction

gun yet. Moreover, it seems that Ag has not diffused yet towards the grain boundaries. The presence of a crystalline oxide layer is confirmed by electron and X-ray diffraction (Figure7 b)) but no crystalline phase of pure Ag is detected by either of the two techniques.

For T > 300 °C, the sample's microstructure is quite different. SEM (Figure 6b) shows that consolidation occurs with the formation of necks between grains. The surface presents similarities with a ductile fracture surface with cupping. However, the material is still porous and spherical grains similar to the ones observed for temperatures below 300 °C still exist. Bright field TEM micrographs (Figure 8 (a)) reveal the presence of small spherical precipitates with an average diameter of 10 nm. Additional rings due to pure silver appear on the electron diffraction patterns (Figure 8 c)) tending to prove that silver has precipitated. On the other hand, no oxide is detected. These results have been confirmed by STEM and EELS experiments. Figure 8 (b) is the corresponding silver elemental map of the same area shown in Figure 8 (a). This map confirms that silver precipitates in the matrix but also segregates towards the grain boundaries insofar as the contrast is brighter along the grain boundaries. Moreover, precipitates seem to be

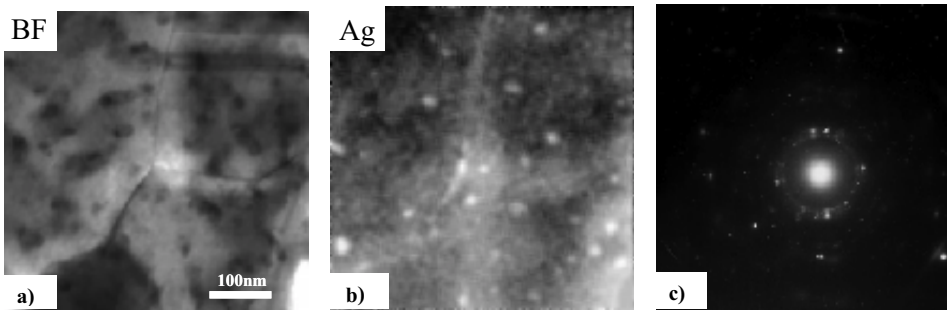

Figure 8: Cu(Ag) nanopowders sintered up to 400 °C: a) bright field STEM image, b) corresponding Ag map, c) electron diffraction

concentrated close to the grain boundaries and especially near triple junctions. Oxygen maps confirm the lack of oxide at grain boundaries or in the form of precipitates.

5 Discussion

5.1 Influence of the Sintering Conditions

The primary aim of this study is to determine and optimize the sintering conditions for Cu(Ag) nanoparticles in order to produce highly densified samples. Table 1 summarizes the characteristic data obtained for the sintering of pure Cu and Cu(Ag) nanoparticles. In both cases, nanopowders are synthesized and sintered following the same procedure. Cu(Ag) nanoparticles appear to be more difficult to sinter: the whole sintering process is shifted towards higher temperatures and less shrinkage is observed. The kinetics of oxide reduction is also modified by the addition of silver as the cuprite is totally removed only for $T = 300$ °C, as opposed to $T = 150$ °C for pure copper. The predominant mechanism for densification involves grain boundary diffusion. As shrinkage is inhibited for Cu(Ag) nanoparticles, diffusional properties of grain boundaries are therefore modified by the presence of silver.

Table 1: comparison of the sintering conditions for Cu and Cu(Ag) nanopowders

Sample	Oxide reduction	Shrinkage	Grain growth
nc-Cu	150 °C	150 °C < T < 250 °C ≈ 20 %	T > 250 °C
nc-Cu(Ag)	300 °C	T > 300 °C ≈ 10 %	T > 400 °C

5.2 Cu-Ag Phase Diagram

The expected nanostructure consists in a matrix of pure copper with silver atoms decorating the grain boundaries. Therefore, the control of the microstructure and of the existing phases is very important. According to the Cu-Ag phase diagram, whatever the composition, a miscibility gap exists at room temperature and under equilibrium conditions [5]. For a silver content of 0.25 at.%, a solid solution becomes possible for $T > 350$ °C. However, the existence of a chemical spinodal implies that a metastable fcc solid solution can exist for silver contents below 5 at.%.

For the powders, the lattice parameter obtained for this phase is in agreement with Vegard's rule. The electron and X-ray diffraction obtained on Cu-Ag nanopowders reveal no characteristic ring for silver. Moreover, TEM micrographs show no precipitation. It can be implied that Ag is in solid solution in Cu, which is in agreement with the phase diagram. Indeed, nanopowder synthesis implies a rapid quenching of the particles in liquid nitrogen. The particles keep the "microstructure" of the liquid phase which is possible because of the existence of the chemical spinodal.

For the sintered samples, for $T < 300$ °C, demixing is predicted by the Cu-Ag phase diagram. However, the temperature is too low to allow bulk diffusion of Ag in Cu [6]. and Ag stays in solid solution in Cu. For $T > 300$ °C, diffusion is activated and, in spite of the solid solution predicted by the phase diagram, Ag segregates towards the grain boundaries as proven by the EELS experiments. Once the grain boundaries are saturated, the excess of silver diffuses along

the grain boundaries up to the surface and then precipitates. These precipitates, revealed by Ag elemental maps, are attributed to a too high Ag content leading to a supersaturation of Ag in the grain boundaries.

6 Conclusions

The main difficulty is to obtain highly densified samples. However, those results are encouraging insofar as silver was firstly introduced in the sample to act as a tracer in the grain boundaries. As the mechanisms involved during sintering and for the deformation are predominantly grain-boundary diffusional, the mechanical properties are expected to vary with different silver contents. This could enable us to investigate diffusional properties at grain boundaries and to determine the influence of the grain boundaries during deformation.

7 Acknowledgement

The authors would like to thank Marcel Tencé and Danièle Bouchet for help with STEM experiments and Jean-Claude Rouchaud for the ICP/OES.

8 References

[1] Y. Champion et al., Science 2003, 300, 310–311
[2] J Bigot, Ann. Chim. Fr. 1993, 18, 369–378
[3] J.E. Langford, International Conference Accuracy in Powder Diffraction II, National Institute of Standards and Technology Special Publication 846, Gaithersburg, MD, USA, 1992
[4] B.E. Warren, Prog. Metal. Phys. 1959, 8, 147
[5] P.R. Subramanian and J.H. Perepezko, J. of Phase Equilibria 1993, 14, 62–75
[6] G. Barreau et al., C.R. Acad. Sci. Paris 1970, 270, 516

Nanoporous Gold as a Metallic Actor Material

Dominik Kramer[1], Raghavan Nadar Viswanath[1], Jörg Weissmüller[1,2]
[1]Institut für Nanotechnologie, Forschungszentrum Karlsruhe, Karlsruhe, Germany
[2]Universität des Saarlandes, Fachrichtung Technische Physik, Saarbrücken, Germany

1 Abstract

The surface stress of metallic surfaces wetted by an electrolyte varies with the charge density and, therefore, with the potential of the electrode. We show that when nanoporous gold electrodes with macroscopic dimensions are charged in an electrolyte the stress changes result in a reversible macroscopic expansion and contraction. Therefore, the length of the sample can be varied simply by applying a potential. In a bimetal foil arrangement consisting of a solid metal layer covered with a layer of nanoporous gold, the strain is converted to a bending movement by simple mechanical amplification. The tip displacement of such a cantilever can exceed 1 mm.

2 Introduction

The surface tension γ of a liquid is a very important parameter of the surface, which influences obvious properties as the shape of liquid drops. The value of γ depends on the potential E of liquid electrodes as described by the well-known Lippmann equation

$$\mathrm{d}\gamma/\mathrm{d}E = q$$

where q denotes the superficial charge density. Therefore the shape of liquid electrodes can depend on the potential.

For liquids, variations of the surface area involve accretion of matter at the interface, at constant atomic structure. Solids electrodes, by contrast, can be deformed by elastic strain alone at low temperatures where diffusion is slow. The parameter which governs the elastic equilibrium at the surface is the surface stress f, the derivative of γ with respect to the tangential strain of the bulk solid abutting at the surface. Similar to γ the surface stress is also dependent on the potential (see, for instance, Ref. [1]), and in model calculations it is found to vary even more than the interfacial tension over the investigated range [2]. As the surface layer of atoms must retain its coherency with the underlying crystal lattice during the elastic deformation, the interface stress must be balanced by stress in the bulk [3]. Independent of the shape of the solid (and of the curvature of the surface), the condition of equilibrium is given by the capillary equation for solids [3],

$$3\,V\,\langle \Delta P \rangle_{\mathrm{V}} = 2\,A\,\langle f \rangle_{\mathrm{A}}\,.$$

The inherent stiffness of solids prevents that the surface stress results in a large macroscopic strain. Contrary to what is observed in liquids, changes in the position or shape of solid surfaces

can be neglected in most cases. Indeed, extremely sensitive equipment is necessary to measure surface stress changes. Measurements were first made by using highly sensitive extensometers [4, 5]. After the advent of cantilever bending techniques using scanning tunneling microscope type setups an increasing number of surface stress data were published, including results for single crystal surfaces [6–15]. Even practical applications of measurements of surface stress changes have been proposed and tested, especially sensors detecting these during adsorption of molecules from the gas [16, 17] or liquid phase [11, 18]. However, typical deflections of cantilevers remain in the lower nanometer range, considerably short of the requirements for practical use in most applications which are typical for solid actor materials.

Surface effects are expected to have a prominent role in nanomaterials because of their large surface-to volume ratio, and for that reason it can be expected that surface stress changes have pronounced effects on nanomaterials. Indeed, surface-stress induced length changes of nanoporous platinum cubes have been observed recently [19]: with a displacement of 1.5 μm the displacement amplitude is enhanced by a factor of 10^3 compared to conventional materials. Therefore, such materials may be attractive for use as actuators [20]. However, integration of the porous metal into a device requires that it can be precisely and reproducibly shaped, and that it can be bonded to the parts which transmit displacement and load. It has not been demonstrated so far how this can be achieved using nanopowder compacts; furthermore, while compacts support a considerable hydrostatic pressure, their resistance to shear stress may be poor. Here we show that nanoporous metals prepared by dealloying a bulk solid solution exhibit similarly large strain amplitudes as nanopowder compacts, and that the porous material can be combined with solid metals foils to form a composite cantilever beam actuator.

Dealloying was used to prepare the nanoporous specimens: By selectively leaching out one component of a single-phase alloy using an (in our case: electrochemical) oxidation process porous samples with nanosized structure are obtained [21]. During dealloying, a phase separation process (spinodal decomposition) results in a sponge-like structure of the more noble metal [21]. Dealloying is attractive as a technique for preparing nanoporous solids, because macroscopic samples with a nanometer-scale porosity extending through the whole bulk can be easily obtained. Complex shapes, readily prepared by forming the starting alloy, can be dealloyed to produce active nanomaterials of sophisticated shape. It can be expected that dealloying can be used for miniaturized components as well – including those made by lithography – because for the small nanostructures that can be obtained, μm sized samples should behave very similar to mm sized samples, except that they can be produced even faster. For the work presented here it is essential that the nanomaterial obtained by dealloying can retain a mechanical bond to its substrate, so that shear stress can be transmitted from the actor to its environment.

3 Experimental

3.1 Sample Preparation

Silver-gold alloy (75 at.% silver, 25 at% gold) was prepared by arc melting of gold and silver wire (ChemPur, Au 99.9985%, Ag 99.99%) under Argon. The ingot was sealed in a fused silica tube and annealed for 80 h at 890 °C. It was rolled by several passes in a motorized rolling mill, interrupted repeatedly to anneal for 15 min at 800 °C (bimetal foils: 750 °C) to remove work

hardening. The dilatometer samples (L_0 = 1.2 mm) were rectangles of cross-section 1.2 × 1 mm^2 cut from a 1.2 mm thick sheet.

Dealloying was performed in 1 M perchloric acid under potentiostatic conditions [22]. The samples were kept at +1 V in fresh $HClO_4$ to remove silver residuals, they were then washed by replacing the electrolyte several times. The samples were permanently kept in solution, except for the electron microscopy studies.

Our results were obtained on samples with a ligament spacing of about 20 nm as shown in Fig. 1. Smaller structures have been obtained by dealloying, down to 3 nm [22]. However, it is known that coarsening occurs at negative potentials [23]. Indeed, the capacitance of freshly prepared samples (as measured by repeated voltammograms in perchloric acid) diminishes slightly with time. This is consistent with a decrease in surface area resulting from coarsening. The sample in Figure 1 had been cycled prior to the electron microscopy; its structure is therefore representative of our samples after the initial coarsening, in particular for the results shown in Figure 2.

3.2 Dilatometry and Electrochemical Measurements

The strain was measured at 299.9 K in a commercial dilatometer (Netzsch TMA 402) equipped with a small glass electrochemical cell, which was cleaned by a mixture of H_2O_2 and sulfuric acid prior to the experiments. The counter electrode was a second piece of nanoporous gold, which was separated from the sample by a glass frit. A commercial small silver/silver-chloride/potassium-chloride electrode (World Precision Instruments) was used as reference in the dilatometer; the potentials were measured and are quoted versus this reference. Control experiments with a platinum wire as a chlorine-free pseudo reference electrode gave consistent results. The solutions were made from concentrated perchloric (pro analysi, Merck) or sulfuric acid (Merck Titrisol) using water that was bidestilled in a quartz glass apparatus.

Since the potentiostat used (PGSTAT 100, EcoChemie) did not support true linear potential sweeps or current integration staircase voltammetry, the voltammogram of Fig. 3 was recorded using the staircase method with a single current reading at each step. This introduces an error in the double-layer current and charge, which vanishes in the limit where the hold time at each step is much smaller than the time constant of the charging. We have estimated the error by varying the step size and extrapolating to zero. The current of Fig. 3 has been corrected in this way, with an estimated uncertainty that may be as large as 30 % of the actual value.

4 Results

Figure 1 shows a scanning electron microscopy image of the nanoporous gold microstructure obtained by dealloying of a $Ag_{75}Au_{25}$ master alloy sheets as described above. The ligament size is in the range of 0.02 μm.

Figure 2 shows the length of a nanoporous gold sample vs. the time (lower part of the figure) obtained *in-situ* the dilatometer during a variation of the potential vs. a Ag/AgCl reference electrode as shown in the upper part of the graph. The length of the sample varies in phase with the potential. Superimposed to the reversible length change, there is a small irreversible shrinking.

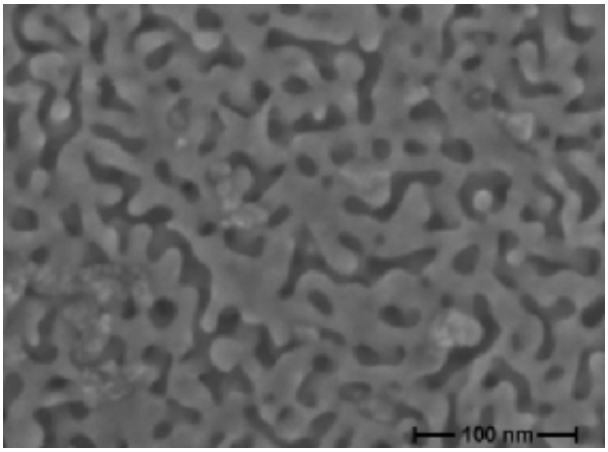

Figure 1: Scanning electron microscope picture of the nanoporous gold structure obtained by etching silver-gold alloy in perchloric acid

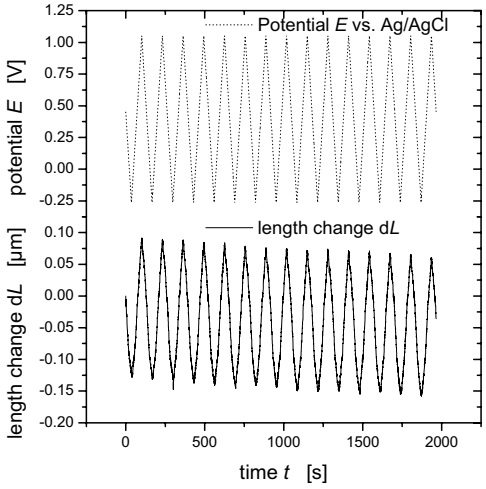

Figure 2: In-situ results obtained during cycling the potential (15 cycles) of a nanoporous gold sample in 50 mM sulfuric acid in the dilatometer. Upper curve: potential of the nanoporous gold electrode versus time measured vs the Ag/AgCl reference electrode. Lower curve: length change of the electrode ΔL versus time.

The cyclic voltammogram in Figure 3 displays the current which was recorded during the potential scan of Figure 2. The result is typical for a polycrystalline gold surface in sulfuric acid. To investigate the capacitive charging of the surface, the potential window has been limited to the range with the onset of hydrogen evolution at the negative end at ca. –0.25 V and the onset of the gold oxidation at ca. 1 V.

From the current of Figure 3, ca. 1 mA, and the scan rate of 20 mV/s, an estimate of the capacity of the sample of 0.05 F is obtained. This is a very large value for a metallic sample with mm dimensions, and it reflects the huge surface area due to the nm-scale porosity. In fact, it has recently been suggested to use nanoporous gold for the construction of supercapacitors [24]. By using a typical capacitance of a gold surface of 0.05 mF/cm^2, the surface area of the sample of Figs. 2 and 3 is estimated to be roughly 0.1 m^2.

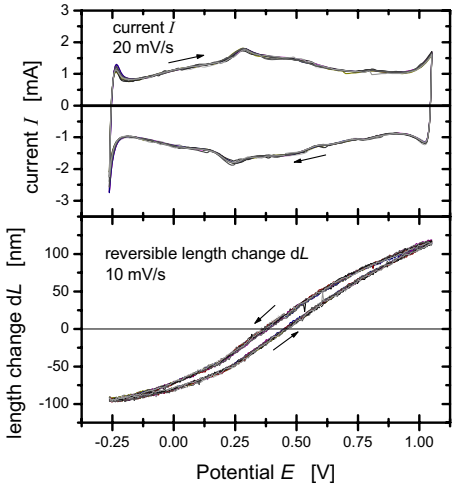

Figure 3: Upper curve: Cyclic voltammogram (15 cycles as shown in Figure 2) of the nanoporous gold in 50 mM sulfuric acid, recorded *in-situ* in the dilatometer. Lower curve: length change of the electrode ΔL versus the potential ("voltstressogram").

It is expected that the surface strain is a function of the charge density. This is supported by the graph of the relative length change $\Delta L/L_0$ versus the charge Q in Fig. 4: it is seen that the hysteresis which is observed in plots of strain versus potential is absent when the strain is plotted versus the charge.

To obtain large displacements, the expansion and contraction of the nanoporous material has to be amplified. We used an bimetallic stripe, which uses the same principle than the bimetal thermometer to convert strain to a visible bending. A silver-gold alloy foil covered with a layer of nanoporous gold was produced rolling the alloy to about 50 µm thickness and by etching the alloy foil from one side only. The opposite surface of the film was covered by nail polish as an insulating coating. The etching depth was selected by limiting the anodic charge to 2/3 of that required to dissolve the silver completely. With stripes 3 cm long and fixed on one side, we obtained large displacements of the tip, in some cases of more than one millimeter during switching the voltage between two of such samples from –1 to 1 volt and back (Figure 5). It is emphasized that the potential window has to be limited to minimize further dealloying at positive potentials and silver deposition at negative potentials. It is emphasized that the potential window has to be limited to minimize further dealloying at positive potentials and silver deposition at negative potentials. When this requirement was complied with the actuation amplitude remained constant over dozens of charging and decharging cycles, e.g. with the foils of Fig. 5.

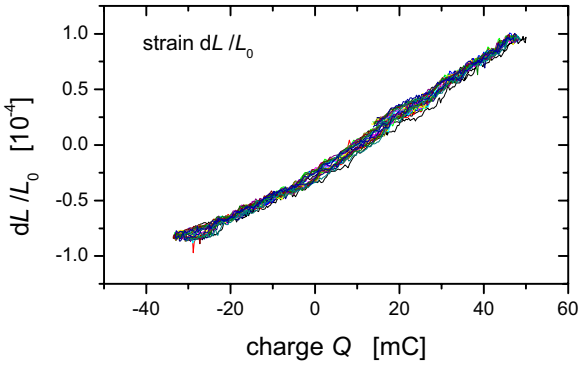

Figure 4: Relative length change $\Delta L/L_0$ versus charge Q. for the 15 cycles of Fig. 2

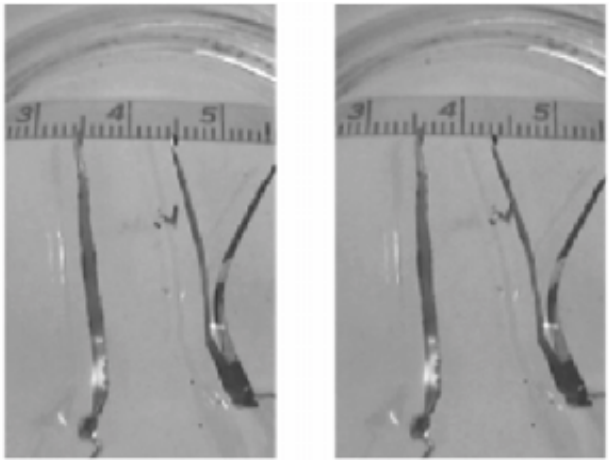

Figure 5: Photographs of a cell with 2 bimetallic foils of nanoporous gold on silver-gold alloy (one of the foils consist of two parts) in perchloric acid with a cm scale in backgrond. The voltage between the electrodes changed the polarity in the meantime between the two photos. Left side: right electrode with –1 V vs. the other. The tips move ca. 1 mm.

5 Discussion

The results confirm our earlier conclusion that it is possible to induce strain with a large amplitude in nanoporous metallic samples simply by changing the charge density on the surface as a function of the electrochemical potential [19]. These earlier results were obtained with nanoporous Pt samples that were made by compaction of nanocrystaline platinum powder [19]. The strain amplitude of Fig. 4 is smaller than that of the nanoporous Pt, which is easily understood due to the larger structure size of the gold with its pores and ligaments with ca. 20 nm diameter. The platinum samples contained smaller crystallites, with a grain size of 6 nm.

Our results show that electrical charges can be used to modify the surface stress and the dimensions of macroscopic samples. This is an example of a material property that can be varied simply by applying a voltage. Therefore, these results supports the suggestion that it should be possible to tune all electron-density dependent properties of nanomaterials (that may be nanocrystalline, but can be coarse grained and nanoporous as well) by changing the potential [25]. To predict the effect of such an electron density variation one might think of using a very simple picture which would assume that adding an electron changes the properties of a nanostructured element towards the properties of the element with larger atomic number according to the periodic system. One example for such a relation would be the similar properties of the isoelectronic (d8) atoms of Pt(II) and Au(III) compounds, e.g. the planar and quadratic geometry of the complexes. Most of the remaining differences of such isoelectronic species are due to the different charges of the ions, and therefore, one might expect that these differences are more subtle in our case, because the charge is not located on a single atom, but distributed on the whole interface. However, this simple isoelectronic picture fails in the present case: The lattice parameters and atomic volumes increase in the series Osmium (76, atomic radius 135 pm) Iridium (77, 135.7 pm), Platinum (78, 138 pm), Gold (79, 144.2 pm) and Mercury (80, 160 pm), and consequently, the concept stressing the bare electron number would predict that adding electrons results in expansion. However, the results shown here and in [19] give the opposite behavior, expansion due to positive charges, which demonstrate that in this case, the influence of the atomic cores can not be neglected. The results can be interpreted as the weakening of the bonding between the atoms due to the removal of binding electrons during charging positively (cf. Ref. [7]).

6 Acknowledgement

Stimulating discussions with H. Gleiter and support by DFG (Center for Functional Nanostructures) are gratefully acknowledged. Many thanks to C. Volkert for taking the SEM picture.

7 References

[1] j. Lipkowski, W. Schmickler, D. M. Kolb, R. Parsons, J. Electroanal. Chem. 452, 1998 193
[2] W. Schmickler, E. Leiva, J. Electroanal. Chem. 453, 1998, 61
[3] J. Weissmüller, J. W. Cahn, Acta mater. 45, 1997, 1899
[4] T. R. Beck, J. Phys. Chem. 73(2), 1969, 466
[5] K. F. Lin, T. R. Beck, J. Electrochem. Soc. 123, 1976, 1145
[6] W. Haiss, J. K. Sass, J. Electronanl. Chem. 386, 1995, 267
[7] Ibach, H., Surf. Sci. Rep. 29, 1997, 195; Ibach, H., Erratum, Surf. Sci. Rep. 35, 1999, 71
[8] R. Raiteri, H.-J. Butt, J. Phys. Chem. 99, 1995, 15728
[9] T. Miyatani, M. Fujihira, J. Appl. Phys. 81, 1997, 7099
[10] H. Ibach, C. E. Bach, M. Giesen, A. Grossmann, Surf. Sci. 375, 1P997, 107
[11] R. Raiteri, H.-J. Butt, M. Grattarola, Electrochim. Acta 46, 2000, 157
[12] C. Friesen, N. Dimitrov, R. C. Cammarata, K. Sieradzki, Langmuir 17, 2001, 807
[13] H. Ibach, Electrochimica Acta 45, 1999, 575

[14] W. Haiss, R. J. Nichols, J. K. Sass, K. P. Charle, J. Electroanal. Chem. 452, 1998, 199
[15] R. J. Nichols, T. Nouar, C. A. Lucas, W. Haiss, W. A. Hofer, Surf. Sci. 513, 263–271 (2002)
[16] R. Berger, E. Delamarche, H. P. Lang, Ch. Gerber, J. K. Gimzewski, E. Meyer, H.-J. Güntherodt, Science 276, 1997, 2021
[17] G. Y. Chen, T. Thundat, E. A. Wachter, R. J. Warmack, J. Appl. Phys. 77, 1995, 3618
[18] J. Fritz, M. K. Baller, H. P. Lang, T. Strunz, E. Meyer, H.-J. Güntherodt, E. Delamarche, Ch. Gerber, J. K. Gimzewski, Langmuir 16, 2000, 9694
[19] J. Weissmüller, R. N. Viswanath, D. Kramer, P. Zimmer, R.Würschum, H. Gleiter, Science 300, 2003, 312
[20] R. H. Baughman, Science 300, 2003, 268
[21] J. Erlebacher, M. J. Aziz, A. Karma, N. Dimitrov, K. Sieradzki, Nature 410, 2001, 450
[22] R. Li, K. Sieradzki, Phys. Rev. Lett. 68, 1992, 1168
[23] R. C. Newman, S. G. Corcoran, J. Erlebacher, M. J. Aziz, K. Sieradzki, MRS Bulletin 24, 1999, 24
[24] M. Cortie , E. van der Lingen, S. Valenzuela, D. Martin, Properties and potential applications of meso-porous gold, submitted to Gold 2003
[25] H. Gleiter, J. Weissmüller, O. Wollersheim, R. Würschum, Acta Mater. 49, 2001, 737

Palladium Nanoparticles Generation Within Microcellular Polymeric Foam

Alexandre Desforges[a], Hervé Deleuze[b], Rénal Backov[a] , and Olivier Mondain-Monval[a]
[a] Centre de Recherche Paul Pascal, Pessac, France
[b] Laboratoire de Chimie Organique et Organométallique, Talence, France

1 Introduction

Supported catalysis has been widely promoted in the last thirty years due to its numerous advantages when compared to homogeneous catalysis [1, 2]: recycling possibility, fixation of the active specie, pollution reduction and so forth. This explains the wide variety of available supports for nanoparticles known to exhibit a catalytic activity [2–4]. Among the main active metallic particles, palladium particles are probably the most efficient ones concerning a large number of chemical reactions [3, 5]. Thus, many routes to support these particles are described [3, 6]. Several important requirements are requested for the process to be efficient:

- the reactive medium should be able to easily diffuse into the supporting matrix
- the support specific area should be important enough to allow for the catalytic activity of the particles to be exhibited
- the solvent-particles interface should be optimized to favor the reaction process
- the support should both be insoluble within the reaction medium and able to retain the metallic particles
- due to the important cost of metallic particles, the support should be easily recycled

Let us also note that in the particular, but common, case of catalytic reactions occurring in an oxidizing medium, the metallic particles should be strongly stabilized by the support in order to avoid their deactivation or solubilization in the solution [2, 7].

In this paper, we describe the synthesis of a new type of catalytic support that is made of a macroporous cross-linked polymer matrix on the surface of which metallic palladium particles are nucleated. We describe different parameters that influence the distribution of the nanoparticles in the support and several synthetic procedures to get the final material. Finally, we test the catalytic activity of these supports using the hydrogenation of allylic alcohol as a test reaction.

2 Experimental Section

2.1 Synthesis of Palladium/PolyHIPE Hybrid Material (Pd/PHP)

In a typical procedure, 4.5 g of styrene, 1.2 g DVB, 4.0 g of chlorobenzene as a porogen and 2 g of SPAN 80 are mixed in a 500 ml hemispherical reactor vessel. The aqueous phase is prepared by mixing 0.16 g of $K_2S_2O_8$ as an initiator, 0.5 g of NaCl, and 60 g of distilled water and then slowly added to the reactor mixture under mechanical stirring with a rod fitted with a D-shaped

paddle, connected to an overhead stirrer motor (at approx. 300 rpm). The emulsion polymerization is carried on by heating to 60 °C using a temperature controlled bath during 12 hours. The monolith is then cut in smaller pieces, washed with ethanol in a soxlhet apparatus during 2 days and finally dried in air at ambient temperature. Dissolved oxygen is removed from water by bubbling Argon gas during 30 min. Then K_2PdCl_4 (33.3 mg) is dissolved in 10 ml of water or water-THF (1:1 w/w) mixture to get a final concentration of 10^{-2} mol/l. The reduction is performed using three different methods presented in the next section. The determination of the Pd loading was performed using combustion elemental analysis by the "Service Central d'Analyse du CNRS" at Vernaison, France.

2.2 Catalysis: Hydrogenation of Allyl Alcohol

A 100 ml reaction vessel equipped with a condenser, a gas inlet and mechanical stirring apparatus, containing 50 ml of THF and the Pd/PolyHIPE (2 % w/w) or the commercial Pd/C (5 % w/w) is degassed with N_2 for 15 min. Then nitrogen is replaced by hydrogen. Once all the N_2 has been replaced, a 2 ml solution of 1 M allyl alcohol in THF is added with a syringe. The hydrogenation takes place under magnetic stirring and hydrogen pressure at ambient temperature. Aliquots are taken at 20 min interval till the complete hydrogenation and analyzed using GC chromatography.

2.3 Instrumentation

X-Ray Photon Spectroscopy (XPS) experiments have been performed using Escalab VG 220i XL. Transmission electron microscopy (TEM) was performed using a CM10 Philips TEM operating at 60kV. Sample preparations are performed by first polymerizing an epoxy resin inside the polyHIPE matrix and then cuting thin film af approx. 80 nm using an ultramicrotone Ultracut E Reichert-Jung. Particle size distributions were determined by counting at least two micrographs of two different regions at 105K magnification. A minimum of 100 particles were taken into account. Scanning electron microscopy (SEM) was performed using a 515 Philips SEM. The X-Ray Diffraction (XRD) powder experiments were performed on a Philips PW1820/1710 powder diffractometer with Bragg-Brentano geometry (Cu $K\alpha_{1,2}$-radiation). Surface areas and pores characteristics were obtained with a Micromeritics ASAP 2010 employing the Brunauer-Emmett-Teller (BET) method.

3 Results and Discussion

3.1 Preparation of the Porous Supports

PolyHIPE (PHP) is a material developed in the early 80's by Unilever [8], which is obtained by polymerization of a concentrated inverse emulsion. This process leads to open-cell morphologies. As previously described [9], these morphologies can be tailored by the emulsion formulation. A wide range of preparation techniques and monomers are available. Possible applications for these materials include adsorbents, catalysts, scavengers, peptide synthesis support, cell

growth media [10,11]. For this study, we have chosen the poly(styrene-co-divinylbenzene) system, which characteristics are well established, and can be easily functionalized with various organic groups. The typical macro-scale morphology is revealed by the SEM micrograph presented on figure 1.a. Due to the size of both cells and interconnecting windows (respectively around 10 and 1µm) the specific surface area is generally low (~5–25 m^2/g). By using a non polymerizable and volatile solvent (further referred to as "porogen component"), a secondary porosity can be obtained by, first, the phase separation between the porogen and the on-growing polymer [12] and then the consequent elimination of the porogen during the washing – evaporation process. In this work, we used chlorobenzene as a porogen. On figure 1b, one can see this secondary porosity in the walls separating two neighboring cells, what we further refer to as mesostructure (for comparison, a SEM picture of the same material without porogen is shown on figure 1a). On figure 1c, we present a TEM picture realized on the system previously filled with resin and cut in thin slices. In these pictures, the polymer appears as gray areas whereas the empty cells appear much clearer. These two types of porosity are clearly revealed by the pictures. In such materials, the corresponding BET surface area is found to be around 90 m^2/g and the smallest porosity induced by the presence of the porogen is typically on the order of 20 nm.

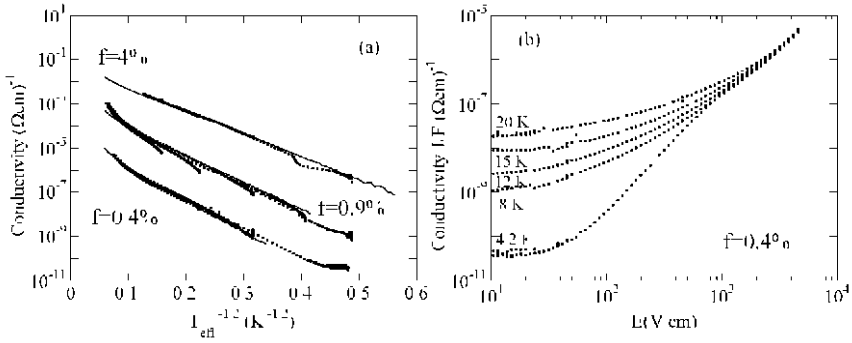

Figure 1: Typical polyHIPE morphology. A) SEM picture of a polyHIPE prepared without porogen; b) SEM picture of polyHIPE prepared with porogen. c) TEM picture of a material prepared with porogen, filled with resin and cut in thin slices. The polymer appears as the gray areas and the pores as the white ones.

3.2 Nanoparticles Generation Inside the Support

3.2.1 Basic Principle of Pd^0 Generation

Basically, two main methods of generating nanoparticles can be cited and referred to as physical and chemical methods [3]. In the first one, a macroscopic bulk metallic powder is mechanically broken in smaller particles (that can be eventually on the nanometer scale). However, obtaining particles with a narrow size distribution appears as a hard task to reach using this method [13]. In the second case, the solid particles can be obtained by the local reduction of, in most cases, a salt originally dissolved in the solvent. The obtained particles will then generally aggregate into bigger objects *via* a nucleation-growth process and the goal is to find a way to stop the growth at the desired size [14]. In this study, we use the chemical way.In the following, we will use a two

step process that consists of, first, filling our support with the palladium salt solution and then reducing the metallic cations Pd^{2+} to their zerovalent state. As we shall see later, the reduction takes place at the surface of the polymer matrix. We probe the influences of the reduction method, the nature of the solvent and the concentration in the dissolved palladium salt, on the size and spatial distribution of the palladium particles.

3.2.2 Particles Characterization

First, the presence of palladium colloidal particles is revealed by a color change in the material. Then, for all the studied samples, we have checked the *in-situ* presence of nanoparticles at the surface of the matrix by observing the resin slices with the TEM. However, such observation does not allow for the determination of the palladium oxidation degree and crystallization state. To determine these important properties, the materials were studied using XPS and XRD. For all the studied samples, the following characteristics were obtained. When performed at the surface of a newly made hybrid material, the XPS spectrum reveals the presence of the $Pd(3d^{5/2})$ band that is located at 336,8 eV. Such a signal can be attributed to palladium oxide PdO [15]. By digging 1–2 nm of the materials surface with an electron beam, we observe a shift of this peak toward the characteristic palladium metallic $3d^{5/2}$ and $3d^{7/2}$ bands respectively centered at 335,2 eV and 340 eV [15] (figure 2a). This experimental result shows that, when exposed to air, the palladium particles located at the outer surface of the monoliths spontaneously oxidize [16]. By contrast, the particles generated inside the matrix are present still in a zero-valence oxidation state. This is confirmed by the XR scattering spectra of the formed particles (figure 2b). The XRD pattern mainly exhibits two diffraction peaks centered at $2\theta = 40°$ and $2\theta = 46.5°$, which are characteristic of metallic palladium materials that crystallize in the Fm3m face centered cubic space group.

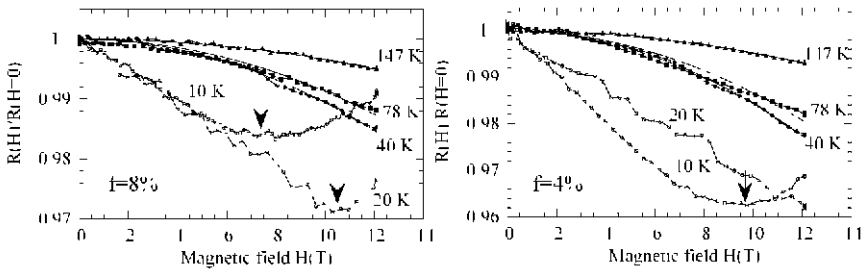

Figure 2: a) XPS spectra showing the positions of the $3d_{5/2}$ and $3d_{7/2}$ peaks characteristic of metallic palladium particles b) XRD pattern performed on powder with the two main peaks at $2\theta = 40°$ and $2\theta = 46{,}5°$. The XRD broad peak centered at $2\theta = 19°$ corresponds to the amorphous bulk organic matrices whereas the two over scaled diffractions at 38.4 (2θ) and 44.6 (2θ) degree correspond to the aluminum support holding the powder.

3.2.3 Critical Parameters for the Particles Synthesis

We have compared different parameters that influence the nanoparticles generation, especially the particles sizes and aggregation states. Beyond those specific nucleation and particles growth

issues, we have studied the homogeneity of the Pd particles spatial distribution within the monoliths.

First, one important parameter is the nature of the solvent that is used to dissolve the palladium salt. The solvent should present the following characteristics, i.e. being polar enough to dissolve the salt completely while being hydrophobic enough to wet the polymer supports. To check this possibility, we used two different solvents, namely pure water and a 50/50 mixture of water and tetrahydrofurane (THF). Since water does not fill the hydrophobic PS support, we chose to fill the matrix with the THF/water 50/50 mixture (THF being a good solvent of polystyrene, it induces a spontaneous wetting and swelling of the polymer matrix) The solvent quality with respect to the polymer matrix can be evaluated by measuring the volume of solvent that can be inserted in 1 g of the polymer matrix (~ 2 ml/g for pure water, ~ 18 ml/g for the H_2O/THF mixture).

The second step consists of reducing the palladium ions in order to obtain palladium particles. Several processes are known to trigger such a reduction step among which we chose to select i) the use of Sodium borohydride ($NaBH_4$, Fig. 3a) ii) UV light (Fig 3b). Surprisingly, we also observed that, when leaving the solvent impregnated in the matrix for a long enough period (i.e. up to 15 days), the reduction of the palladium ions into metallic particles is also observed at the surface of the polymer support (Fig. 3c). This means that the reduction process spontaneously occurs at some active sites in which the electron transfer can take place. We also observed (see figure 3), that the spatial distribution of the particles in the matrix is very different from one process to the other. With either $NaBH_4$ or UV as reduction triggers, the particles are aggregated in big clusters and their spatial distribution within the matrix is very poor (fig. 3a–b).

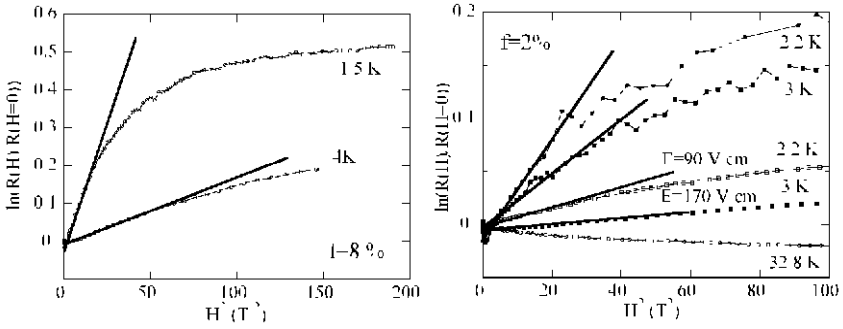

Figure 3: TEM micrograph of materials prepared with $[K_2PdCl_4]=10^{-2}$ M; Initiator $[K_2S_2O_8]$ = 0.25 %; Solvent H_2O/THF and the following reduction method: a) $NaBH_4$ reduction of the palladium salt; b) using the UV reduction method ; c),d) letting the material for 15 days in the salt solution.

We believe that this tendency is due to the different time scales involved in the impregnation/reduction process. The first characteristic time is the solvent diffusion typical time inside the matrix (τm) whereas the second characteristic time involves the chemical reduction time scale (τR). With $NaBH_4$ and UV ray, $\tau_R \ll \tau_D$ and some metallic particles appears at the surface of the matrix as soon as the solvent enters the matrix. Thus, most of the ionic species are reduced before they have the time to diffuse inside the polymer matrix. This explains why one observes the presence of large aggregates located close to the surface of the monoliths while the

inner part of the matrix remains almost completely free of metallic nanoparticles. In the last case (fig. 3c, when neither UV light nor $NaBH_4$ are used), $\tau_R \gg \tau_D$ and the solvent can diffuse inside the matrix to react with the polymer matrix and the particles generation takes place only when the matrix are completely filled by the salt solution. Therefore, we decided to perform the following study only with the samples obtained by the third process (i.e. with the samples that were impregnated by the salt solution for 15 days). Qualitative and quantitative comparisons of the results obtained with these 3 different techniques are exposed in table 1. A typical TEM picture of the materials obtained with this technique is shown on figure 3c. The particles are highly dispersed in the polymer matrix and no aggregation phenomenon occurs. As explained above, we believe that this is due to the very slow time scale involved in this process.

3.2.4. Palladium Salt Concentration

The amount of palladium is also a critical parameter that needs to be high [5] or low [17] depending on the targeted applications. In our case, the concentration of palladium salt in the solution appears to be of primary importance for the control of the final palladium loading (see figure 4-a). Just by varying $[K_2PdCl_4]$ between 10^{-3} M and 5.10^{-2} M, the final loading can be adjusted between 0.3 % and 6 % respectively. Moreover, the size of the nanoparticles (figure 4-b) and their spatial distribution in the matrix are not affected by this change in salt concentration. Playing with this parameter appears to be the simplest method to tailor the PHP/Pd support to the targeted application.

4 Catalysis

We have tested the ability of these materials to catalyze organic reactions. This part is just a quick test of what can be achieved with this type of materials and should certainly not be considered as a complete study. The aim of this section is to compare our material with more standard systems such as commercial palladium/carbon supports. For this purpose, we have used the hydrogenation of allyl alcohol into 1-propanol [18] as a test-reaction :

$$H_2C{=}CH{-}CH_2OH \xrightarrow[THF]{H_2} H_2C{-}CH{-}CH_2OH$$

Table 1: Influence of the reduction method on the materials ($[K_2PdCl_4]=10^{-2}$ M; Initiator $[K_2S_2O_8]$ = 0.25 %; Solvent H_2O/THF)

Reduction Method	Pd loading (weight %)	Mean size (nm)	Standard deviation (%)	Spatial distribution
Auto-reduction	2.2	13.8	19	Homogeneously dispersed
UV	6	12.7	20.4	Very aggregated
$NaBH_4$	3.8	7.4	26.6	Very aggregated

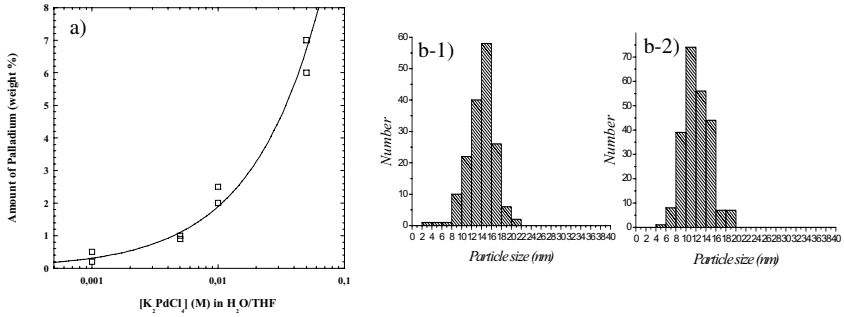

Figure 4: a) Palladium loading versus palladium salt concentration. The solid line is a guide to the eye. Initiator $[K_2S_2O_8]$ = 0.25 %; Solvent H_2O/THF; b) Size histograms obtained from the analysis of TEM micrographs of hybrid Pd/PHP materials impregnated with a water/THF mixture and a salt concentration of b-1) 10^{-2} M, b-2) $5 \cdot 10^{-2}$ M. (Initiator $[K_2S_2O_8]$ = 0.25 %; Solvent H_2O/THF):

A qualitative measurement of the conversion rate has been made by comparing the surface area of each peaks obtained by gas chromatography. The comparison of PHP/Pd materials obtained with auto-reduction method is made with commercial Pd/C 5 %. We have used appropriate quantities for the reaction time to be equivalent for both materials.

On figure 5, we plot the percentage of conversion as a function of time for three different systems: i) Pd/C ii) Pd/PHP as a monolith iii) Pd/PHP powder. First, one note that the three systems eventually lead to the same amount of propanol in the system after 60 minutes. Secondly, we observe that the support efficiency is strongly enhanced when transformed into a powder. In that case, the amount of formed propanol varies from around 20 % to 80 % after 20 minutes. This can be explained by the time for the reactant to diffuse through the bulk material. Then, we have checked the support ability to be used several times in a row (figure 6). This test was performed with the monolith and clearly evidences that the catalytic activity of the material in-

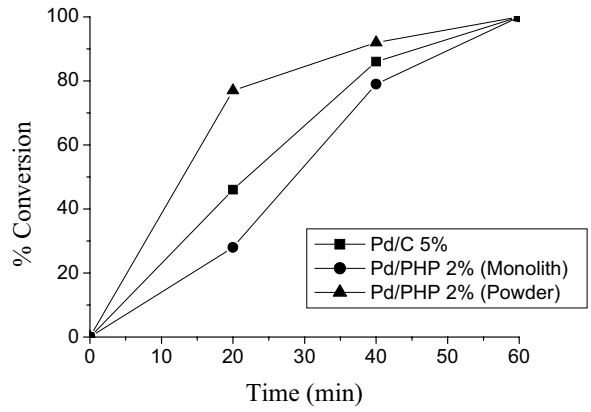

Figure 5: Kinetic evolution of the conversion ratio for the 3 studied systms

creases as function of the number of performed runs. Two reasons can be proposed to explain this behavior: i) after the first run, the material is slightly broken, some fractures being observed in the monolith. This most probably tends to favor the solvent flow inside the monolith thereby increasing the reaction rate ii) as revealed by the XPS experiments, some of the particles were made of PdO instead of metallic zerovalent palladium.

PdO exhibits no catalytic activity. Then, the delay before the start of the reaction can probably be partly attributed to the characteristic time required to first reduce the PdO particles before they can act to catalyze the reaction. In the future, we believe that a significant improvement of the supports could be obtained by the following processes: i) a prior H_2 treatment or a storage of the support in reductive solution ii) use the material in a different shape, for example by making small polyHipes beads. In a last point, we should add that the obtained palladium supported matrix could not be efficiently used for the catalysis of reaction in an oxidizing medium. In that case, we observed a poor activity and an important solubilization of the nanoparticles during the reaction. We believe that this is due to weak particles stabilization at the surface of the polymer support. This might be widely improved by the previous functionnalization of the polymer matrix with organic functions that are known to stabilize nanoparticles. Further experiments are currently under way in our laboratory to improve the catalytic activity of our support in an oxidizing medium.

5 Conclusion

This work deals with the generation of palladium nanoparticles in macroporous polymer matrix and their use as catalytic support for organic synthesis. We show that it is possible to grow metallic palladium particles at the surface of the polymer matrix by plunging the support in a palladium solution. We examine the different experimental parameters of the particles generation that are the initial palladium concentration in the solution, the solvent used to fill the matrix, the polymerization initiator and the palladium reduction method. By tuning these different experimental parameters, the particles aggregation states, size distributions, positions and, over all, the macroscopic sample homogeneity can be tuned and up-grated. We checked the Pd on polyHipes

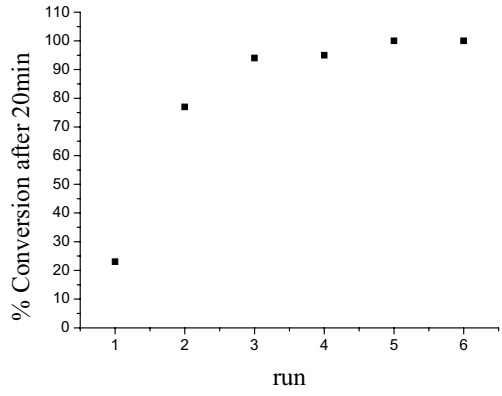

Figure 6: Evolution of the conversion ratio after 20 minutes as a function of the number of reaction cycles

(Pd/PHP) catalytic properties with a basic hydrogenation reaction and compared the results with the well-known Pd/carbon powder systems. Pd/HIPE monolith type materials first depict a lower hydrogenation yield compared to the Pd/carbon powder system mainly due to the reactant impregnation time into the Pd/PHP monoliths. Also cyclic catalysis reaction can be performed with the Pd/PHP system and the hydrogenation yield becomes better and better from cycle to cycle as the impregnation is step forward increased. Future work will be dedicated toward better nanoparticles stabilization using adequate additives. Some specific treatment will be performed on the host scaffolds in order to reach both high temperature catalysis properties associated and the ability to work under oxidative conditions. Further research directions also include the improvement of the mechanical properties and the shape of the materials, with a particular emphasis toward the synthesis of hybrid Pd/PHP beads. These works are under way in our laboratory.

References

[1] C. A. McNamara, M. J. Dixon, M. Bradley, Chem. Rev., 2002, 102, 3275–3300
[2] A. Biffis, M. Zecca, M. Basato, J. Mol.Cat. A: Chem, 2001, 173, 249–274
[3] A. Roucoux, J. Schulz, H. Patin, Chem. Rev., 2002, 102, 3757–3778
[4] A. B. R. Mayer, J. E. Mark, S. H. Hausner, J. Appl. Polym. Sci., 1998, 70, 1209–1219
[5] H.-U. Blaser, A. Indolese, A. Schnyder, H. Steiner, M. Studer, J. Mol. Catal. A: Chemical, 2001, 173, 3–18
[6] M. Kralik , A. Biffis; J. Mol. Cat. A: Chem, 2001, 177, 113–138
[7] R. Nayaranan , M. A. El-Sayed , J. Am. Chem. Soc., 2003, 125, 8340–8347
[8] D. Barby, Z. Haq, U.S. Patent, 4 522 953, 1985
[9] N. R. Cameron, A. Barbetta, J. Mater. Chem., 2000, 10, 2466
[10] N. R. Cameron in Monolithic Materials (F. Svec, T.B. Tennikova and Z. Deyl), Elsevier Science, 2003
[11] H. Deleuze, B. Maillard, O. Mondain-Monval; Bioorg. Med. Chem. Lett., 2002, 12, 1877–1880
[12] B. Corain, M. Zecca , K. Jerabek, J. Mol. Catal. A: Chemical, 2001, 177, 3–20
[13] M. T. Swihart; Current opinion in colloid and interface science, 2003, 8, 127–133
[14] J. H. Adair, E. Suvaci ; Current opinion in Colloid and Interface Sci., 2000, 5, 160–167
[15] M. Brun , A. Berthet, J. C. Bertolini; J. Electron microscopy and related phenomena, 1999, 104, 55–60
[16] P. H. Wang, C.-Y. Pan; Colloid Polym. Sci., 2001, 279, 171–177.
[17] S. Ye, K. V. Ashok, L. H. Dao, J. Electrochem. Soc., 1997, 144(1), 90–95.
[18] C.-W. Chen, T. Serizawa, M. Akashi; Chem. Mater., 1999, 11, 1381–1389.

Empirical Modeling of the Nanocrystallization Process During Devitrification of an Al-based Metallic Glass

David Jacovkis, Javier Rodriguez-Viejo, Maria Teresa Clavaguera-Mora
Universitat Autònoma de Barcelona, Grup de Física de Materials I, Bellaterra.
Narcís Clavaguera
Universitat de Barcelona, Departament d'Estructura i Constituents de la Matèria, Barcelona.

1 Introduction

Al-TM-RE amorphous alloys (where TM is a transition metal and RE a rare earth) have raised great interest since they were first observed in 1988 [1, 2], mainly due to the mechanical properties that some of them present [3, 4]. Those properties can be significantly improved in some materials by promoting the proper microstructure in the samples. It has been shown that a dispersion of primary fcc-Al nanocrystals embedded in the amorphous matrix can increase the strength of the amorphous alloy, though the optimum values of nanocrystallized fraction and grain size must be explored experimentally. Typical optimum values are 30% of nanocrystallized volume and a mean grain size of 10nm [4, 5].

This paper focuses on the study of the primary crystallization process in an Al-rich AL-TM-RE amorphous alloy, with special emphasis on the mechanisms that control the final microstructure of the samples and their thermal stability. The most important source of information about the crystallization of amorphous alloys is the study of calorimetric data. Differential Scanning Calorimetry (DSC) allows the evolution of the crystallized fraction to be followed in both isothermal and continuous heating regimes, and provides a measure of the heat released during the process. But in order to explore the mechanisms that control the transformation, some assumptions must be made about the crystallization kinetics. In this paper we present a new approach to deal with continuous heating DSC data, based on the isokinetic hypothesis.

2 Empirical Modeling

2.1 Isokinetic Hypothesis

The method we propose for the analysis of calorimetric data is based on the isokinetic hypothesis, which states that the evolution of the transformed fraction can be described by a first order differential equation, separable in time and transformed fraction, under continuous heating with a heating rate β.

$$\frac{dx}{dT} = \frac{K(T)}{\beta \cdot P(x)} \tag{1}$$

Throughout this article we will use x to refer to the transformed fraction of primary crystallization, so that $x = 1$ just before the secondary precipitation begins.

Equation (1) is relevant for the analysis of the calorimetric data, because the transformation rate is proportional to the heat flow between the sample and the environment during the transformation, which is the magnitude measured by the calorimeter.

We will assume, as is commonly accepted for thermally activated transformations, that the dependence of the transformation rate with temperature obeys a dimensionless arrhenian equation,

$$K(T) = e^{-E_{ap}/RT} \quad , \tag{2}$$

where E_{ap} is the apparent activation energy of nanocrystallization.

Since Eq. (2) depends only on temperature, the kinetic information is contained in the function $P(x)$. The knowledge of this function also allows the evolution of the transformed fraction x to be predicted under an arbitrary thermal path in the isokinetic range, by solving the integral form of Equation (1):

$$\int_0^{x(t)} P(x')dx' = \int_0^t K(T(t'))dt' \tag{3}$$

This integration will lead to an *isokinetic solution* of the form $x = x(t)$.

2.2 Determination of the Activation Energy: Master Curve Method

Since Eq. 3 does not depend on the heating rate, we can use it to deduce a temperature transformation that takes us from any heating rate β_i to an equivalent one, β_{eq}:

$$\frac{1}{\beta_i}\int_{T_0}^{T_i} K(T')dT' = \frac{1}{\beta_{eq}}\int_{T_0}^{T_{eq}} K(T')dT' \tag{4}$$

Assuming the shape given in Eq. (2) for $K(T)$, we can integrate for $E_{ap} >> RT$:

$$\frac{1}{\beta_i}T_i^2 \quad e^{E_{ap}/RT_i} = \frac{1}{\beta_{eq}}T_{eq}^2 \quad e^{E_{ap}/RT_{eq}} \tag{5}$$

Given a set of calorimetric curves obtained at different heating rates β_i, we can use the last equation to convert them all to a single equivalent heating rate β_{eq}, with E_{ap} as the only parameter. We will take the value of E_{ap} that leads to a better overlapping of the curves, evaluated by applying the least squares method to the averaged *master curve* and each of the transformed curves (see Figure 1).

Note the similarities between this method and the widely used Kissinger method, which is based on the same assumptions but takes profit of only one experimental point from each curve (the maximum of the calorimetric peak), while the method we propose uses the shape of the whole peak.

2.3 Kinetic Analysis

Once the activation energy has been determined, the *master curve* can be used to explore the mechanisms that drive the crystallization. Equation (1) can now be expressed in terms of the *master curve*, so we can obtain function $P(x)$ from the experimental data:

$$P(x) = \frac{1}{\beta_{\mathrm{eq}}}\left[\frac{dx}{dT_{\mathrm{eq}}}\right]^{-1} e^{-E_{\mathrm{ap}}/RT} \tag{6}$$

The study of this function can help us to identify the most relevant mechanisms in different stages of the process.

Let us consider this function in the context of the Kolmogorov-Johnson-Mehl-Avrami (KJMA) theory. In this framework the transformation is considered to take place in an *extended volume*, without geometrical impingement between growing grains. The extended transformed fraction is related to the real one by:

$$dx = (1-x)dx_e \tag{7}$$

Many kinetic models use for x_e the general form proposed by Avrami,

$$x_e = \left(K(T)\cdot t\right)^n , \tag{8}$$

where n is the *Avrami exponent*, which can be interpreted in terms of growth dimensionality and time evolution of the nucleation frequency [6].

In the KJMA framework we can obtain a functional form for the kinetic function $P(x)$, combining Eqs. (6), (7) and (8):

$$P_{\mathrm{Av}}(x) = P_0 \frac{\left[-\ln(1-x)\right]^{\frac{1-n}{n}}}{n(1-x)} \tag{9}$$

When nanocrystallization occurs by growth of pre-existing nuclei with density N, the grain size evolution can be estimated using the transformed fraction, obtained by integration of Eq. (3).

$$x(t) = \frac{4}{3}\pi\, N < r^3 >_t , \tag{10}$$

if site saturation has been reached during quenching (i.e., there are no nucleation sites available for thermally activated nucleation).

3 Experimental Procedure

The amorphous ribbons, of atomic composition $Al_{87}Ni_7Cu_3Nd_3$, were prepared by melt spinning by the group of Prof. A. Inoue in Tohuku University, Sendai, Japan.

DSC curves were acquired in a Perkin-Elmer DSC7 calorimeter under pure Ar atmosphere. The calibration with standard samples (In and Zn) led to an experimental accuracy of ±1K in temperature and 5 % in enthalpy. A second experiment was always performed on the transformed sample in order to subtract the experimental baseline from the original signal.

XRD experiments were performed in a PHILIPS X'PERT diffractometer using a monochromatic Cu-Kα beam, over a 2θ range from 30º to 50º with a step of 0.03º.

4 Results

Figure 1 shows a set of DSC curves corresponding to the primary crystallization, obtained at 10, 20, 40, and 60 K/min. The shape of the curves indicates a rapid onset of the transformation followed by a long tail at all heating rates. The method depicted in Section 2.2 was applied to the curves in order to obtain an averaged *master curve* (also shown in Figure 1), leading to an apparent activation energy of 105±5 kJ/mol. The transformed curves show a good overlapping in all the isokinetic range, with the only exception of the end of the transformation, where also the instrumental error is higher.

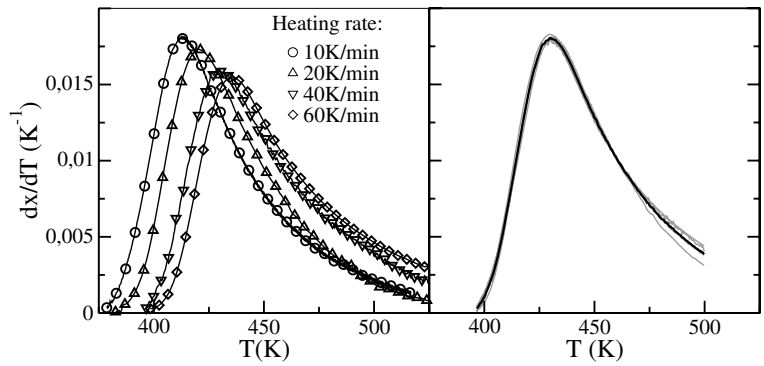

Figure 1: Transformation rate at different heating rates (left), obtained from DSC experiments. On the right, the averaged *master curve* (bold line) and the transformed curves (gray lines), showing good overlapping for E_{ap} = 105 kJ/mol.

This *master curve* was then used to calculate the experimental $P(x)$ curve following Eq. (6). With this operation, the temperature dependence of the transformation rate was extracted from the calorimetric data, so that the remaining curve contained only kinetic information. The analysis of this data provided some insight on the mechanisms controlling the nanocrystallization, especially on its early stages. The $P(x)$ curve can be seen in Figure 2 in continuous line. The curve in dashed line was calculated using the Avrami equation (Eq. (9)) with $n = 3/2$ and $P_0 = 1 \cdot 10^{10}$ s, and fits the experimental data up to a nanocrystallized fraction of $x = 0.05$. This

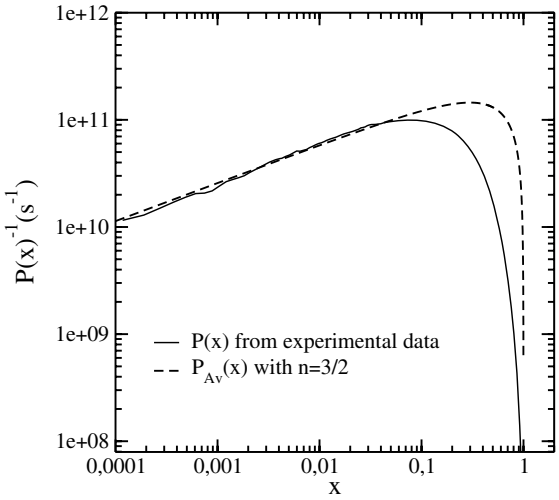

Figure 2: The P(x) curve, as obtained from calorimetric data after extracting the temperature dependence, together with a curve calculated in the Avrami framework, assuming diffusion-controlled growth of pre-existing grains. The curves show good agreement for $x < 0.05$.

value of the Avrami exponent can be associated to a diffusion-controlled growth of pre-existing nuclei with no thermally activated nucleation [REF Christian]. As the transformed fraction increases, the $P(x)$ curve obtained from experimental data deviates from the diffusion-controlled growth model. This indicates a change in the mechanism limiting grain growth.

The good agreement between the experimental data and the Avrami model at the beginning of the transformation seems to indicate that site saturation has occurred in the samples during quenching, inhibiting thermally activated nucleation during heat treatments. This assumption allows us to estimate the grain size evolution for any heat treatment in the isokinetic range, since we can obtain the transformed fraction by numerical integration of Eq. (3).

The result of this calculation can be seen in Figure 3 for a grain density $N = 2 \cdot 10^{17}$ cm^{-3}, together with the theoretical evolution of the mean grain size in the diffusion-controlled grain growth model. As the figure clearly shows, grain growth in the samples becomes slower than parabolic growth short after the grains begin to grow significantly. This fact supports the hypothesis that another mechanism controls grain growth after the first stage. At the end of the transformation both curves converge, as it is expected for a constant grain density, regardless of the mechanisms controlling the process.

The values derived from the *master curve* agree with the experimental points shown in empty circles. These values were obtained by fitting XRD patterns of thermally treated samples with a convolution of the amorphous and nanocrystalline fcc-Al phases. This method is described in detail in [7].

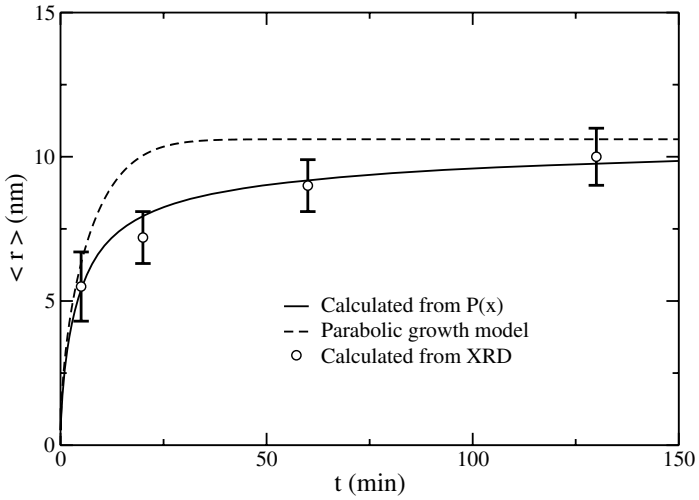

Figure 3: Mean grain size during an isothermal annealing at 383 K, obtained from the *master curve* assuming constant grain density, showing good agreement with the estimations based on XRD data. In dashed line, the result for an Avrami model with n = 3/2:

5 Discussion

The analysis of calorimetric data using the *master curve* method indicates that the transformation begins with a diffusion-controlled growth of pre-existing grains. This is the limiting mechanism until the transformed fraction is ~5 % of the volume available for primary crystallization, as can be seen in Figure 2. In this regime, solute atoms rejected from the growing grain pile up near the interface forming a solute barrier. The rate at which the barrier diffuses away from the interface will limit grain growth.

The same analysis also suggests that the number of grains is constant during the transformation, since the early stages of the precipitation can be described by an Avrami function with n = 3/2[REF Christian], and a significant amount of thermally activated nucleation would lead to a larger value of n. The agreement between grain size estimations obtained from XRD data and the curve calculated assuming constant grain density further supports this assumption.

As nanocrystallization proceeds a new mechanism takes control of the transformation, reducing the growth rate with respect to the diffusion-control regime. This is obvious from Figure 3, where the curves diverge near the beginning of the transformation. This behavior can be due to the overlapping of diffusion fields, known as *soft impingement*. Long before geometric (or *hard*) impingement occurs, the solute diffusion fields associated to adjacent grains will begin to overlap, gradually reducing the concentration gradient ahead of the solute barrier, and therefore slowing grain growth.

The transformation is very slow in the final part of the graph, but it doesn't show a clear end after 150 min annealing at 383 K (see Figure 3). This suggests that the transformation is slowed kinetically due to soft impingement, since there is still a positive driving force for crystalliza-

tion. Therefore, the experimental curve would meet the final value predicted by the hard impingement model, if the sample was kept long enough at that temperature.

6 Conclusions

A new method for the kinetic analysis of continuous heating calorimetric data has been presented. The method, based on the isokinetic approach, has been applied successfully to the nanocrystallization of the $Al_{87}Ni_7Cu_3Nd_3$ amorphous alloy, resulting on a value of the activation energy of 105 kJ/mol. The analysis of the $P(X)$ function has allowed us to explore the mechanisms controlling the transformation. It has been found that the first stages can be described accurately by the diffusion-controlled growth of pre-existing nuclei, probably formed during quenching. The estimated grain density is $N = 2 \cdot 10^{17} cm^{-3}$. After the 5 % of the primary precipitation is completed, the transformation slows with respect to that model, due to soft impingement. This mechanism controls the nanocrystallization until the end of the process.

7 Acknowledgements

This work was supported by the Comisión Interministerial de Ciencia y Tecnología (Projects No. MAT2000-0388-C02 and MAT2001-2532) and the Comissió Interdepartamental de Ciència i Tecnologia (Project No. 2001SGR-00190). D. Jacovkis thanks the financial support granted by the Universitat Autònoma de Barcelona.

8 References

[1] A. Inoue, K. Ohtera, A.P. Tsai, T. Masumoto, Jpn. J. Appl. Phys. 1988, 27, L280
[2] Y. He, S.J. Poon, G.J. Shiflet, Science 1988, 241, 1640
[3] A. Inoue, Materials Science and Engineering 2001, A304–306,1
[4] Z. C. Zhong, X. Y. Jiang, A. L. Greer, Materials Science and Engineering 1997, A226–228,531
[5] Y.H. Kim, A. Inoue, T. Masumoto, Mater. Trans. JIM 1991, 32, 331.
[6] J. W. Christian, The theory of transformations in metals and alloys, 2nd ed., Pergamon Press, Oxford, 1975, p. 542
[7] D. Jacovkis, Y. Xiao, J. Rodriguez-Viejo, M. T. Clavaguera-Mora, N. Clavaguera, Acta Mater., submitted.

Numerical Modelling of Frequency and Field Dependent Relaxation Time in Soft Magnetic Amorphous Ribbons

I. Z. Rahman[1], A. Boboc[1], Md. Kamruzzaman[1] and M. A. Rahman[2]
Magnetics Research Laboratory, Materials and Surface Science Institute (MSSI)
[1] Department of Physics
[2] Electronic & Computer Engineering Department
University of Limerick, National Technological Park, Limerick, Ireland

1 Introduction

In this paper we have modelled the MI effect in soft magnetic amorphous ribbons using a micromagnetic model and an extension of the Machado et al.[1] formulation. Soft magnetic metallic glass wires and ribbons shows Giant Magneto-Impedance (GMI) effect which is the large variation of magneto-impedance (MI) in soft magnetic materials induced by a small dc magnetic field in the presence of a relatively high frequency ac field. This has attracted wide interest because of its application as magnetic field and current sensors and for studying this effect from micromagnetics point of view. The basic mechanism for MI phenomenon is the change of magnetic penetration depth inside a material that induces modification of the transverse magnetic permeability [1–3]. GMI or MI effect has been found to be dependent on relaxation time that can be defined as the magnetic delay in response to the high frequency filed due to the combined effect of an ac and a dc magnetic field. The application of axial dc magnetic field, which is applied in the longitudinal direction of the ribbons changes the transverse permeability. The transverse domain spins are reoriented toward the ribbon axis. As the dc field increases, the transverse permeability, μ_t decreases and the skin depth, d increases. At high frequencies, the effective cross-section of the conducting magnetic ribbon is modified causing a large decrease in ac impedance (Z). The impedance of a sample can be expressed [4] using classical electrodynamics as,

$$Z = \frac{(1-j)L}{2lc}(2\pi\rho\omega\mu_t)^{1/2} \tag{1}$$

where, ρ is the resistivity, c is the velocity of light, l and L are the ribbon width and length respectively. The above relationship shows that Z depends on the dc field and frequency ($\omega\mu_t$), which, in turn depends on the response of the domains to the longitudinal dc field and the ac excitation.

MI effect is expressed as *MI Ratio* and mathematically can be expressed as:

$$MI\ \ Ratio = \frac{\Delta Z}{Z(H_S)} \cdot 100(\%) = \frac{Z(H) - Z(H_S)}{Z(H_S)}\ \cdot\ 100(\%) \tag{2}$$

where, $Z(H)$ is the impedance of the metallic glass wires or ribbons in zero dc magnetic field and $Z(H_S)$ is the impedance at saturation dc field, in the presence of an ac excitation. This is illu-

strated in Figure 1. At higher frequencies after reaching the maximum, MI values decrease since the excitation field flows through a very thin layer near the surface and the sample becomes insensitive to the ac field.

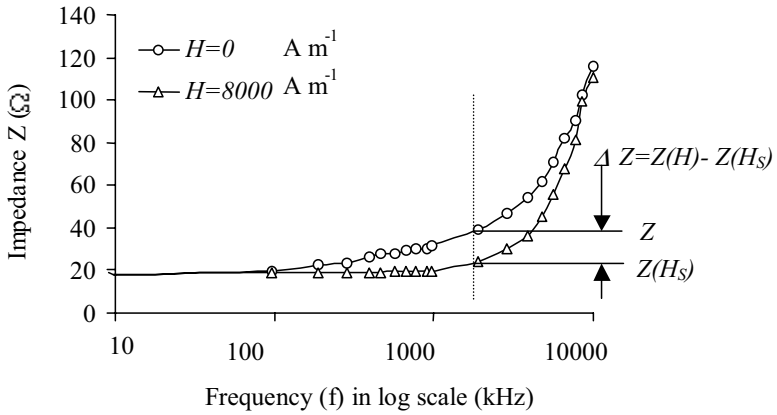

Figure 1: Comparison between Impedance profiles at H_{dc} = 0 and at H_{dc} = 8000 A m^{-1} at frequency range from 100 kHz to 10 MHz for an amorphous magnetic ribbon of composition $(Co_{95}Fe_5)_{70}Si_{12}B_{18}$

2 Phenomenological Models for GMI Effect

The research on GMI phenomenological model started in order to understand the experimental data found in metallic glasses. Santos et al.[5] has proposed a model of the domain structure and assumed that a metallic glass ribbon has transverse domain structure. When an ac current flows through the ribbon, a transverse magnetic field is induced around it. MI effect is observed when an axial dc field comparable to magnitude of saturation field H_S is applied parallel or perpendicular to the sample. The motion of the magnetic domain walls, which results from the combined effect of the external axial field, H_{dc} and the transverse ac field H_{ac} created by the ac current, I_{ac} is depicted in Figure 2**.** There one can see that an increase in the axial dc field will decrease the angle of distribution of the net field.

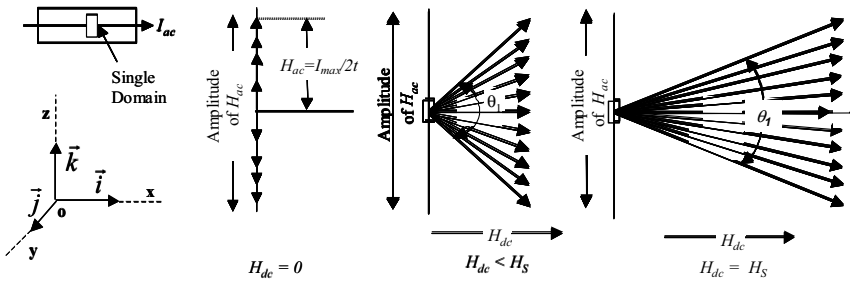

Figure 2: Domain wall model under the influence of combined ac and dc field

Using the same concept described in Figure 2, Machado et al [1,2] presented a semi-empirical model for Co-rich metallic glass ribbons based on the electromagnetic skin depth effect and on the domain wall motion due to the magnetic field and ac current, which explained the MI spectra and its frequency and field dependence. Machado considered two neighbouring domains that have spins opposite to each other as shown in Figure 4 where the magnetic spin direction of a single domain in respect with the *x-axis* (angle θI) depends of the amplitudes of ac and dc field that are applied to the sample.

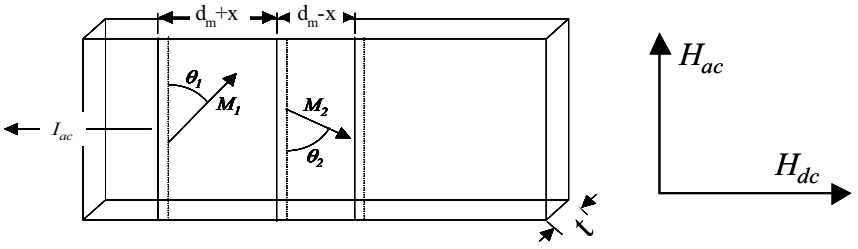

Figure 3: The net magnetization direction of two neighbouring domains due to the application of both ac and dc magnetic field at a certain time [ref 1]

Here θ_1 and θ_2 are the angles between the two domain magnetization directions with the easy axis direction, d_m is the domain width, x is the wall displacement, t is the ribbon thickness and H_{ac} and H_{dc} are the ac and dc field respectively. Since the current flows along the two surfaces, one can analyze only the behaviour of the domain on one surface. Assuming initially quasistatic condition, the domain wall displacement (x) from the equilibrium configuration ($H = H_{ac} = 0$) and the direction of the domain magnetizations are obtained by minimizing the free energy density U_{total}. This is the sum of the Zeeman, anisotropy, transverse Zeeman and wall energy contributions respectively. The angles θ_1 and θ_2 and the can be obtained by minimizing the total energy density equation:

$$\frac{\partial U_{\text{total}}}{\partial \theta_1} = \frac{\partial U_{\text{total}}}{\partial \theta_2} = \frac{\partial U_{\text{total}}}{\partial x} = 0 \tag{3}$$

By solving the Equation (3) followed by several mathematical steps one can find the equation for transverse susceptibility as follows:

$$\chi_t = \frac{M_t}{H_{\text{ac}}} = \frac{M_S}{H_{\text{ac}}} \left(\frac{1}{2}\left(\cos\theta_1 - \cos\theta_2\right) + \frac{\chi}{d_m}\left(\cos\theta_1 - \cos\theta_2\right) \right) \tag{4}$$

where, χ_t and M_t are transverse magnetic susceptibility and magnetization respectively.

At high frequencies $\chi_t \cong \mu_t$. The frequency dependence of transverse susceptibility can be obtained from the analysis of the domain dynamics. In Machado's model it has been assumed that the domain dynamics is limited by the wall motion and not by the magnetization rotation.

Assuming that an alternating transverse field ($he^{i\omega t}$) is generated by the ac current and neglecting the magnetic domain wall mass, Machado obtained, from Equation (4), the following expression for transverse susceptibility χ_t:

$$\chi_t = \frac{\chi_0}{1 - i\omega\tau} \tag{5}$$

where, τ is the relaxation time and χ_0 is the static susceptibility (at $f = 0$).

Finally, Machado derived that the impedance of the metallic glass ribbon which shown in Equation 1 and can be rewritten considering the dependence on the relaxation time and the frequency as follows:

$$Z = \frac{L}{2lc}\left(\frac{4\pi\rho\omega}{1+\omega^2\tau^2}\right)^{1/2}\left[\left(1+\omega^2\tau^2+4\pi\chi_0\right)^2+\left(4\pi\chi_0\omega\tau\right)^2\right]^{1/4} \tag{6}$$

3 Landau-Lifshitz-Gilbert Approach to Study MI Effect

Experimental measurements give us information about macroscopic magnetic parameters. With the practical imaging techniques such as MFM, MOKE one can obtain information of the magnetic domain distributions only at the surface of the ribbons. We analyzed the MI effect also by using the Landau-Lifshitz-Gilbert formalism. This attempt is different from the Machado approach and considers the effect of rotation (damping) of the magnetization spins with respect to the applied field. In the micromagnetic simulation approach, an equilibrium magnetization configuration of a ferromagnetic body can be found by minimizing its total Gibbs free energy E_{total}, which can be written as sum of several energy contributions due to various effects such as anisotropy, exchange, demagnetization and Zeeman:

$$E_{\text{total}} = E_{\text{anisotropy}} + E_{\text{exchange}} + E_{\text{demag}} + E_{\text{Zeeman}} \tag{7}$$

In general, an effective field H_{eff} acting on a given magnetic moment can be defined as the derivative of energy with respect to magnetization:

$$H_{\text{eff}} = -\frac{1}{\mu_0}\frac{\partial E_{\text{total}}}{\partial M} \tag{8}$$

At equilibrium, the magnetisation vector M is parallel to H_{eff} and the total free energy reaches a minimum. The magnetisation configuration satisfying this condition is usually computed by integration of the Landau-Lifshitz-Gilbert (LLG) equation and given by,

$$\frac{\mathrm{d}\vec{M}}{\mathrm{d}t} = -\gamma\left(\vec{M}\times\vec{H}_{\text{eff}}\right) - \frac{\alpha}{M^2}\left(\vec{M}\times\left(\vec{M}\times\vec{H}_{\text{eff}}\right)\right) \tag{9}$$

where, M_s is the saturation magnetization, γ is the Landau-Lifshitz gyromagnetic ratio and α is the Gilbert(Landau) damping coefficient.

To implement this formalism we have used the OOMMF package [6], which solves Equation (9) by implementing a first order forward Euler method with step size control on the Landau-Lifshitz ordinary differential equation. Conventional terms for the various contributions to the local field and energy are included in the calculation. The exchange energy is computed via a six neighbour bilinear interpolation described in reference [7], with Neumann boundary conditions and the magnetostatic energy is calculated using a Fast Fourier Transform based scalar potential [6]. This original code has been built for micromagnetic modelling and we have adapted for the study of the MI effect. In this way we were able to observe the formation and movement of the magnetic domain walls inside the sample in function of frequency and field. One can also obtain the 3D distribution of the magnetization vector inside the sample that cannot be measured experimentally.

4 Results

4.1 Further Work on Machado's Model

We have already reported on the extension of the Machado model as referred in [8]. Machado used the relaxation time (τ) calculated from dynamical susceptibility and values of Z were calculated using Equation (6). By inverting the Equation (6) the dependence $Z = Z(\tau)$ can be transformed in $\tau = \tau(Z)$, having the following expression for the relaxation time:

$$\tau = \left[\frac{\omega^2 L^4 \pi^2 \rho^2 \left(1 + 4\pi\chi_0\right)^2 - l^4 c^4 Z^4}{l^4 c^4 z^4 \omega^2 - \omega^4 L^4 \pi^2 \rho^2} \right]^{\frac{1}{2}} \tag{10}$$

Our goal has been to simplify Equation (10) by using a mathematical fitting technique described in reference [7] and taking into account the variation of the relaxation time with field and frequency. Experimentally obtained data on magneto-impedance of Fe and Co based ribbons were used for calculating the relaxation time as a function of frequency and dc magnetic field. The numerical technique has two steps as follows [8]:

Step one: a general expression shown in the Equation (6) can be converted to the following form:

$$\tau_{\mathrm{FIT1}} = \tau_1 + \tau_2 = a_0 e^{a_1 f} + a_2 f \tag{11}$$

The two components τ_1 and τ_2 are used to fit relaxation time as functions of frequency at a certain value of the field are pictured in Figure 4(a). It was observed that parameter a_0 is nearly independent of the axially applied dc field, the values of a_1 and a_2 increases with the field as shown in Figure 4(b) as an example.

Step two: we considered the approximation of the first fit parameters by implementing their dependence with the applied dc magnetic field as shown in the Equation (12):

$$a_0(H) = c_0 \, a_1(H) = -\frac{c_1}{\sqrt{H}} \quad a_2(H) = c_2 + c_3 H^2 \tag{12}$$

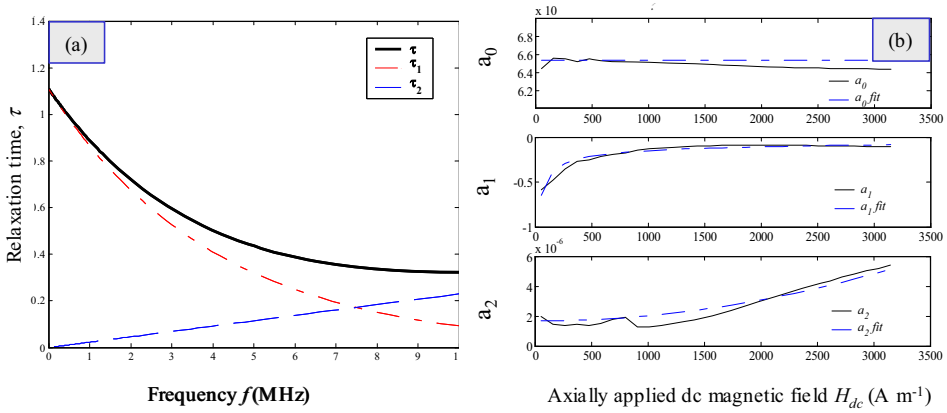

Figure 4: (a) Relaxation time components and (b) Relationship between a_0, a_1 and a_2 parameters as a function of axially applied dc magnetic field

where, c_0, c_1, c_2, c_3 are constants that depend on the intrinsic magnetic properties of the sample.

In Figure 4b a_i and $a_i fit$ represent the values by fitting with Equation 11 and Equation 12 respectively. Using Equation (7) and (8), the final expression for τ takes the following form:

$$\tau_{FIT2} = c_0 e^{-\frac{c_1 f}{\sqrt{H}}} + \left(c_2 + c_3 H^2\right) f \tag{13}$$

Experimental data on several metallic glass ribbons were used and the parameters c_0, c_1, c_2 and c_3 are extracted for each ribbon by implementing the fitting algorithm as previously described.

Evolution of the relaxation time for ($Co_{67}Fe_4Mo_{15}Si_{16.5}B_{11}$) ribbons as a function of frequency for two field values is shown in Figure 5 as an example:

The MI effect, described by the Equation (1), with an applied dc magnetic field H_{dc} has been analysed. Figure 6 (a) to (c) show the plots of calculated dc field dependent *MI Ratio* and the experimental values for metallic glass ribbons with nominal compositions at three different frequencies where the ribbons show maximum *MI Ratio*.

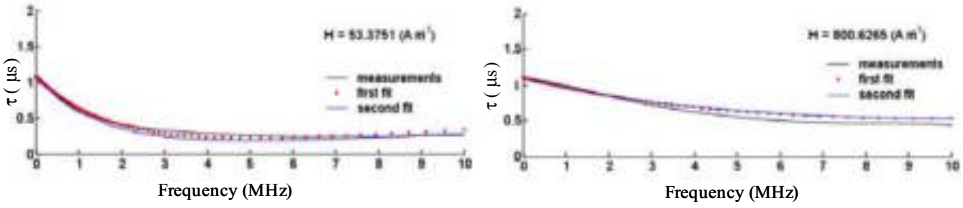

Figure 5: Relaxation time as a function of frequency for ribbon with nominal composition of $Co_{67}Fe_4Mo_{1.5}Si_{16.5}B_{11}$

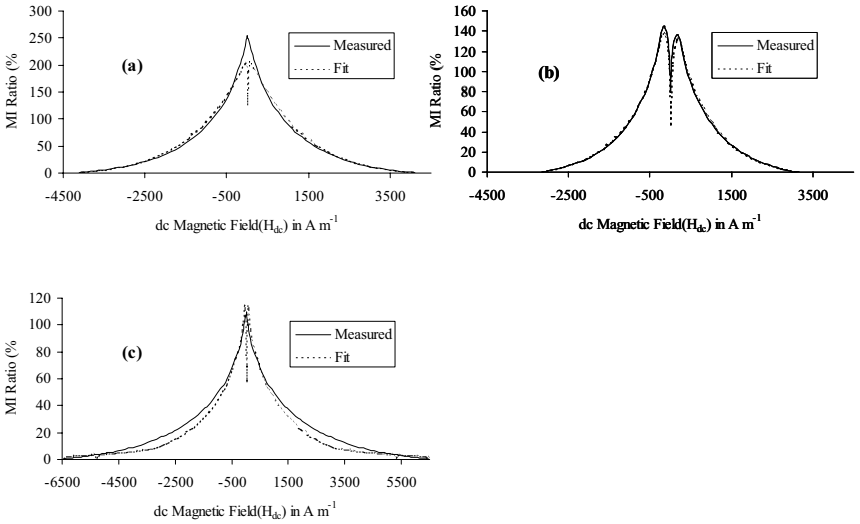

Figure 6: Plot of *MI Ratio* as a function of bias dc magnetic field from experimental and simulation results on metallic glass ribbons of nominal compositions **(*a*)** $Co_{71}Fe_1Mo_1Mn_4Si_{14}B_9$, maximum *MI Ratio* found at 2 MHz, **(*b*)** $Co_{67}Fe_4Mo_{1.5}Si_{16.5}B_{11}$, *MI Ratio* found at 8.7 MHz and **(c)** $Co_{71}Fe_2Mn_4Si_{14}B_9$, maximum *MI Ratio* found at 3.8 MHz

Calculated values of the *MI ratio* agree well with our experimentally measured *MI ratio*, see Figures 6 (a) to (c). In all cases, *MI ratio* increases with the frequency, showing a maximum at a certain frequency value and then decreases slowly. The small differences between the calculated and the experimental values can be explained by recalling the assumptions that are taken in the Machado et al. [1, 2] originally proposed model. In the first approximation, they assumed that the domain dynamics was limited by the wall motion and not by the magnetization rotation. But in a real situation, the domain dynamics is rather complex. At low frequency, the domain wall motion dominates magnetization. At intermediate frequency, the magnetization proceeds partly due to the domain wall motion and partly due to the magnetization rotation. At higher frequency, magnetization is purely rotational. The frequency range of low, intermediate and high frequency is not well defined and it varies from material to material that have different magnetic and physical properties.

5 Study of Magnetization Dynamics of the Ribbons Using LLG

We considered a distribution of the dc and ac magnetic field in the sample that can be expressed as follows:

$$\vec{H}_{\text{total}}(z,t) = H_{\text{dc}}\,\vec{i} + H_{\text{ac}}(0)e^{-z/\delta}\sin(2\pi f t)\vec{k} \tag{14}$$

where, δ is the penetration depth of the ac field, f is the frequency of the ac field, $H_{ac}(0)$ is the maximum amplitude of the ac field at the surface of the ribbon, H_{dc} is the amplitude of the dc field, t is the time and z is the distance from the surface of the ribbon to the inner side along the *z– axis* in Cartesian co-ordinate system.

The calculation is to find the best matching parameters for an impedance value close to the experimental measured one.

The information obtained from this simulation can provide not only the value of the susceptibility of the sample but also details about 3D distribution of the magnetic spins and magnetic domain inside the sample that is not possible to achieve experimentally. From the 3D magnetization map it is possible to see how the combination ac and dc field affects the magnetic spins and how are our results in respect with the Machado model predictions.

We must mention here that the Machado model is a semi-empirical model that is based on the measure of macroscopic parameters as impedance or frequency of the field but do not have the ability to introduce constraints that depend of the internal distributions of the magnetic spins.

Figure 7 shows the magnetization (spins) distribution at different cross-section at the surface (x = 0 and z = 0) and inside of the ribbon under the influence of a combined ac and dc magnetic field.

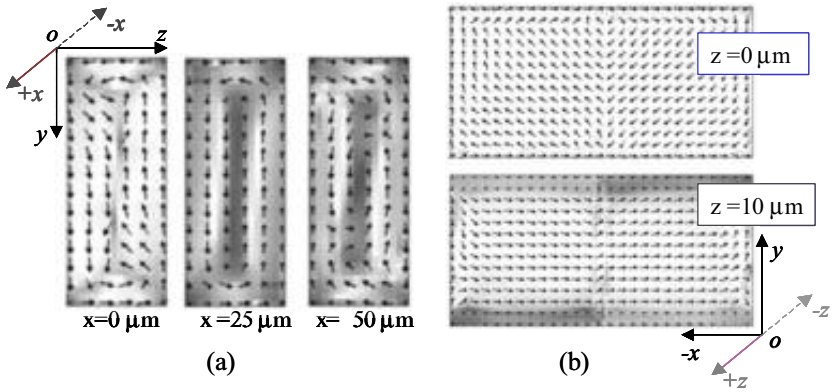

Figure 7: Magnetization vector distribution along (a) *x-axis* and (b) *z-axis* at various depth inside a ribbon with dimensions (100 × 50 × 20 µm^3) under the combined action of a dc magnetic field (1200 A m^{-1}) and an ac field (Amplitude = 375 A m^{-1} at 2.89 MHz)

As can be noticed, the magnetization dynamics in very different in the two cases. In the middle of the ribbon the formation of more like domains. One can, by analyzing the evolution in time and space of the magnetization spins, find important characteristics regarding domain wall formation and movement. By comparing the simulated values of the relaxation time with the experimental measurements, an evaluation of the Landau damping factor, that is an intrinsic property of the material, can be made.

6 Conclusions

In the present study, the behaviour of the relaxation time at different field and frequency were analysed and a simplified model consisting of parameters that depend only with the intrinsic properties of the materials has been proposed. MI values were compared with a model proposed by Machado et al. According to this model, the impedance of the ribbon is related to the relaxation time. It was observed that the relaxation time obeys linear relationship with frequency at high magnetic field and an exponential relationship at low field. To this end, a general expression of the relaxation time as a function of ac frequency and dc bias magnetic field for soft magnetic ribbons was established.

On the other side, the LLG approach reveals important 3D characteristics of the MI phenomena.

7 Acknowledgements

This work is partly supported by EU under Marie Curie Host Development Fellowship Grant Scheme, Enterprise Ireland STRG grant scheme and the University of Limerick Postgraduate Research Fund.

8 References

[1] F. L. A. Machado et al., J. Appl. Phys., 1996, 79, 6558
[2] F. L. A. Machado et al., Physical Review B-Condensed Matter, 1995, 51, 3926
[3] Panina, L.V. Mohri, K. Bushida, M. Noda,, IEEE Trans. on Mag., 1995, 31, 1249–1260
[4] J. D. Jackson, Classical Electrodynamics ,Wiley, New York, 1975
[5] A. D. Santos, L. G. C. Melo, C. S. Martins, F. P. Missel, Journal of Applied Physics, 1996, 79, 6546-6548
[6] M. J. Donahue and D. G. Porter, ”OOMMF User’s Guide, Version 1.0,” NISTIR 6376, NIST, Gaithersburg, MD ,1999
[7] Philip R Bevington, ” Data reduction and error analysis for the physical sciences- 2nd ed.”, McGraw Hill, 1992, 237–239
[8] I. Z. Rahma, A. Boboc, Md. Kamruzzaman and M. A. Rahman, ”Numerical Modelling of GMI Effect In Soft Magnetic Amorphous Ribbons”, International Conference On Magnetism , 2003,Roma, Italy, ICM 2003 Abstract book no 5-S pm22, 715

Hierarchical Nano-Structured Design of Metal-Oxide Catalysts

Daniela Habel[1], Jean Boris Stelzer[2], Jürgen Caro[2], Martha-Martina Pohl[3], Egbert Feike[1], Helmut Schubert[1]
[1] Institute for Material Science and Technologies, TU Berlin,
[2] Institute for Physical Chemistry and Electrochemistry, TU Hannover,
[3] Institute for Applied Chemistry, Berlin

1 Introduction

Commonly used catalysts in industry are composed of highly dispersed particles of precious metals or transition metal oxides on oxide supports. Both the particle size and the way of connection between the support and the active compound have a strong influence on the activity and selectivity of the catalysts.

Oxides containing molybdenum or vanadium are effective catalysts for the oxidative transformation of aliphatic and aromatic hydrocarbon. With these easily reducible metal oxides the oxidative dehydrogenation of propane to propene (ODP) runs in accordance with the Mars Van Krevelen mechanism according to which the hydrogen is abstracted by lattice oxygen from the alkane molecule. The anion gap arising is being closed by dissociative adsorption of oxygen from the gaseous phase (redouble oxidation of the catalyst) [1]. Bell and employees [2] [3] concluded from spectroscopic examinations of the ODP that was the dissociation of the C-H relationship and not the redouble oxidation of the catalyst which was kinetically limiting the whole process. It is expected that nano-particles show an increased oxygen diffusion towards the bulkoxides than compact oxide phases and therefore influence the activity of the catalyst positively. The highest propane conversion and propene selectivities were found when the catalyst contains vanadium as a so-called "single sites" on a greatest possible surface [4]. It is therefore expected that catalytic nano-particles on nano-structured surfaces also show a changed selectivity in the partial oxidation.

The activity and selectivity of the catalysts depend decisively on the nature of the molybdenum or vanadium species which are influenced each by the composition and preparation procedure.

Stelzer et al. [5] investigated catalysts with V_2O_5 and MoO_3 based on different supports. The catalysts with MoO_3 were the most selective ones, while the highest propane conversion and yields of propene were achieved with V_2O_5. In this examinations the inert part in the feed was only 40 Vol.% so that propene yield reached with a catalyst consisting of µm-TiO_2-support and 5 wt.% V_2O_5 was only 9 wt.%.

Target: In this work, catalysts with hierarchical nano-structured design were prepared by various ways and their catalytic activity was tested on the basis of the model reaction of ODP. Two TiO_2 supports were successively covered with one or two of the active compounds TiO_2, V_2O_5 or MoO_3. It was examined whether the combination and the order of the active compounds have an effect on the activity of the catalysts. The ”intermediate layer” which consists of a active compound of some nm only and which is located between support and second active compound, is of special interest.

This way a rise of the surface shall be obtained which makes it possible to have the second active compound finely distributed on the intermediate layer surface. It is expected that nano-scaled catalyst particles on nano-structured surfaces show an increased selectivity in the partial oxidation. There are two models of the composition of a catalyst [6] with a support and one or two active compounds (Figure 1).

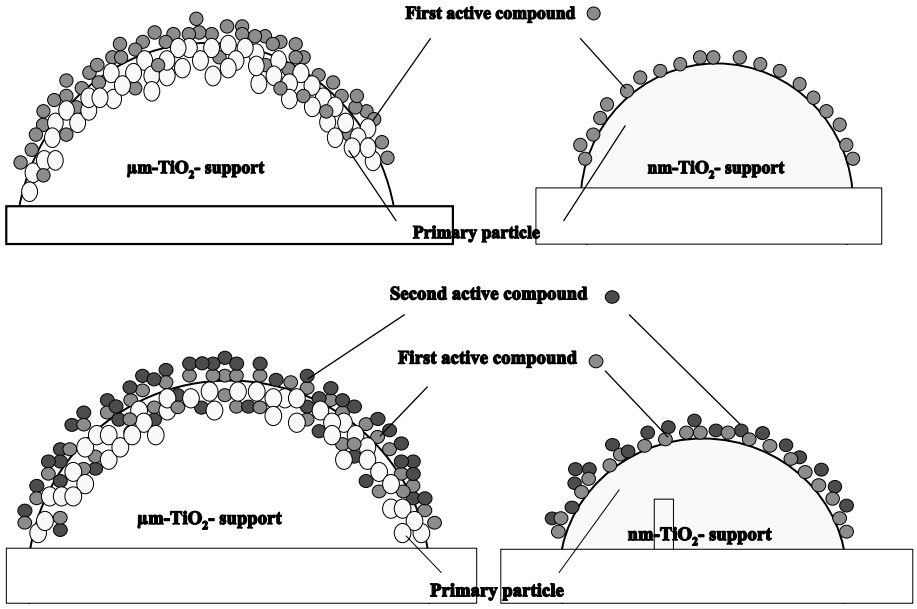

Figure 1: Model of a catalyst built up from a support functionalized by one or two active compounds

2 Preparation

2.1 Preparation of the Supports

2.1.1 µm-TiO_2-support

For the preparation of the µm-support a laboratory spray drier (Anhydro, Denmark) with a drying chamber diameter of 1 m and a water evaporation rate of 7.5 kg/h was used. By the process of spray-drying a commercial TiO_2 powder (anatase) with average 200 nm size primary particles was shaped into approx. 30 µm size granules (Figure 2). For stabilization the granules had to be calcined in the surface diffusion regime (773 K) to encourage neck formation.

2.1.2 nm-TiO_2-support

The nm-support prepared by the hydrolysis of titanylsulfate $TiOSO_4 \cdot 2\,H_2O \cdot H_2SO_4$ at 280 K shows a primary particle size of 30 nm (Figure 2).

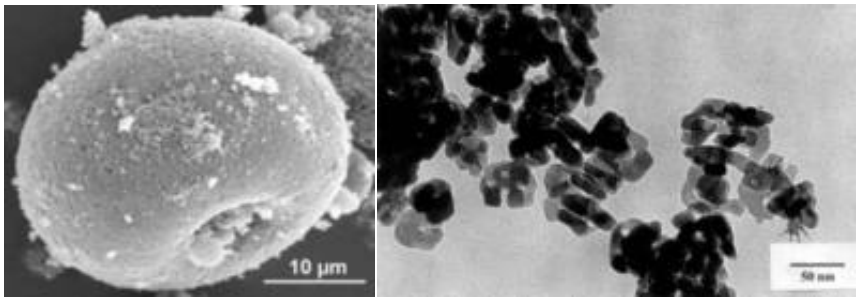

Figure 2: SEM-image of hollow granules as µm-TiO_2-support (left side) and TEM-image of nm-TiO_2-support (right side)

XRD investigations have shown that both the µm-TiO_2-support and the nm-TiO_2-support were found in the anatase modification.

2.2 Preparation of the Catalysts

The transition metal oxides V_2O_5, MoO_3 and TiO_2 were chosen as catalytic active compounds. The two supports with different dimensions will be covered one or two times in various proportions by one or two of these active compounds. The order of application of the active compounds was changed.

Depending of the oxide there are three ways of the preparation.

V_2O_5: The support was mixed with V_2O_5 powder in a vibrating unit and heat treated at 773 K in air. This process is called spreading.

MoO_3: A molybdenum precursor $(NH_4)_6Mo_7O_{24} \cdot 4\ H_2O$ was precipitated on the surface of the support.

TiO_2: A titanium precursor $Ti(OC_3H_7)_4$ was precipitated onto the support surface. The defined titanisopropylate hydrolysed due to the presence of water causing hydroxide formation. The heat treatment at 673 K again induced the formation of TiO_2 nano particles.

2.3 Catalytic Testing

For the catalytic experiments, a fixed-bed reactor (ø = 6 or 12 mm) made of quartz, operated at ambient pressure and equipped with on-line gas chromatography was used. A reaction mixture consisting of 40 Vol.% C_3H_8, 20 Vol.% O_2 and 40 Vol.% N_2 was passed through undiluted catalyst (0.2–1 g; d = 250–355 µm) packed between two layers of quartz of the same particle size. Total flow rates from 10 to 150 cm^3/min were used depending on the type of catalyst partial pressures of propane and oxygen, which were varied from 30 to 60 and 15 to 50 kPa, respectively.

3 Physical and Chemical Characterization

3.1 Catalysts Based on the µm-TiO_2-Support

Spray-dried TiO_2 after calcination shows a specific surface of 4 m^2/g. After covering with the active compounds the BET analysis showed an increase of the specific surface of hierarchical catalysts compared with the pure support in the range 9 to 12 m^2/g. For catalysts with TiO_2 as the active compound the specific surface is higher than for catalysts with V_2O_5 or MoO_3.

Table 1: Specific surface and content of active compounds of the layer close to the surface for the µm-TiO_2-support

Support / Active compounds A/B	$x_{\text{Active compound}}$ [%]	S_{BET} [m²/g]	$S_{\text{Active compound}}$ [m^2/g]	Content of active compounds XPS [At %]		
			calculated	Ti	Mo	V
µm-TiO_2-support, spray-dried and calcined		4.0				
µm-TiO_2 / V_2O_5	1	9.2 ± 0.2	524	21.2	–	2.5
µm-TiO_2 / V_2O_5	5	9.0 ± 0.1	104	20.4	–	3
µm-TiO_2 / MoO_3	1	9.3 ± 0.2	534	20.3	2.4	–
µm-TiO_2 / MoO_3	5	9.8 ± 0.2	120	18	3.9	–
µm-TiO_2 / TiO_2	1	12.0 ± 0.2	804	–	–	–
µm-TiO_2 / TiO_2	5	12.3 ± 0.2	170	–	–	–
µm-TiO_2 / TiO_2/V_2O_5	1/1	9.3 ± 0.2	216	22.0	–	0.5
µm-TiO_2 / TiO_2/MoO_3	1/1	7.8 ± 0.4	156	18.6	0.5	–
µm-TiO_2 / MoO_3/V_2O_5	1/1	13.9 ± 0.2	400	22.3	0.9	0.5–

The surface area of the active component can be estimated from basic data applying a mixing rule

$$S_{\text{BET}} = S_{\text{Active compound}} \cdot x_{\text{Active compound}} + S_{\text{Support}} \cdot x_{\text{Support}}$$

The values are in the range of more than 100 m^2/g . Even for the high uncertainties of these values one may conclude a particulate morphology of the active compound and rather than of a covering mono-layer. These results were confirmed by the XPS data. The SEM/EDX micrographs (Figure 3) show a relatively homogeneous distribution of the V- and the Ti-signals. However, the resolution of the EDX was much too rough for the detection of nano-particles.

Thus, TEM-investigations were needed.

The assumption that the active compound is rather a particulate form and not a monolayer covering continuously the support surface, is confirmed by TEM photos. Since the concentrations mentioned above cannot be proved with EDX/TEM, catalysts are prepared with 10 wt. % V_2O_5 to get the photos shown (Figure 4).

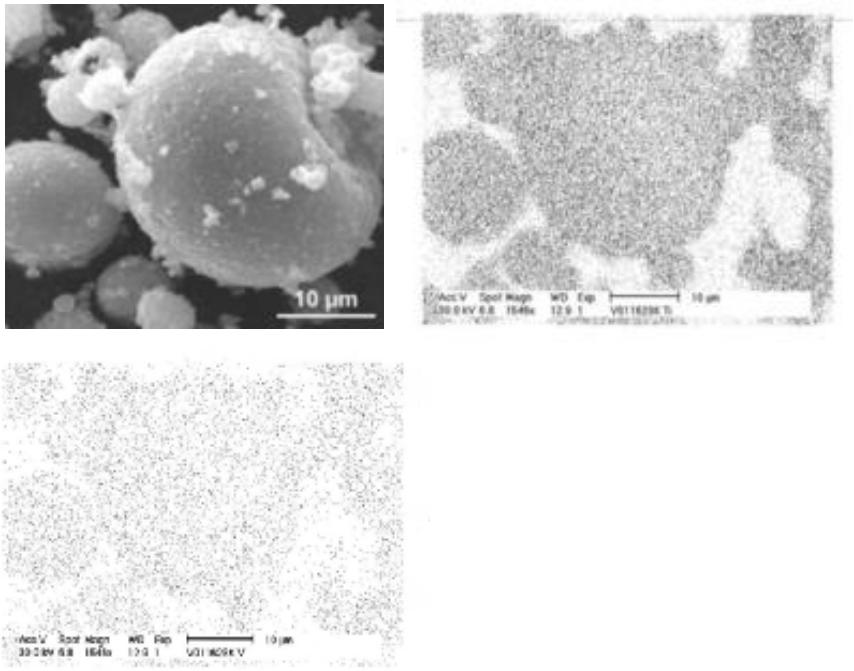

Figure 3: SEM-image and EDX-element distribution (Ti in the middle, V on the right side) of a µm-TiO_2-support with V_2O_5

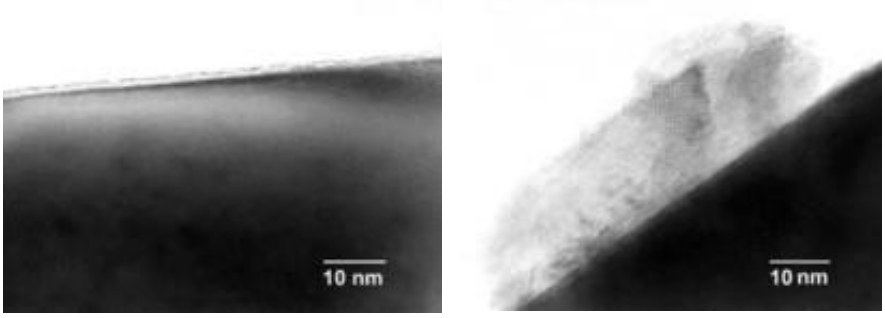

Figure 4: TEM-images of the µm-TiO_2-support (left side) and a V_2O_5- particle on the µm-TiO_2-support (right side)

The pure µm-TiO_2-support shows amorphous layers on the surface. Insulated vanadium oxide particles of up to 100 nm are located on the µm-TiO_2-support.

3.2 Catalysts Based on the nm-TiO_2-Support

The prepared nm-TiO_2-support has a specific surface of 140 m^2/g which reduced to 119 m^2/g after a heat treatment (673 K, 2 h). Being covered by active compounds the specific surfaces decrease even up to 58 m^2/g.

The size of the specific surface of the catalysts depends decisively on the sequence of the respective active compounds. Catalysts with TiO_2 as the first active compound (intermediate layer) have higher specific surfaces than catalysts with MoO_3 or V_2O_5 as the first active compound. This influence of the sequence of applying the active compounds is less pronounced in case of the nm-TiO_2 catalysts with the active compounds V_2O_5/MoO_3 and MoO_3/V_2O_5.

EDX results show a good analogy between the theoretical and the measured amounts of molybdenum. The MoO_3 is located on the surface of the nm-TiO_2-support (Figure 5).

Table 2: Specific surface and content of active compounds of the layer close to the surface for the nm-TiO_2-support

Support / Active compounds A/B	$x_{Active\text{-}compound}$ [%]	S_{BET} [m²/g]	Content of active compounds XPS [At %]		
			Ti	Mo	V
nm-TiO_2-support		140.0			
nm-TiO_2-support, calcined		119.0			
nm-TiO_2 - TiO_2/V_2O_5	2.5/2.5	65.5 ± 0.3	21.0	–	1.5
nm-TiO_2 - V_2O_5/TiO_2	2.5/2.5	58.9 ± 0.2	17.7	–	1.1
nm-TiO_2 - TiO_2/MoO_3	2.5/2.5	104.8 ± 0.6	12.7	8.4	–
nm-TiO_2 - MoO_3/TiO_2	2.5/2.5	89.1 ± 1.2	14.5	6.3	–
nm-TiO_2 - V_2O_5/MoO_3	2.5/2.5	66.7 ± 0.4	19.4	2.3	2.2
nm-TiO_2 - MoO_3/V_2O_5	2.5/2.5	71.8 ± 0.4	17.6	3.4	2.1

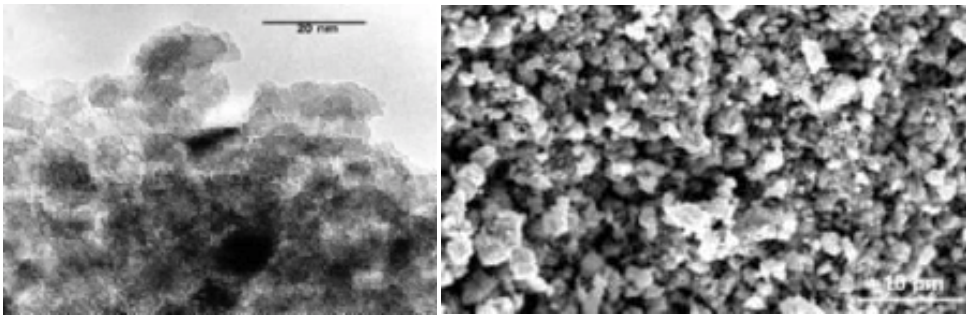

Figure 5: TEM-image: MoO_3 on a nm-TiO_2-support (left side), SEM-image: V_2O_5 and MoO_3 on a nm-TiO_2-support (right side)

4 Catalytic Results

4.1 Catalysts Based on the µm-TiO_2-Support

The different activities of the examined catalysts depend highly on the respective active compound. Using a support with a constant amount of active compound (V_2O_5, MoO_3 or TiO_2) resulted in a decrease of the propane conversion V_2O_5 » MoO_3 ≈ TiO_2. With a larger amount of all active compounds a higher propane conversion but a lower selectivity of propene was denoted. The yields of propene for catalysts with the same amount of 1wt % each of the two active compounds increase from 1.7 % to 7.3 % in the sequence:

µm-TiO2-TiO2/MoO3 < µm-TiO2-MoO3/V2O5 < µm-TiO2-TiO2/V2O5 (Figure 6).

The catalytic effect of the hierarchical construction is more favorable than that of individual components. So the contact zone between the nano-particles of the active compound and the respective TiO_2 support is probably of special importance. The number of these contacts increases with smaller particle sizes (more contacts per square) and increasing amounts of active compounds as long as the latter ones are located as isolated nano-particles on the support.

The yield of materials with a nano-scaled interlayer was almost twice of that without, both for a given V_2O_5-content.

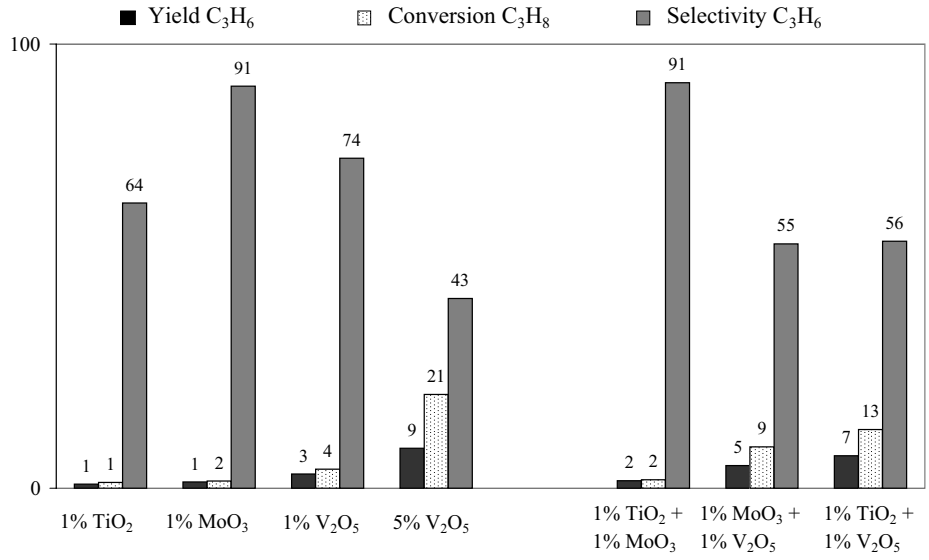

Figure 6: Catalytic results for the µm-TiO_2-support with one or two active compounds (Feed $C_3H_8/O_2/N_2$ = 40/20/40; T = 773 K; contact time τ = 0,75 [g s ml^{-1}])

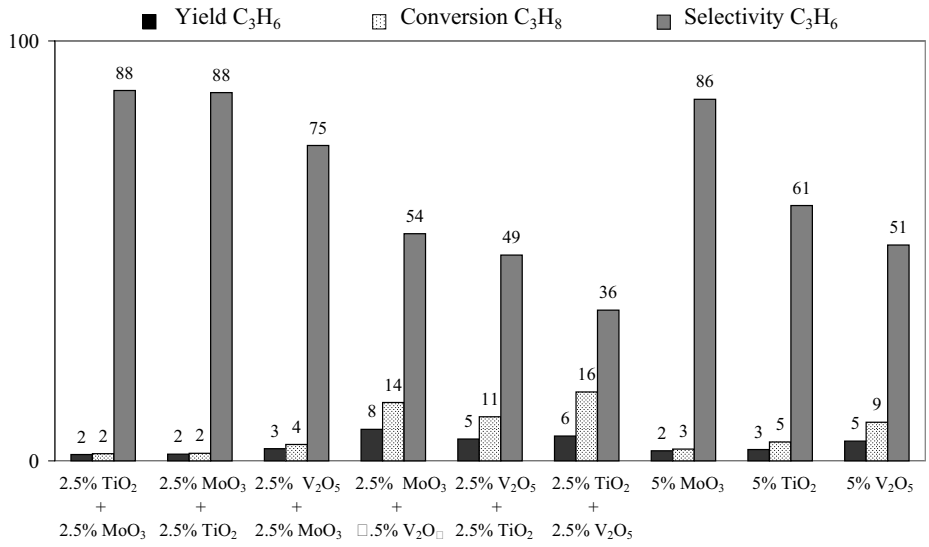

Figure 7: Catalytic results for the nm-TiO_2-support with one or two active compounds (Feed $C_3H_8/O_2/N_2 = 40/20/40$; T = 773 K; contact time $\tau = 0{,}75$[g s ml^{-1}])

4.2 Catalysts Based on the nm-TiO_2-Support

The nm-catalysts behave especially selectively in ODP for nm-TiO_2-TiO_2/MoO_3 and nm-TiO_2-MoO_3/TiO_2 combinations (Figure 7). These results agree with item [3] according to which the selectivity reaches approx. 80 % when a MoO_x species is used as an active compound.

The selectivity of the material with a nano-scaled interlayer was higher even for a low V_2O_5 concentration (S[nm-TiO_2-TiO_2-1 wt.%V_2O_5] « S [nm-TiO_2-5 wt.%V_2O_5]).

5 Conclusion

The hierarchically structured morphology of the catalyst enables a nano-scaled contact between the active compound and the interlayer. Thus, the influence of the support is of lesser importance. The chemistry of the active compound and the interlayer, however, play a very important role. The combination TiO_2-support with V_2O_5 in the appropriate morphology was responsible for the catalytic behavior. The same amount of V_2O_5 in another environment did not give as good results. The mechanisms for this behavior are not yet understood.

6 Acknowledgements

This work was subsidised by the Deutsche Forschungsgemeinschaft DFG under grant Schu 679/21-2, Fe 608/1-2 and Ca 147/9-2.

7 References

[1] C. Doornkamp, V. Ponec, J. Mol. Catal. A: Chemical 2000, 162 19–32
[2] K. Chen, A.T. Bell, E. Iglesia, J. Catal. 2002, 209, 35
[3] M.D. Argyle, K. Chen, A.T. Bell, E. Iglesia, J. Catal. 2002, 208, 139
[4] P. Rybarczyk, H. Berndt, J. Radnik, M.-M. Pohl, O. Buyevskaya, M. Baerns, A. Brückner, J. Catal., 2001, 202, 45–58
[5] J.B. Stelzer, H. Kosslick, J. Caro, D. Habel, E. Feike, H. Schubert; Chemie Ingenieur Technik 2003, 7, 872–877
[6] J.B. Stelzer, D. Habel, M.-M. Pohl, H. Kosslick, E. Feike, J. Caro, H. Schubert, Chemie Ingenieur Technik 2003, 11, 1656–1660

Formation of Nanostructural Oxide Fibers

T. M. Ulyanova, N. P. Krut'ko, P. A. Vityaz
Institute of General and Inorganic Chemistry NAS of Belarus

1 Introduction

In different areas of science and technology studies are being made of objects with the size factor: nanocrystals, nanoclusters; nanostructural, nanophase, nanoporous materials and nanocomposites. A spectrum of the mentioned objects in continuously extended: from information recording structures, converters of different-type energy to new medical preparations and their carriers. Developing nanostructural technologies and materials provides the basis for electronics, computer-aided techniques and in other fields of industry. Many investigations [1–4] are devoted to studying nanostructural materials and their properties. One of the most feasible methods of synthesis is the use of the biomimicking when a prototype of a structure or architecture of substance is represented by the microstructure of a natural or synthetic organic object [5].

The aim of the present work was to explore the process of forming nanostructural fibers of alumina, zirconia, magnesia, titania and to study how their crystalline and porous structure depends on the conditions of synthesis and heat treatment.

One of the variants of producing oxide nanostructural fibers is a method based on the ability of natural and synthetic polymers to swell in solutions and to absorb inorganic compounds or to form complexes. Hydrated cellulose fibers, felt, clothes served as an initial polymer, they were impregnated with aqueous solutions of metal salts and then dried. Hydrated cellulose was cho-

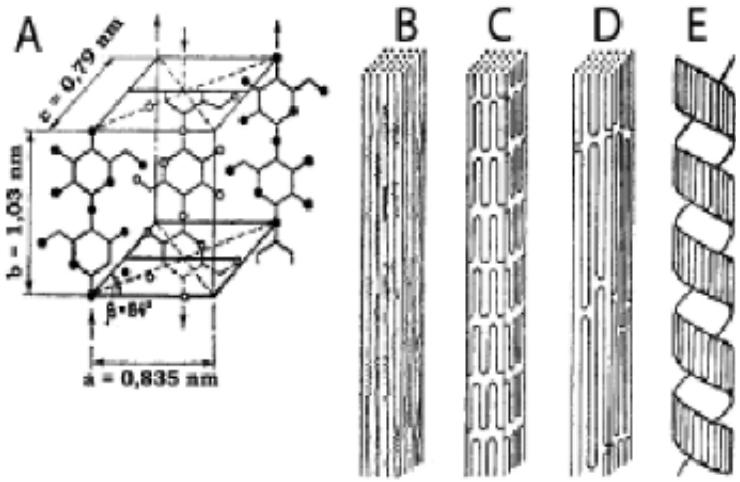

Figure 1: The spatial model of an elementary cellulose cell (a) and the structural model of elementary fibrils (b-e): b – extended chain with alternating amorphous and crystalline regions; c – folded chains; d – conformation of interconnected chains; e – ribbon-shaped twisted folded chains

sen because it is polysaccharide of complex architecture: its macromolecule is comprised of $(3–36) \cdot 10^3$ elementary links formed from anhydro-D-glucose. Elementary links are β-glycoside bonded into chain-like molecules and incorporate three free hydroxyl groups of the second, third and sixth carbon atoms. Each final elementary link has 4 such groups [6].

Chain-like polysaccharide molecules form micelles that in their turn - fibrils and lamellas. As for a number of other natural polymers, the cellulose microstructure is a system of crystallite-microfibrils surrounded by polycrystalline and amorphous regions. The cellulose structure as a whole is a complex system that in addition to microfibrils contains the very fine network of microscopic capillaries, micro- and macropores (Figure 1). All this forms a large inner surface in a fiber that is the governing factor in the processes of filling capillaries, pores and of sorbing aqueous and organic media with polymer molecules. As a result, hydrated cellulose undergoes swelling. The above-mentioned structure and properties of a polymer permit solutions of different metal salts to be added and inorganic fiber materials to be prepared upon heat treatment.

2 Experimental

Hydrated cellulose filaments, an unwoven material (felt) or clothes were carefully cleaned and impregnated with solutions of aluminium, magnesium, titanium chlorides or with zirconium oxychloride. Fibers were dried and heat-treated in a special regime in the air over the temperature range 600-1600 °C [7]. Upon impregnation and drying of salt-containing hydrated cellulose fibers, their structure was examined, changes in geometrical size and mass of material samples were determined.

Thermal conversions of salt-containing fibers when heated were studied by the differential thermal analysis on a Paulic-Paulic-Erdei thermograph. Samples were heated in the air with a temperature rate of 5 °/min, a mass was 0.5 g. Highly cleaned Al_2O_3 served as a standard comparison substance. The fiber structure was analyzed using X-ray methods, IR spectroscopy and scanning electronic microscopy. A specific surface and absorptive ability of fibrous oxides were estimated through benzene vapors and nitrogen absorption by BET method (Brunauer-Emmett-Teller), a mean size of aluminium oxide particles was calculated by the formula:

$$S = f \ / \ L \cdot r \tag{1}$$

where S is the specific surface, L is the mean particle size (diameter if it is a sphere), ρ is the solid substance density, f is the coefficient, whose value varies from 6 for a spherical or a cubic shape to 2 if particles are small thin plates [8]. The data obtained by this formula can be adopted as estimations for comparison.

A radius pore volume distribution was calculated from the desorption curves by the Kelvin equation:

$$r_k = 2\sigma \cdot V_m / RT \cdot \ln(p / p_o), \tag{2}$$

where r_k is the pore radius, σ is the surface tension and V_m is the molar volume of liquid condensed adsorbate, p_o and p are the experimental values of the saturation pressure of adsorbate vapors , and of the equilibrium one of adsorbate vapors when the adsorbate content in a reactive vessel with a test sample is varied [8].

The X-ray diffraction analysis was made on a diffractometer DRON-3 with a Ni-filter, CuK_α radiation with a wavelength λ = 1.5405 Å was used. To calculate a crystallite size the following reflexes were recorded: γ–Al_2O_3 - [440], θ-Al_2O_3 - [202], α-Al_2O_3 - [012], MgO - [220], TiO_2 - rutile [110], anatase [101], ZrO_2 of monoclinic modification - [111], of tetragonal - [111] and spinel $MgAl_2O_4$ - [440]. As standards use was made of the samples of fibrous zirconia, magnesia, titania and spinel annealed at 1500 °C with a high orderliness of a crystalline lattice. In X-ray studies of alumina the α-phase was determined through aluminium hydroxide gel thermally treated at 1400 °C and of the γ- and θ-phases – through aluminium hydroxide gel annealed at 900 °C and 1100 °C, respectively.

Reflex broadening due to a size factor is related to a mean crystalline size by the Sherer formula:

$$L = R \cdot (0{,}94 \cdot \lambda / \beta \cdot \cos\theta), \tag{3}$$

where L is the crystallite size, λ is the radiation wavelength, β is the physical reflex broadening, θ is the half of an angle reflected from the crystalline plane of a ray, R is the distance from a sample to a detector of a reflected ray [9]. Taking into account that oxide fibers are produced in a freely poured state with no pressure, their microstresses are practically absent. Hence, the physical reflex broadening is caused mainly by the size of crystallites.

3 Result and Discussion

The process of swelling and sorption by hydrated cellulose fibers of salt solutions involved several stages. During sorption solutions rose via capillary channels into an interfibrillar space and first penetrated into the amorphous and then into the crystalline component of a polysaccharide macromolecule. In this case, impregnating liquid was kept by cellulose both due to capillary, adsorption forces and due to chemical bond energy.

As hydrated cellulose is a stereoregular high-orientated polymer, anisotropy inherent in swelling manifested itself in changes of swollen fiber diameter (4–6 %) and in its length (11–17 %). In estimating polymer swelling the architecture of an initial hydrated cellulose fiber was not unimportant. In impregnating viscous fibers comprised of 60-70 monofibers, an increase in fiber mass was 50–70 %, the mass of impregnated clothes increased by 110–125 %, upon impregnation of an unwoven material with a random location of short monofibers and a branched network of capillary channels its mass increased by 150–200 %. During heat treatment of salt-containing hydrated cellulose fibers there proceeded complex physical-chemical processes, followed by considerable mass losses. Material heating up to 100 °C occurred with adsorbed water removal, in the temperature range 180–200 °C crystallization water of metal salts split off and polymer thermolysis started. Releasing hydrogen chloride speeded up the splitting of glycoside bonds of cellulose macromolecules. Above 250 °C metal salts dissociated and hydrated cellulose fibers oxidized. As a result, highly volatile substances disappeared, cellulose fibers were turned to carbon fibers containing high-dispersed particles of metal hydroxides or metal oxides. In the temperature range 350–550 °C carbon in the air burnt out, nanosized oxide grains at contacting places sintered to form nanostructural inorganic fibers. It should be noted that the macrostructure of oxide fibers was always identical to the structure of an initial polymer material irrespective of a type of absorbed metal salts (biomimicking) but the tempera-

ture boundaries of forming oxide fibers depended on the nature of added compounds. As an example consider the process of forming aluminium oxide fibers.

According to the thermal analysis results, on heating of cellulose fibers impregnated with aluminium chloride three endoeffects were observed due to loss of adsorbed and chemically bound water in a polymer and in aluminium chloride crystal hydrate (Figure 2).

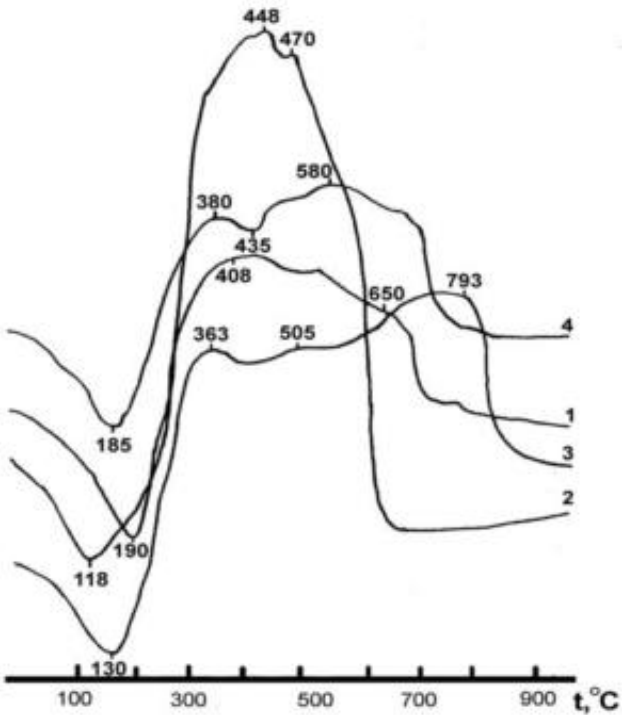

Figure 2: DTA curves of hydrated cellulose fibers impregnated with the solutions of chlorides: aluminium (1), zirconium with yttrium (2), titanium (3), aluminium with magnesium (ratio as in the case of spinel) vs. heat treatment temperature

The highest mass loss velocity was over the temperature range 200–360 °C. This is associated with organic matrix oxidation and carbon formation. This process in the DTA curve meant the first exoeffect superimposed with the endoeffect in the temperature range 330–360 °C. The latter is caused by heat absorption under thermal dissociation of aluminum chloride, because of which an intermediate product: hydroxide or aluminium hydroxochloride was formed. As the heating temperature increased from 400 to 600 °C, carbon burnt out, an intermediate product destructed, and fibrous alumina (second exoeffect) was formed. Oxide fibers with the preserved architecture of the initial polymer were produced from salt-containing hydrated cellulose materials.

Analysis of the crystalline structure of the formed alumina fibers showed that at heating up to 600–650 °C alumina was amorphous, i.e. a crystallite size is compared with a radiation wave-

length. Upon heat treatment, at 700 °C it crystallized in the γ-phase. As the heating temperature of fibers increased up to 900 °C, the latter was transformed into the Al_2O_3 θ-modification. In this case, the fibers possessed a developed specific surface, high reactivity and were comprised of nanosized aluminium oxide grains. During annealing of fibrous aluminium oxide in the range 1100–1200 °C its crystalline structure was turned to α-corundum and was kept up to 1600 °C. To calculate a size of oxide grains in fibers, use was made of the X-ray method for determination of reflex contour broadening of synthesized material phases. Analysis of the results obtained showed that as the annealing temperature of powders increased, particle sizes of alumina, titania and zirconia in different crystalline phases varied nonmontonically. So, e.g., at the beginning of alumina γ-phase at 700 °C the reflexes were broadened, the particle size was 5–6 nm. As the temperature grew up to 800–850 °C, the particle size increased by a factor of 3–4. Alumina γ-phase crystallites grew. This pointed to the structure ordering. In the field of the crystallographic transition $\gamma \rightarrow \theta$ (900 °C) substance underwent dispersing, the crystallite size again decreased up to 6–7 nm, then their value smoothly increased up to the next structural conversion to the α-phase. The crystallites of the latter increased with growing annealing temperature 1100–1500 °C from 40-50 to 300–350 nm (Fig. 3A). Zirconia crystallites of tetragonal and monoclinic modifications had the same behavior. A smooth growth of particle sizes with elevating heat treatment temperature broke down in the region of structural changes, followed by destructing initial phase crystallites and by decreasing their size (Fig. 3B). For comparison the size of Mg Al_2O_4 crystallites was calculated. The spinel formation was supported by the X-ray phase

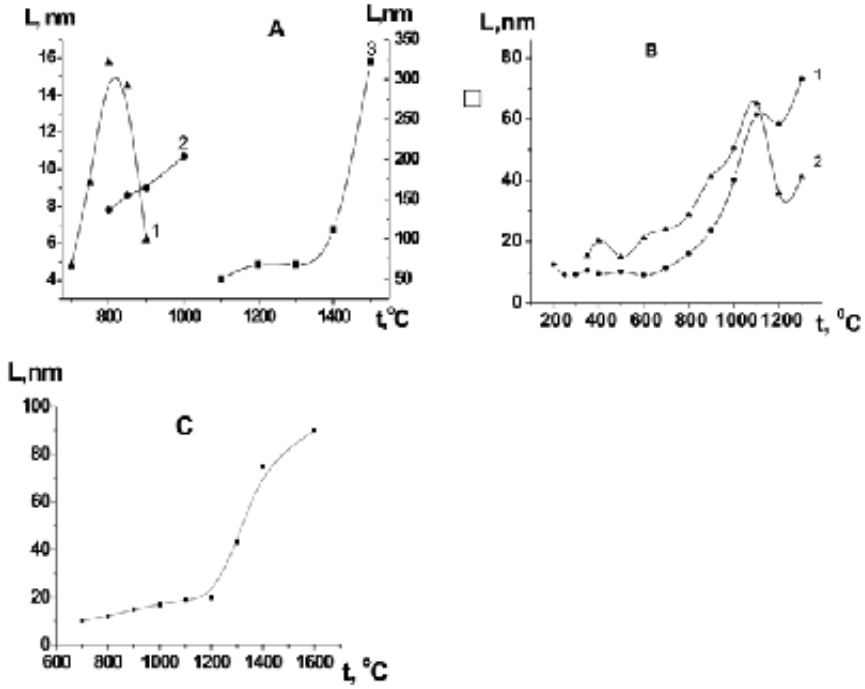

Figure 3: Variations of crystallite sizes of alumina (A) γ-phase - 1, θ-phase - 2, α-phase - 3; zirconia (B) monoclinic phase - 1, tetragonal - 2; (C) spinel $MgAL_2O_4$ vs. annealing temperature

analysis after a salt-containing polymer had been heated up to 500 °C. Down to 1250 °C spinel reflex contours [400] were broadened, and at 1300 °C substance started crystallizing. Calculation of crystallite sizes showed that their value increased from 10 to 20 nm over the temperature range 600–1200 °C and to 90 nm at 1600 °C (Fig. 3C). As the spinel did not undergo crystalline structure changes, no dispersing of crystallites and breaks in the curve for the crystalline size vs. temperature were seen.

The X-ray data are supported by the electronic microscopic analysis. Grains in oxide fibers are well seen on the microphotographs of material samples upon their 1100–1500 °C heat treatment (Fig. 4).

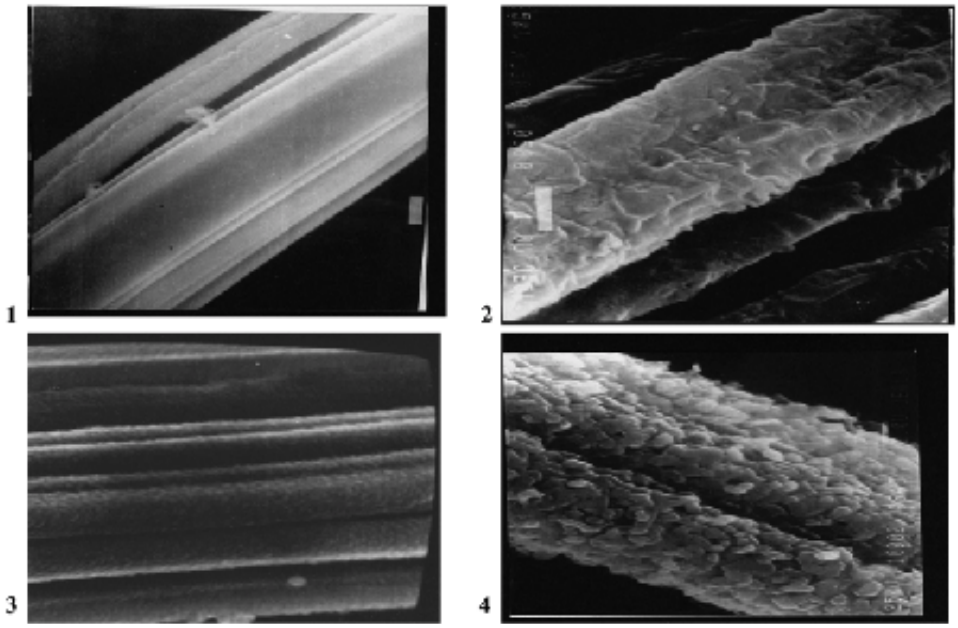

Figure 4: The microstructure of zirconia fibers annealed at temperatures: 700 °C - 1, 1000 °C - 2, 1200 °C - 3, 1500 °C - 4

Oxide fibers are complex in architecture, have a high porosity and a specific surface. This is attributed to the presence of nano-sized particles and a branched network of microchannels and nanopores. To evaluate the porosity nature, a limiting sorption volume and a value of a specific surface of fibrous alumina materials, attempts were made to study benzene vapor adsorption by oxide fiber samples in vacuum at a residual pressure of $1 \cdot 10^{-5}$ mm Hg. The experimental results have demonstrated that fibrous alumina are characterized by the mesoporosity (pore size is 2–5 nm). This is supported by the available hysteresis loops on the isotherms for adsorption-desorption of benzene vapors (Fig. 5). In addition, there is a small percent (up to 10 %) of micropores which are filled with adsorbate in the low-pressure range (initial sections of the adsorption isthoserms). The shape of the isotherms for benzene vapor adsorption permits us to state that slit-like mesopores are present in Al_2O_3 fibers. The radius pore volume distribution

has shown that upon heat treatment of fibrous aluminium oxides over the temperature range 700–800 °C, in addition to slit-like pores bottle-shaped ones with a neck diameter of about 4 nm are formed in monofibers. This is sustained by S-shaped curve 2 in Fig. 5. As a whole, when the heat treatment temperature of materials increased above 1100 °C, the hysteresis loops of the adsorption-desorption isotherms were narrowed down, the values of a sorption volume and a specific surface decreased. In this case, the micro- and mesopores in fibers were closed and macropores (more than 100 nm in size) were formed. The materials sintered and reinforced.

As the heating temperature of fibers increased from 700 to 1600 °C, the picnometric density of fibrous alumina varied from 0.6 to 1.4 g/cm^3, the total porosity of a material decreased from 90 to 45 %, the mean monofiber diameter was equal to 2-4 μm, the size of pores constituted 0.5–2.0 nm and that of mesopores was 2.0–10.0 nm, the specific surface decreased from 150 to 15 m^2/g. An alumina filament consisting of 60 monofibers and annealed at 900 °C withstood a load of 24 g.

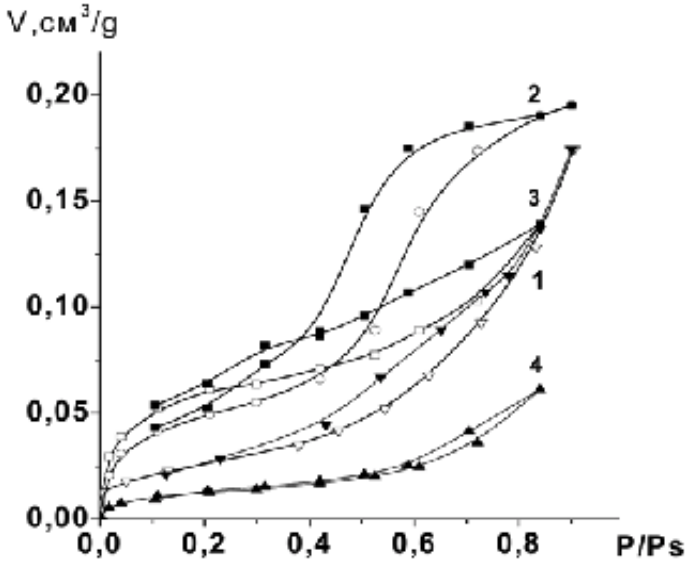

Figure 5: The adsorption-desorption isotherms of benzene vapors formed by nanosized fibrous alumina annealed at temperatures: 650 ºC - 1, 750 ºC - 2, 900 ºC - 3 and 1100 ºC - 4

Thus, by varying a heat treatment regime it is possible to arrange goal-directed control of the physical-chemical properties of nanostructural fibrous materials.

4 Conclusion

The study performed permitted us to establish the mechanism for formation of fibrous oxide with a complex architecture, including metal oxide nanoparticles, nanopores and microcapillaries.

Based on the calculations of crystallite sizes, it is found that crystallographic transformations of fiber oxides cause substance to disperse. Structural changes in fibrous oxides are followed by varying the porosity nature and pore size. The obtained regularities permit us to predict the properties and to control the technology of producing nanostructural fibrous oxide materials.

5 References

[1] Nanotechnology Research Directions. (Ed.: M. C. Roco, R. S. Williams, P. Alivisatos), Kluver Academic Publishers, 2000, p. 292
[2] A. L. Buchachenko, Advanced Chemistry (Rus.). 2003, 72, N 5, 419–437
[3] A. L. Ivanovsky, Advanced Chemistry. (Rus.). 2003, 71, N 3, 203–224
[4] I. Brooks, P. Bunzel, H. Ehrhardt et al., Thermodynamik von Grenzflächen. Veröffentlichungen eimer Institut für Nanotechnologie, FKGmbH, Karlsruhe, 2001, 109–113
[5] P. Greil, Advanced Materials. 2002, 14, N 10, 709–716
[6] Z. A. Rogovin, Chemistry of Cellulose, Chemistry, Moscow, 1972, p. 519
[7] I. N. Ermolenko, T. M. Ulyanova, P. A. Vityaz, I. L. Fyodorova, Fibrous High-Temperature Ceramic Materialsl, Nauka i Tekhnika, Minsk, 1991, p. 255
[8] S. J. Gregg, K. S. W. Sing, Adsorption, Surface Area and Porosity, Academic Press, London-New York, 1982, p. 310
[9] Ya. S. Umansky, X-raying of Metals and Semiconductors. Metallurgy, Moscow, 1969, p. 496

Silicon Carbonitride Nanopowders Synthesized by Laser Pyrolysis for Plastic Nanocomposites

R. Dez, J.L. Besson[1], D. Porterat, M. Amara[1], J. Vicens[2], N. Herlin-Boime
Laboratoire Francis Perrin, Service des Photons, Atomes et Molécules, CEA-CNRS URA 2453, CEA Saclay, 91191 Gif sur Yvette Cedex, France
[1] Laboratoire des Sciences des Procédés Céramiques et Traitements de Surface, UMR 6638, ENSCI, 47 av. Albert Thomas, 87065 Limoges Cedex, France
[2] SIFCOM (Ex LERMAT), CNRS UMR 6176, ENSICAEN, 6 Bd Maréchal Juin, 14 050 Caen Cedex, France

1 Abstract

In material science, the ability to create nano-particles with accurately controlled characteristics is very important for nano-structured materials fabrication. This paper deals with the specific case of Si_3N_4/SiC structural ceramics, for which it is highly important to obtain materials exhibiting plastic deformation at high temperature. Such materials could be suitable to design ceramic pieces with complex geometry as those produced from powder metallurgy.

In silicon nitride based ceramics, the small size and the equiaxed shape of the grains constituting the material are two important parameters in favour of high temperature deformation. Therefore, SiCN nanosized powders are real candidates as starting materials to elaborate dense Si_3N_4/SiC nanocomposites exhibiting the microstructure required for ductility at high temperature.

SiCN nanopowders with different chemical compositions and characteristics (degree of crystallisation, thermal stability…) have already been prepared by CO_2 laser pyrolysis of gaseous or liquid precursors. The drawbacks were the high cost and danger of gaseous precursors (silane) and/or the low thermal stability of powders obtained from liquid precursors, which made sintering very difficult.

In this study, we demonstrate that SiCN nanopowders with a good thermal stability can be prepared from the aerosol laser pyrolysis method and can be used to elaborate nanocomposites by hot forming. Thus, the effects of various synthesis parameters, such as the chemical nature of the precursor and laser power, on the degree of crystallisation and on the thermal stability of nanopowders are investigated. Powders characteristics such as chemical composition, morphology, structure and thermal stability are reported. A correlation between the powders synthesis conditions and their thermal stability is established. Synthesis parameters leading to an improvement in thermal stability are determined. Preliminary results about high temperature deformation properties of dense nanocomposites elaborated from these powders are reported.

2 Introduction

Materials for structural application at high temperature need an improved fracture toughness, thermal shock resistance, oxidation resistance and a good creep behaviour… In the last years, special attention has been paid to superplastic deformation of Si_3N_4/SiC nanocomposite materials. [1] Indeed, plastic deformation at high temperature of such hard materials would be useful

to fabricate ceramic parts with accurate dimensions, as it is usually the case for metals. To achieve such a property, it is necessary to elaborate the materials from SiCN nanopowders with the following characteristics : nanometric size, round shape and narrow size distribution.

Powders obtained from the CO_2 laser pyrolysis method exhibit such properties. SiCN nanopowders could be obtained with controlled chemical composition and size from a mixture of gaseous precursors (silane, acetylene, monomethylamine). The creep behaviour of Si_3N_4/SiC nanocomposites elaborated from these SiCN nanopowders was found promising for high temperature deformation [2, 3]. The main drawbacks for the use of such powders were the high cost and the experimental dangerous aspect of the process due to the presence of silane precursor. To decrease at the same time time cost and danger, SiCN powders were synthesized from a liquid precursor (hexamethyldisilazane, HMDS). These powders exhibit a high weight loss during heat treatment at high temperature [4, 5] which makes them very delicate to use for materials fabrication. In a recent work, we demonstrated that it was possible to obtain nanopowders with good thermal properties by adding a minor phase of silane to HMDS [6]. In the present paper, we report some complementary results on the characterisation of these powders, the elaboration of Si_3N_4/SiC nanocomposite materials from these powders. The first results about the creep behaviour of these nanocomposite materials are also presented.

3 Experimental

This section briefly presents the most salient features related to the synthesis method and to the procedure used for the elaboration of the dense materials from the nanopowders.

3.1 Synthesis and Characterization of the Powders

The powders were obtained from the laser synthesis method which has already been described in several publications [see for example ref. 4]. An aerosol of HMDS was generated in a glass jar (aerosol generator : Pyrosol model from RBI, Meylan, France) and carried to the reaction zone by argon gas. The gaseous silane was mixed with the HMDS aerosol droplets before reaching the reaction zone. In the present case the laser power was 720 W. Concerning the silicon precursors, the chemical composition of the reactive phase was 80 % HMDS and 20 % silane. The nitrogen content was adjusted by adding a NH_3 flow. Rather large quantity of powders (≅ 100 g.) was prepared in order to carry out detailed material study.

Chemical analysis of the powders were obtained from CNRS, Laboratoire Central d'Analyse, (Vernaison, France). The powders were characterized by infrared spectroscopy, X-Ray diffraction and Transmission Electron Microscopy (TEM) at low and high resolution. A Jeol 2010 microscope equipped with EDS and a Topcon 02B for HRTEM were used.

3.2 Elaboration of the Materials and Compression Tests

To elaborate the materials, the SiCN nanopowders were mixed in ethanol with commercial sintering aids (6 wt% yttria and 3 wt% alumina) and de-agglomerated by milling with Si_3N_4 balls according to the procedure described in [7, 8]. Y_2O_3 was a micronic powder purchased from

Prolabo (S_{BET} = 3.5 m^2/g) while Al_2O_3 was a nanometric powder obtained from Marketech (S_{BET} = 48.4 m^2/g). The mixture was then dried under air in an oven (12 hours, 90°C). The green body obtained from this powdery mixture exhibit about 30 % of the theoretical density and was sintered by hot-pressing under 35 MPa in a nitrogen atmosphere using the temperature ramp given by Doucey [3, 9]shown in Figure 3. The microstructure of the sintered materials was observed by TEM. The creep behaviour was studied under compression in air on parallelepipedic samples (7 × 3 × 3 mm^3).

4 Results and Discussion

It was previously shown that the thermal stability of powders was related to their physical (degree of crystallization...) and chemical characteristics (carbon content in excess...). Therefore, according to this thermal stability criteria [10], one powder sample was selected to elaborate the Si_3N_4/SiC material and only the results related to this sample are presented here.

4.1 Powder Characterization

Table 1 presents the chemical composition of the SiCN nanopowder used in this study and its decomposition in terms of stoichiometric compounds. This analysis shows that the powder contains, as it was planned a low amount of excess carbon compared to the stoichiometric compounds.

Table 1: Chemical analysis and decomposition in stoichiometric compounds of the SiCN nanopowder (wt%)

Si	C	N	O	H	Si_3N_4	SiC	SiO_2	C
56,1	5.9	30.1	7.3	0.6	75.8	6.3	13.8	4.1

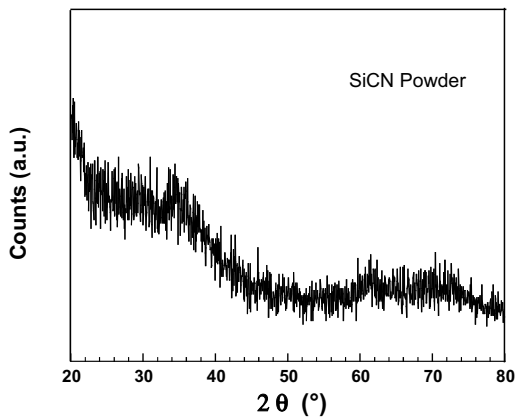

Figure1: X-Ray diffraction diagram of SiCN nanopowder

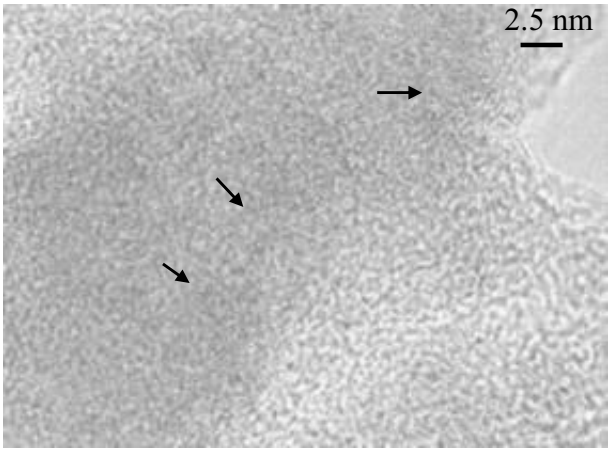

Figure 2: High Resolution picture of nanopowder, some nanodomains have been arrowed on the micrograph

XRD data (Figure 1) show no well defined diffraction peaks resulting. However, some large structure at the position of crystallized Si_3N_4 (e.g. near 35°) were interpreted as traces of Si_3N_4 crystallization [6]. This interpretation is confirmed by the HRTEM picture shown in Figure 2. This picture clearly shows the presence of crystallized Si_3N_4 nano domains with a typical diameter of 2–3 nm.

4.2 Densification and Characterization of Si_3N_4/SiC Composites

Figure 3 presents together the temperature ramp (left scale) used during the sintering process and the densification behaviour (right scale) as a function of time. Densification begins at 1550 °C and increases during the dwell step at 1600 °C. At the end of the sintering treatment, a fully dense sample was obtained.

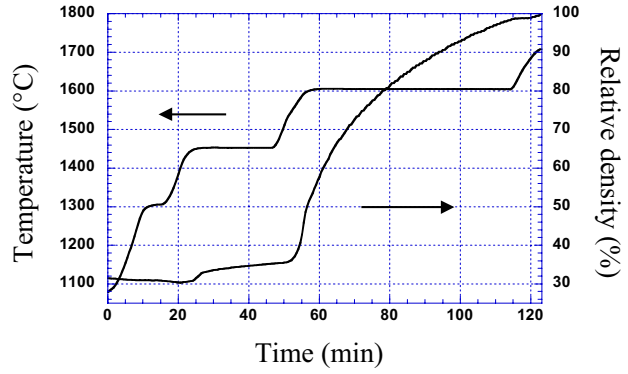

Figure 3: Densification behaviour of the SiCN + Al_2O_3 + Y_2O_3 sample

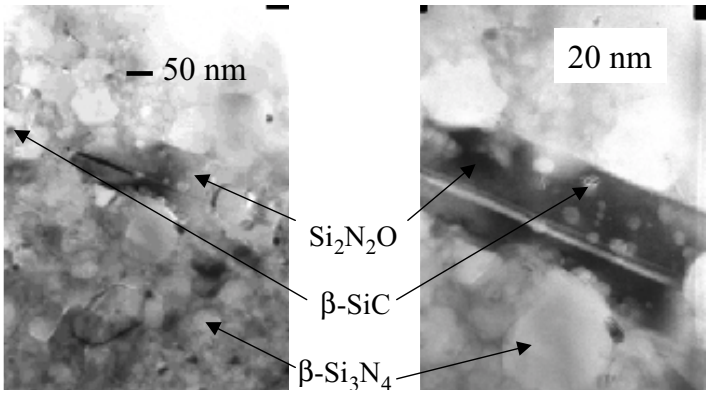

Figure 4: TEM micrographs of the sinteres samples

After the sintering treatment, one of the main question is the stuctural organisation of the composite. The presence of a minor Si_2N_2O phase, identified by XRD [Amamra2003], has been correlated with the drying step before the sintering step. A complete analysis of this phenomenon is presented in [10, 11] Figure 4 shows the microstructure obtained after the sintering. It consists in equiaxed β-Si_3N_4 grains ($d \cong 60$ nm) embedded in an intergranular glassy phase. SiC precipitates, with sizes less than 20 nm, are located inside the Si_3N_4 and Si_2N_2O, grains. Larger ones ($d \cong 100$ nnm) are in intergranular positions. However, the most salient feature is that the microstructure remains in the nanometric range and is mainly composed of equiaxed grains (mean grain size 60 nm). Such characteristics are mandatory to achieve the deformation property of the composite.

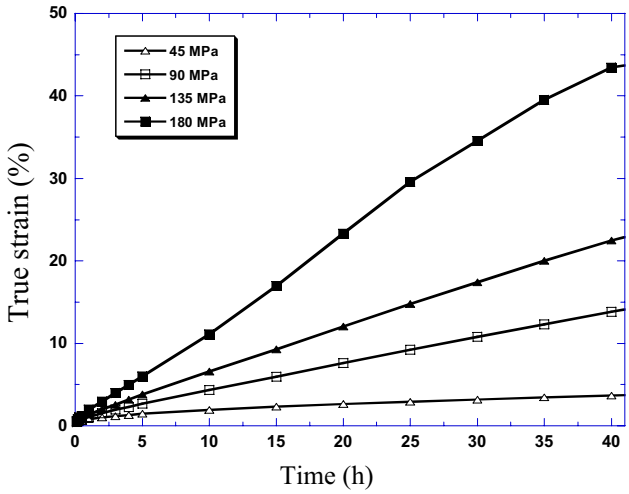

Figure 5: Creep curves at 1350 °C under different stresses

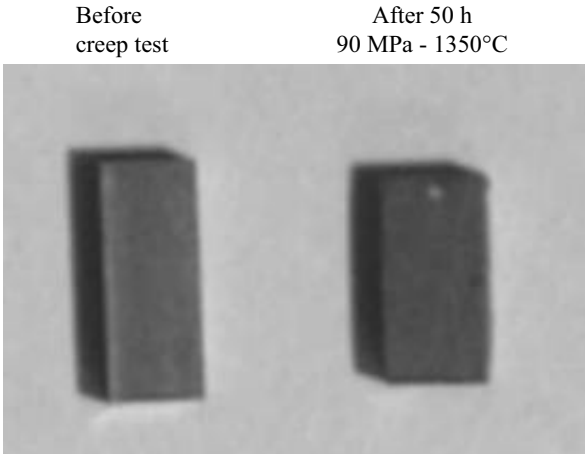

Figure 6: Optical pictures of a nanocomposite sample before and after compression creep test

4.3 Creep Behaviour

The creep behaviour was assessed under compressive loading in air at 1350 °C. Figure 5 presents the isothermal creep curves for stresses ranging from 45 to 180 MPa.

The creep curves show a short primary stage followed by a long pseudo-stationary stage characterized by a slowly decreasing creep rate. This kind of behavior is usual in silicon nitride based ceramics. However the nanosize of the microstructure allows deformation as high as 40 % without cracks forming or barrelling as shown in Figure 6

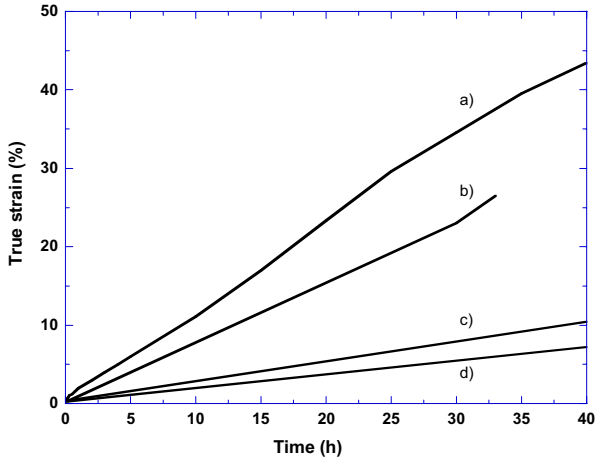

Figure 7: Comparison of the creep curves under 180 MPa at 1350 °C for various composites (a) : present sample (b) Si_3N_4-SiC nano-nano composite (from doucey 99) (c) Si_3N_4 monolith (from Ros 95) (d) Si_3N_4-SiCN Micro-nano composite (from Mayne 97)

Figure 7 presents the creep curves obtained under the same conditions (180 MPa, 1350 °C) for the present nanocomposite, a nanocomposite and a micro-nano composite processed with nanopowders synthesised from gaseous precursors (SiH_4 + CH_3NH_3 + NH_3) and a monolith Si_3N_4 material used as a reference [12]. All these samples were processed with the same amount of additives (6 wt% Y_2O_3 + 3 wt% Al_2O_3) and must therefore contain similar amount of glassy phase. The main structural difference is the grain size decreasing from sample (d) to (a), resulting in an increasing ductility.

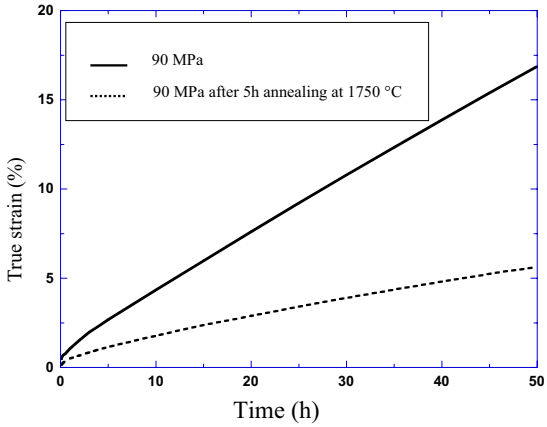

Figure 8: Creep curves at 1350 °C under 90 MPa before and after annealing treatment at 1750 °C for 5 h

An annealing treatment for 5h at 1750°C converts the as-sintered equiaxed structure into an acicular one due to the anisotropic growth of the β-Si_3N_4 grains. This change results in an improvement of the creep resistance, as shown in Figure 8 where the strain is divided by three after the annealing treatment. This results is encouraging because ceramic devices should not any more be deformed when they are used as structural parts.

5 Conclusion

This paper has shown that it is possible to use nanopowders to obtain Si_3N_4/SiC nanoceramic materials. Related to their fine microstructure, these materials exhibit a high ductility and appear well suited to hot forming of near-net shape parts, which can be converted in acicular microstructure with improved creep resistance as required in operation. As pointed by several authors, the next step will be to synthesize nanopowders where the sintering aids are added during the synthesis and to investigate the properties of these powders One interesting point would be to study the ability for sintering of such nanopowders because the mixing step which makes the sintering step time consuming would be suppressed.

6 Acknowledgements

The authors wish to thank P. Goursat and S. Foucaud-Raynaud for fruiful discussions.

7 References

[1] F. Wakai, Y. Kodama, S. Sakaguchi, N. Murayama, K. Izaki, K. Niihara, Lett. to Nature, 1990, 344, 421–3
[2] J.L. Besson, B. Doucey, S. Lucas, D. Bahloul-Hourlier, P. Goursat, J. Eur. Ceram. Soc., 2001, 21, 959–968
[3] B. Doucey, B., PhD Thesis, University of Limoges, 1999
[4] M. Cauchetier, O. Croix, N. Herlin, M. Luce, J. Am. Ceram. Soc,1994, 4, 993–998
[5] E. Musset, E., PhD Thesis, University of Paris XI Orsay, 1995
[6] R. Dez, F. Ténégal, C. Reynaud, M. Mayne, X. Armand, N. Herlin-Boime, J. Eur. Ceram. Soc. 2002, 22, 2969–79
[7] M.Mayne, D. Bahloul-Hourlier, P. Goursat, J.L. Besson, C.R. Acad. Sci. B, 320, 1995, 433–39
[8] M. Mayne PhD thesis, University of Limoges, 1997
[9] Doucey, B, D. Bajhloul-Hourlier, P. Goursat, B. Devilliers, J.L. Besson, R. Dez, N. Herlin-Boime, Ceramika, Ceramics, Polish ceramic Bulletin,2002, 29, 23–28
[10] R. Dez, PhD thesis, University of Limoges, 2003
[11] M. Amara, R. Dez, S. Foucaud-Raynaud, D. Bahloul-Hourlier, P. Goursat, N. Herlin-Boime, J.L. Besson, proceedings ISNTIT3, 2003 to be published in Silicates Industriels
[12] F. Rossignol, PhD thesis, University of Limoges, 1995

Synthesis of Ormosil Particles by Non-Hydrolytic Sol-Gel Chemistry

John N Hay[1], Miguel Manzano[1] and Steve Shaw[2]
1. Chemistry Division, SBMS, University of Surrey. Guildford, Surrey, GU2 7XH, UK.
2. Future Systems Technology Division, QinetiQ, Farnborough, Hampshire, GU14 0LX, UK.

1 Abstract

The non-hydrolytic sol-gel process has been used for the synthesis of organically-modified silicas (ormosils). The effect on morphology of the ormosil particles has been investigated using different solvents, types of stirring, and additives such as surfactants or polystyrene. The products are organic-inorganic hybrid (nano)composite materials where the organic modifications (methyl, ethyl, hexyl or phenyl groups) are covalently attached to silicon.

2 Introduction

The sol-gel process is a synthetic method that offers access to a wide range of materials with very different physical and chemical properties. The sol-gel process involves the generation of colloidal suspensions (*sols*) of solid particles in a liquid. During the process, these colloids are converted to viscous *gels* (gelation) and then to solid materials [1].

The non-hydrolytic sol-gel (NHSG) route is based on the direct polycondensation between a metal halide and an oxygen donor (such an alkoxide, ether or alcohol) under non-aqueous conditions[2]. The products of the reaction are an inorganic oxide and an alkyl halide.

The accepted mechanism of the NHSG process (Figure 1) proceeds *via* the coordination of the oxygen donor to the metal centre of the metal halide. The halide is then able to attack (nucleophilic substitution) the α-carbon in the alkoxide group and cleavage of the carbon-oxygen bond leads to an oxide linkage [2–5].

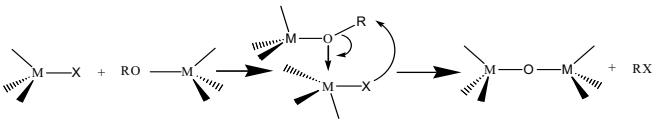

Figure 1: Mechanism of the non-hydrolytic sol-gel condensation [2–5]

When silicon is the metal centre (less reactive than other metals), this reaction works only with tertiary, benzylic and allylic carbon groups, which are able to stabilise a carbocation [6,7]. If primary or secondary carbon groups are used, a Lewis acid such as iron(III) chloride is necessary to catalyse the condensation.

The synthesis of organic-inorganic hybrid materials has received much attention in recent years because of the possibility of developing materials with unique structures and properties.

There has been an increase in the number of publications dedicated to this topic, including some interesting reviews [8–15], indicating the growing interest of chemists, physicists and materials researchers in this new area.

Combining inorganic components with organic moieties on a microscopic or nanoscopic scale needs a formation process of the inorganic network which is compatible with the thermal stability of the organic components. Organic materials can rarely survive temperatures higher than 200 °C, but classical inorganic methods commonly work around 1000 °C. The sol-gel process overcomes this limitation and permits low temperature routes to organic-inorganic hybrids[1].

The synthesis of organic-inorganic hybrids *via* the conventional sol-gel process (hydrolytic route) has been intensively explored over the last 20 years or so [3,8,9,12,13,16–22]. However, relatively little research has been carried out in the field of hybrids *via* the non-hydrolytic sol-gel route, and the different kinetic and electronic factors during the process offer an alternative route to some hybrids whose synthesis using the hydrolytic route may have problems such as incompatibility of the precursors with water [23].

Those hybrids with organic groups attached to silicon are often abbreviated as Ormosils (ORganically MOdified SILicas or silicates). They are defined as silicate networks (inorganic component of the hybrid) that are organically modified by the covalent attachment of small organic groups to some or all the silicon atoms in the network [23]. The non-hydrolytic route to produce ormosils has been researched in the last few years mainly by two groups in Surrey (UK) [24, 25] and Montpellier (France) [26, 27] independently.

In this paper, the synthesis of ormosils *via* the non-hydrolytic sol-gel process is described. Different conditions of the process have been investigated in an attempt to produce micron or sub-micron particles of uniform shape. The general reaction of the process consists of the direct polycondensation of tetraalkoxysilane (oxygen donor) with different trichlorosilanes (Eq. 1).

$$\begin{aligned} &RSiCl_3 + 0.75Si(OEt)_4 \rightarrow \left[RSi_{1.75}O_3\right]_n + 3EtCl \\ &(R=CH_3, C_2H_5, C_6H_{13}, C_6H_5) \end{aligned} \tag{1}$$

3 Experimental

3.1 Procedure

The method used to synthesise the ormosil materials was the non-hydrolytic sol-gel route to oxides previously reported [6, 28, 29] but using organically modified precursors (alkyl chlorosilanes) that are commercially available.

In the past, the synthesis of these ormosils was carried out in an uncontrolled way [24, 25]. In the present work, the production of controlled morphology particles has been targeted under „pseudo dispersion polymerisation“ conditions. This investigation involves the search for the optimal conditions for the reaction trying different solvent mixtures, stirring methods and speed, and effects of different additives (surfactants and polystyrene).

In a typical experiment, methyl-modified silica ($CH_3Si_{1.75}O_3$) was formed by reacting methyltrichlorosilane [MTCS] (3.89 g, 26 mmol) with tetraethyl orthosilicate [TEOS] (4.00 g, 19 mmol) in the presence of iron(III) chloride catalyst (0.08 g, 1 wt. % based on weight of reac-

tants), using a mixture of toluene (4.5 ml) and petroleum ether (100–120 °C) (13.5 ml) as the solvent. The reaction was carried out under nitrogen flow. A mechanical stirrer was used during the reaction. The mixture was stirred at room temperature for 2 hours, and then the temperature was increased to reflux temperature (110 °C). The reaction was kept under these conditions for 20 hours. The resulting solid was filtered and washed with diethyl ether. The obtained solid was dried in a vacuum oven at 60 °C for 8 hours to yield a dark powder (2.89 g, 99 %). The characterisation methods used are described elsewhere [25].

Elemental analysis gave C, 12.1; H, 3.29 % (calculated: C, 10.7, H, 2.67 %). The FT-IR spectrum showed C-H stretching vibrations at 2970–2950 cm^{-1}, a Si-CH_3 deformation band at 1275 cm^{-1} and asymmetric Si-O-Si stretching vibrations at 1010 cm^{-1}.

4 Results and Discussion

The synthesis of a range of organically-modified silicas has been carried out using the non-hydrolytic sol-gel route. The reaction is based on the direct polycondensation of TEOS with different alkyltrichlorosilanes (methyl-, ethyl-, hexyl- and phenyltrichlorosilane) using iron(III) chloride as catalyst (Eq. 1).

During the synthesis of the ormosils, satisfactory yields were obtained in most cases (yields were calculated based on the theoretical empirical formula of the product), and the elemental analysis figures were obtained in reasonable agreement with the theoretical values. In some cases, the yield was over 100 %. It was assumed that this could be due to two main reasons: there was still solvent present in some of the products, as can be seen in the IR spectrum of a typical ormosil product (Figure 2 left); also some of the reactions did not go to completion, as is shown in the ^{29}Si NMR spectrum (Figure 2 right).

A typical ^{29}Si DP MAS NMR spectrum of an ormosil showed a mixture of T (mono-substituted silica) and Q (unmodified silica) species, as expected (Figure 2 right). In the spectrum the most intense peaks were T^3 (–64 ppm) and Q^4 (–109 ppm) species, which means that the predominant silicon species in the sample were $RSi(OSi)_3$ and $Si(OSi)_4$ (when doing direct polarisation the relative intensities are quantitative). However, Q^3 species (–103 ppm) were also observed, which means that there were some oligomers such as $(EtO)Si(OSi)_3$ within the product, confirming that the polycondensation did not proceed to completion. The absence of T^0 and Q^0 species indicated that there was no unreacted monomer within the product.

In the past, the non-hydrolytic sol-gel process has been used for the synthesis of ormosils in the absence of solvents[24,25]. However, the use of a solvent potentially offers some control over the product morphology. The solvent was carefully selected so that the precursors were soluble at the start of the reaction, with the ormosil precipitating out as the reaction progresses. Due to the totally opposed polarities of the organic content (alkyl or aryl substituents) and the silica network, it was thought that the process may behave like a dispersion polymerisation, with the organic groups projecting into the non-polar solvent, and the inorganic polar silica forming the core of the resulting particles. Spherical particles were expected to be formed as a result of the steric stabilisation of these particles.

Different solvents were tested during the first part of the work, including various mixtures of toluene and petroleum ether (100–120 °C). The relative proportions of the two solvents were found to influence the degree of aggregation of the smallest particles; as the solvent is richer in petroleum ether, the aggregation diminishes. The best balance of catalyst solubility and reduced

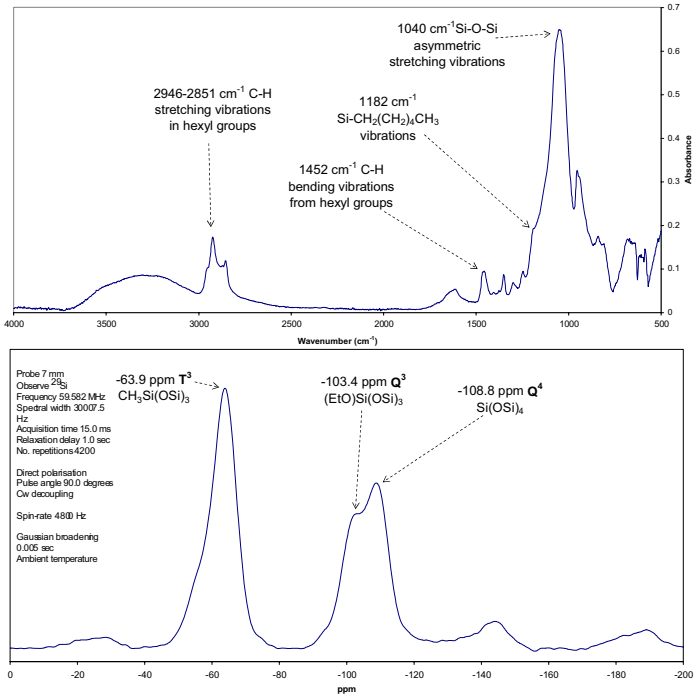

Figure 2: Left: IR spectrum of hexyl-modified silica synthesised using a mixture of solvents (toluene:petroleum ether 25:75 %) and Brij® 52 (5 wt. % based on weight of reactants) as additive. Right: ^{29}Si NMR spectrum of methyl-modified silica synthesised using a mixture of solvents (toluene:petroleum ether 25:75 %) and high speed stirrer.

aggregation was found with a 25:75 % mixture of toluene and petroleum ether respectively. In many cases, large aggregated, irregular particles of diameter > 100 µm were obtained, but in some cases these could be clearly seen to consist of much smaller (a few µm) individual particles.

The non-hydrolytic sol-gel synthesis of these ormosils goes through a „pseudo-dispersion" polymerisation process, therefore the final properties of the hybrids strongly depend on the degree of phase dispersion. Thus, by increasing the speed of stirring during the process, the size and distribution of the primary particles is expected to change. Using an ULTRA TURRAX® T 25 high speed, high shear stirrer, beneficial effects on reducing particle size and aggregation were found. The smallest (irregular) particles were found to have diameters of approx. 1 µm.

The use of surfactants (surface active agents) was thought to be one possible way to control the structure of the hybrids during their formation. The surfactants reduce the interfacial energy between the hybrid particles, stabilising the dispersion formed. Thus, surfactants were expected to control the aggregation of the smallest particles, and hence some structural properties of the ormosils.

Five different surfactants within a homologous series of non-ionic polyoxyethylene ethers with different polarities (HLB values, Table 1) were selected:

Table 1: Surfactant data from Sigma-Aldrich

Commercial name	Name	Structure	HLB	Molecular weight
Brij® 52	Polyoxyethylene 2-cetyl ether	$C_{16}H_{33}(OCH_2CH_2)_nOH$ n~2	5.3	330 g.mol^{-1}
Brij® 30	Polyoxyethylene 4-lauryl ether	$C_{12}H_{25}(OCH_2CH_2)_nOH$ n~4	9.7	362 g.mol^{-1}
Brij® 98	Polyoxyethylene 20-oleyl ether	$C_{18}H_{35}(OCH_2CH_2)_nOH$ n~20	15.3	1,150 g.mol^{-1}
Brij® 92	Polyoxyethylene 2-oleyl ether	$C_{18}H_{35}(OCH_2CH_2)_nOH$ n~2	4.9	357 g.mol^{-1}
Igepal® co-210	Polyoxyethylene 2-nonylphenyl ether	4-$(C_9H_{19})C_6H_4(OCH_2CH_2)_nOH$ n~2	4.6	308 g.mol^{-1}

Brij® 52 appeared to be the most effective surfactant in producing more regular shaped primary particles of *ca*. 1 μm diameter, while the other surfactants were effective in reducing the overall level of aggregation. One of the concerns was that during the work up process, when filtering the product, the small particles could pass through the filter, losing them. The experiments with Brij® 52 as additive were repeated with a change in the typical procedure: the gel obtained was left to dwell in a desiccator with P_2O_5 for 2 days at room temperature. Spherical particles (Figure 3) were obtained when synthesising methyl-modified silicates. The size distribution of these spherical particles was quite broad, from *ca*. 100–200 nm to 1–2 μm in diameter. The aggregation degree of these spherical particles was not improved using this new method, as can be seen in SEM pictures (Figure 3).

The size of the organic moiety was found to be an important factor in the structure of the hybrid, because under certain conditions (using Brij® 52 as surfactant) spherical particles were obtained using methyl substituents, while under the same conditions, the ethyl-modified silicate particles were found with irregular shapes.

Viscosity has been investigated as a possible parameter to control the size and morphology of metal particles [30] (it permits the control of the aggregation step of the growth mechanism);

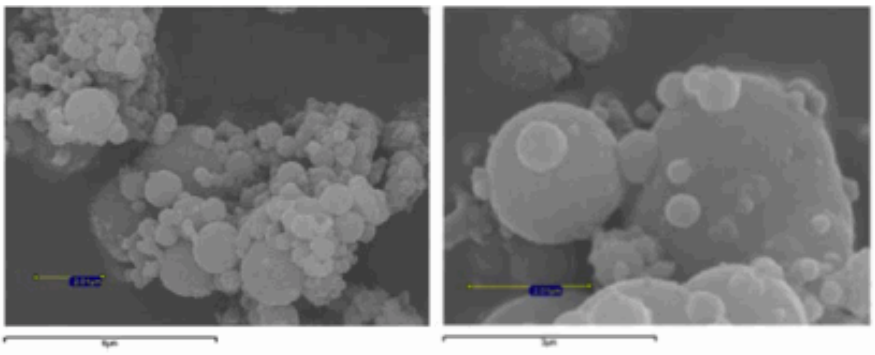

Figure 3: Scanning electron micrographs of methyl-modified silica synthesised using 25:75 % toluene:petroleum ether as the solvent and Brij® 52 as the surfactant without filtering the resulting gel

a possible way to increase the viscosity of the reacting medium is the use of polystyrene as an additive. Polystyrene present in a colloidal suspension may control the group-wise behaviour of the colloidal particles.

Different amounts of different polystyrenes (different molecular weight) were tested. The morphology of the obtained products was not very different from previous results. Irregular, aggregated hybrid particles were obtained with a size ranging from 0.5 μm to 5 μm. However, when increasing the viscosity significantly using 20 % (percentage based on weight of the solvent used) of polystyrene (M_n *ca.* 45,000), spherical shapes were found in some of the primary particles (Figure 4).

The long polymer chains of polystyrene could interfere in the normal nucleation and growth stage of the ormosil and thus modulate the shape of the particles during their formation process.

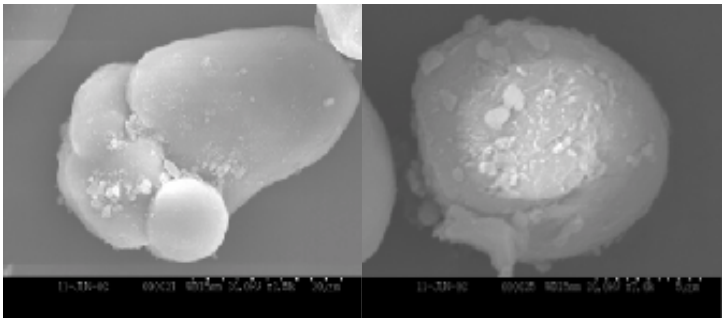

Figure 4: Scanning electron micrographs of methyl-modified silica using 20 % (based on weight of solvent) of polystyrene (Mn. *ca.* 45,000) during the non-hydrolytic sol-gel synthesis

5 Conclusions

A variety of sol-gel synthetic routes have been studied in an effort to produce organic-inorganic hybrid (nano)particles. The use of a non-hydrolytic sol-gel route successfully produces hybrid ormosils, whose morphology can be varied depending on the nature of the solvent (a mixture of toluene and petroleum ether (100–120 °C) (25:75 %) was found to be the most effective in reducing the aggregation of the smallest particles); the type of stirring (a decrease in the particle size was achieved when using a high speed stirrer); the presence, type and concentration of surfactant (Brij® 52 was found to be the most effective, achieving spherical particles in the size range of 100 nm–1μm, Figure 3); and the presence and concentration of polystyrene as additive during the synthesis (20 % of polystyrene [M_n *ca.* 45,000] based on the amount of solvent was found to be partially successful producing spherical particles with relative low aggregation, Figure 4).

Four different organic groups (methyl, ethyl, hexyl and phenyl) were introduced into the hybrid to evaluate how the organic content affects the morphology of the resulting ormosil. The size of the organic moiety was found to be an important factor in the structure of the hybrid.

For the first time, some control over the product morphology during the NHSG synthesis of ormosils has been achieved. In the past, ormosils have been synthesised in a NHSG solvent-free route, but no control over the morphology of the particles was achieved [48,49]. In the present work, the use of solvents in which the precursors are soluble, lead to ormosil spherical particles,

where the inorganic content (silica) of the hybrid formed the core of the particles and the organic groups projected into the non-polar solvent surrounding the inorganic oxide.

6 References

[1] C. J. Brinker and G. W. Scherer, The Physics and Chemistry of Sol-Gel Processing, Academic Press Inc., San Diego, 1990
[2] A. Vioux and D. Leclercq, Heterogen. Chem. Rev., 1996, 3, 65
[3] R. J. P. Corriu and D. Leclercq, Angew. Chem., Int. Ed. Engl., 1996, 35, 1420
[4] A. Vioux, Chem. Mater., 1997, 9, 2292
[5] L. Bourget, R. J. P. Corriu, D. Leclercq, P. H. Mutin and A. Vioux, J. Non-Cryst. Solids, 1998, 242, 81
[6] R. J. P. Corriu, D. Leclercq, P. Lefévre, P. H. Mutin, A. Vioux, J. Non-Cryst. Solids, 1992, 146, 301
[7] R. J. P. Corriu, D. Leclercq, P. H. Mutin, H. Samson, A. Vioux, J. Organomet. Chem., 1994, 466, 43
[8] J. Wen and L. Wilkes, Chem. Mater., 1996, 8, 1667
[9] C. Sanchez and F. Ribot, New J. Chem., 1994, 18, 1007
[10] L. Mascia, TRIPS, 1995, 3(2), 61
[11] J. E. Mark, Polym. Eng. Sci., 1996, 36, 2905
[12] B. M. Novak, Adv. Mater., 1993, 5, 422
[13] P. Judeinstein and C. Sanchez, J. Mater. Chem., 1996, 6, 511
[14] J. D. Mackenzie and E. P. Bescher, J. Sol-Gel Sci. Tech., 1998, 13, 371
[15] K. G. Sharp, Adv. Mater., 1998, 10, 1243
[16] D. Avnir, Acc. Chem. Res., 1995, 28, 328
[17] G. L. Wilkes, H. H. Huang and R. H. Glaser, in Silicon-Based Polymer Science, A Comprehensive Resource, edited by J. H. Ziegler and F. W. G. Fearon, American Chemical Society, Washington DC, 1990, p. 207
[18] J. E. Mark, in Hybrid Organic-Inorganic Composites, edited by J. E. Mark, C. Y-C. Lee and P. A. Bianconi, American Chemical Society, Washington DC, 1995, 585, p. 1
[19] J. D. Mackenzie, in Hybrid Organic-Inorganic Composites, edited by J. E. Mark, C. Y-C. Lee and P. A. Bianconi, American Chemical Society, Washington DC, 1995, 585, p.226
[20] D. A. Loy and K. J. Shea, Chem. Rev., 1995, 95, 1431
[21] R. J. P. Corriu, Polyhedron, 1998, 17, 925
[22] G. Schottner, Chem. Mater., 2001, 13, 3422
[23] J. N. Hay and H. Raval, Chem. Mater., 2001, 13, 3396
[24] J. N. Hay, D. Porter and H. Raval, Chem. Commun., 1999, 81
[25] J. N. Hay, D. Porter and H. Raval, J. Mater. Chem., 2000, 10, 1811
[26] L. Bourget, R. J. P. Corriu, D. Leclercq, P. H. Mutin and A. Vioux, in Proceedings of the First European Workshop on Organic-Inorganic Materials, edited by C Sanchez and F Ribot; Bierville, France, 1993, p. 305
[27] L. Bourget, D. Leclercq and A. Vioux, J. Sol-Gel Sci. Tech., 1999, 14, 137
[28] J. N. Hay and H. Raval, J. Sol-Gel Sci. Technol., 1998, 13, 109
[29] J. N. Hay and H. Raval, J. Mater. Chem., 1998, 8, 1233
[30] V. Pessey, R. Garriga, F. Weill, B. Chevalier, J. Etourneau and F. Cansell, J. Mater. Chem., 2002, 12, 958

Grain Boundary Microanalysis in Al_2O_3-SiC Nanocomposites

Ian P Shapiro, John M Titchmarsh, Steve G Roberts, Alex M Cock and Richard I Todd
University of Oxford, Oxford

1 Introduction

1.1 Al_2O_3/SiC „Nanocomposites“

Niihara and Nakahira [1] first investigated the use of fine (< 0.3 μm) particulate SiC reinforcement in polycrystalline alumina (Al_2O_3/SiC „nanocomposites“). They found that for nanocomposite bend strength was 1050 MPa (350 MPa for Al_2O_3) and toughness was 4.8 MPa.$m^{½}$ (3.5 MPa.$m^{1/2}$ for Al_2O_3) [1]. Attempts to replicate this work have resulted in less dramatic bend strength increases, typically in the range 500 to 800 MPa [2, 3, 4]. The current consensus is that little or no toughening occurs in nanocomposites [5].

Despite controversy over the existence and magnitude of strength and toughness increases, all researchers report a clear change in fracture mode. The addition of silicon carbide causes the nanocomposites to fracture transgranularly, rather than intergranularly, which is typical of alumina [1,6]. Another agreed effect of the nanocomposite additions is the change in wear behaviour. After polishing, the nanocomposites showed better surface quality than alumina polished under the same conditions [2, 4].

1.2 Strengthening Mechanisms

The strengthening mechanism in nanocomposites is unclear. It is known that residual stress arises on cooling from processing temperatures due to thermal expansion mismatch between the phases [7, 8]. The associated stress fields will influence crack propagation. However this would be expected to affect toughness, in contrast to observations. Another effect of the particulate addition is to limit grain growth. Smaller grains limit flaw size and increase strength, although not by a sufficient magnitude to explain the strength increases.

TEM observations show that ground and polished nanocomposite surfaces exhibit plastic deformation to greater depths than do alumina surfaces, and that dislocation glide is the predominant deformation mechanism, rather than via twinning as in alumina [9]. This results in greater compressive residual stress in the nanocomposite surface [10].

Niihara and Nakahira reported a dramatic increase in strength of nanocomposites after annealing at 1300 °C from ~ 1000 to ~ 1500 MPa [1]. Cracks are observed to heal in nanocomposites during annealing [10, 11], possibly by oxidation of SiC leading to the formation of mullite which bonds cracks. In addition, surface residual machining stress is found to persist after annealing nanocomposites but relaxes for alumina [12]. The combination of crack healing and the retention of surface residual stress can explain how annealing acts to increase the bend strength of nanocomposites.

The change in wear behaviour is linked to the change in fracture mode. In wear of alumina whole grains become detached from the sample when intergranular cracks propagate around a whole grain. In the nanocomposites, this occurs to a much reduced extent; instead, wear appears to be by plastic flow. This suggests that grain boundaries are strengthened in nanocomposites.

Jiao and Jenkins [13] observed the deflection of cracks into grains by intergranular SiC particles. While this may not provide a toughening mechanism, it is consistent with an improvement in wear properties. If intergranular cracks are deflected into grains less grain pull-out will occur. Thermal mismatch provides a possible mechanism for wear behaviour modification, by similar deflection of intergranular cracks by residual stress fields around particles [8]. The two mechanisms could be co-operational.

Al_2O_3/SiC and Al_2O_3/Al_2O_3 boundaries in nanocomposites have been found to have a silicon rich amorphous layer [14, 15]. Critically, neither Schmid et al.'s [14] nor Ferroni et al.'s [15] studies make comparisons with alumina. To attempt explain the change in properties between Al_2O_3 and Al_2O_3/SiC nanocomposites the changes in grain boundary structure and chemistry between the two must be compared. Hence, more detailed analysis of the differences in boundary structure and composition between alumina and nanocomposites is necessary to provide an explanation for the effect of SiC nanocomposite additions. This is the focus of the current work.

1.3 Processing

Unfortunately the SiC additions in Al_2O_3/SiC nanocomposites inhibit densification and increase the sintering temperature required [16]. Fully dense nanocomposites are usually produced by hot pressing [e.g. 1]. Industrial scale hot pressing is expensive and limits component shapes.

Processing temperatures can be lowered by addition of small concentrations of sintering aids. Kumar [17] investigated the use of Y_2O_3 and other oxides as sintering aids in nanocomposites and found: 0.5 % Y_2O_3 increased sintered density from 96 % to > 99 % at 1600 ºC. Temperatures below 1600 ºC become useful for industrial scale sintering. Materials with Y_2O_3 sintering aid additions are studied in this work. Analytical electron microscopy is used to investigate what effects the addition has on grain boundary structure and chemistry.

1.4 Grain Boundaries

Scanning transmission electron microscopy (STEM) using high spatial resolution energy dispersive X-ray microanalysis (EDX), allows composition of boundaries to be measured. If the segregant forms a complete atom layer this is known as „monolayer segregation". The average Al-Al atom spacing is used as the monolayer width in this work. If less than a complete layer is formed the segregation can be defined by what fraction of a monolayer it represents, which in this work is the ratio of density of segregant to Al atoms. The EDX spatial resolution is larger than a monolayer (~ 0.2 nm) so the resulting spectrum will include a contribution from the surrounding matrix area. The effect of this unwanted contribution will be to reduce the apparent concentration of any segregant in the recorded spectrum.

Quantification of STEM-EDX data requires careful analysis. The contribution from surrounding material can be removed by analysing a composition profile perpendicular to the boundary [18], or by calibrating the signal from analysing various areas of matrix [19]. In the

first method, used in this work, the X-ray interaction area and hence the compositional profile are considered as a convolution of the probe current distribution and the segregated monolayer [20].

2 Experimental

2.1 Materials Processing

All materials investigated (Table 2) were processed by conventional procedures used for pressureless sintering, described in detail elsewhere [21, 22]. Table 1: Manufacturers' data for starting powders shows the starting powders used. Al_2O_3, SiC, $Y(NO_3)_3$ (which forms Y_2O_3 on sintering), 4 wt% polyethylene glycol (PEG, a binder to help green body formation), and 0.1 g Dispex A40 (a dispersant, Ciba, Switzerland) were mixed. Attrition milling with zirconia media formed a well-dispersed homogeneous slip, which was then freeze dried to form a powder without hard agglomerates. All material was uniaxially pressed at 137 MPa, then heated in N_2 atmosphere at 3ºC/min and held at the sintering temperature for 120 minutes before cooling at the same rate.

Table 1: Manufacturers' data for starting powders

	„Easy sintering" alumina, AES11C	„Pure" alumina, AKP50	SiC, UF25
	Sumitomo, Japan	Sumitomo, Japan	H.C. Stark, Germany
Purity [wt%]	99.8	> 99.99	> 97.4
Impurities	SiO_2 0.06 wt% Na_2O 0.04 wt% MgO 0.05 wt% Fe_2O_3 0.01 wt%	Si = 25 ppm Fe = 20 ppm Na = 10 ppm Mg = 10 ppm Cu = 10 ppm	O < 2.50 wt% Al < 0.04 wt% Ca < 0.01 wt% Fe < 0.05 wt%
Particle size [µm]	0.5	0.2	0.45

Table 2: Materials Produced

Material	Al_2O_3 type	Sintering Temp ºC	Density % of theoretical *)	Grain size / µm
Al_2O_3 – 0.15 wt% Y_2O_3	Easy sintering	1550	100.1	1.70 #)
Al_2O_3 – 5 vol% SiC	Easy sintering	1600	94.8	0.89 #)
Al_2O_3 – 5 vol% SiC– 0.15 wt% Y_2O_3	Easy sintering	1600	97.8	1.27 #)
Al_2O_3	High Purity	1550	100.7	3.46

*) Compared to expected phases. #) From [21]

2.2 Specimen Preparation

Slices of material ~ 500 μm thick were cut using a diamond-grit abrasive annular saw; these were then ground and polished (down to 6 μm diamond) to parallel-sided slices of material ~ 100 μm thick. An ultrasonic drill, with water and silicon carbide grinding medium was used to produce 3 mm diameter disks. A dimple grinder (Gatan, USA) was used to polish (down to 1 μm diamond) dimples each side, leaving an area ~ 10 μm thick. The specimen was finally thinned to electron transparency using a Precision Ion Polishing System (Gatan, USA).

2.3 Microscopy

Microstructure was examined by conventional TEM (Philips CM20). EDX was performed using a cold field emission gun STEM (FEG-STEM, Vacuum Generators HB501, UK).

Grain boundary composition was analysed by taking a series of EDX spectra along a line perpendicular to the grain boundary extending 20 nm each side; these spectra were quantified by a commercial software package (INCA, Oxford Instruments, UK). The amount of each element was plotted as a function of distance from the boundary. The distribution was found to have an approximately Gaussian shape. The method and software developed by Vatter and Titchmarsh [18] was adapted for use here. The software used the composition data points and error bars to fit the most likely theoretical profile. This profile was then used to predict the density of atoms in a monolayer of grain boundary segregation.

Point analysis of grain boundaries was also used to give qualitative data such as the ratio between segregated elements. This ratio will be independent of how much matrix the probe analyses.

3 Results

3.1 General Microstructure

Grain size is reduced by the SiC addition (see Table 2: Materials Produced). „Easy sintering“ alumina with 0.15 % Y_2O_3 had grain size 1.70 μm but when 5 % SiC is also added grain size reduced to 1.27 μm [from 21].

Bright field TEM of the nanocomposite materials reveals inter and intragranular particles around 100 nm in size (Figure 1). These particles can be identified by STEM-EDX. Some particles are found to be rich in Si, others rich in Zr. Figure 2 shows „pure“ alumina processed by the same route but without any deliberate additions. Note the larger grain size of the SiC free material, despite a 50 ºC lower sintering temperature. The particles visible were found to be rich in Zr.

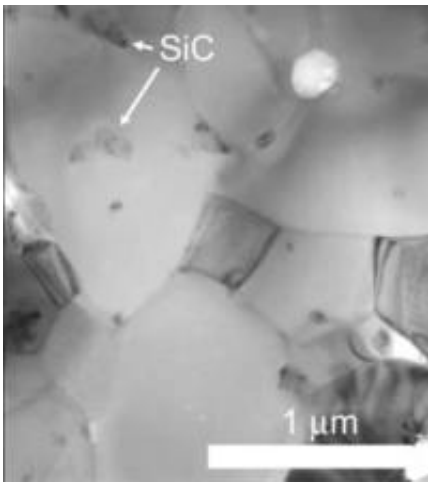

Figure 1: „Easy sintering“ Al_2O_3 with 5 % SiC and 0.15 % Y_2O_3 sintered at 1600 ºC

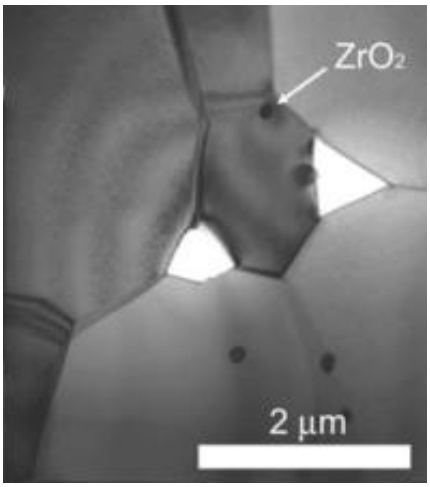

Figure 2: „Pure“ Al_2O_3 with 0 % SiC, 0 % Y_2O_3 sintered at 1600 ºC

3.2 Grain Boundary Chemistry

STEM-EDX of grain boundaries in all materials made with „easy sintering“ alumina revealed several elements (Figure 3b) which were not present in the matrix (Figure 3a). Both matrix and grain boundaries show Al, O, C and Ar peaks. (The peak 0.3 keV below Al is an artefact of the EDX system which has subsequently been eliminated.)

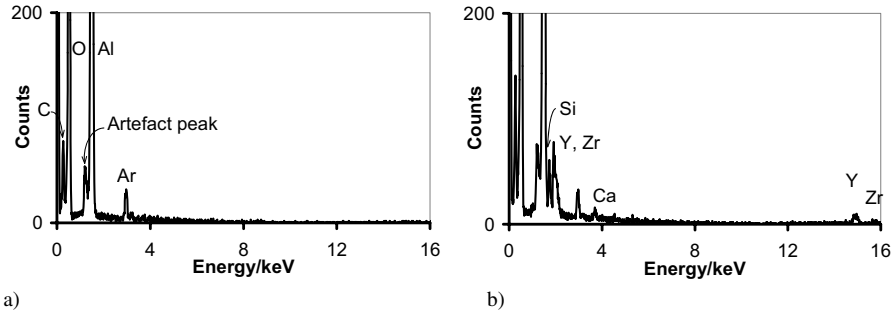

Figure 3: a. EDX spectrum of matrix in 'easy sintering' alumina with 5% SiC and 0.15% Y2O3 **b)** EDX spectrum of a grain boundary in „easy sintering“ alumina with 5 % SiC and 0.15 % Y2O3

A profile of a typical grain boundary (Figure 4) shows segregation of Y, Zr, Si and Ca. These four elements were found to segregate to grain boundaries in all the materials made from „easy sintering“ alumina. The „pure alumina“ sample was found to contain segregated Y and Zr. The average monolayer segregation calculated from the boundary profiles is shown in Table 3.

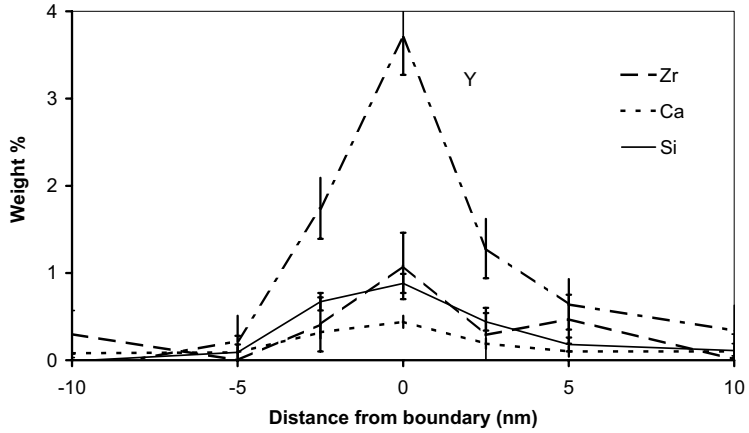

Figure 4: Segregation profile of a grain boundary in „easy sintering" alumina with 5 % SiC and 0.15 % Y_2O_3

Table 3: Average grain boundary segregation as a percentage of a monolayer.

Material	Number analysed	Al_2O_3 type	Si	Ca	Y	Zr
Al_2O_3 – 5 vol% SiC	6	Easy sintering	13	5	7	2
Al_2O_3 – 5 vol% SiC– 0.15 wt% Y_2O_3	5	Easy sintering	20	5	9	2
Al_2O_3 – 0.15 wt% Y_2O_3	5	Easy sintering	8	8	5	2
Al_2O_3	2	High Purity	0	0	2	11

Point analyses were also made on 8 or more boundaries in each material. The quantity of Ca was most consistent hence, the ratio of Y, Zr and Si to Ca was calculated from these data and compared between materials in Figure 5: Relative amounts of elements normalised to Ca by wt%a, b, c. There is considerable scatter in the data but a trend towards a greater ratio of Si to other elements in SiC-containing material is clear and also increased Y in Y_2O_3 containing material is suggested.

The pure alumina sample did not show Ca or Si segregation, but did show Y and Zr at grain boundaries. The ratio of Y to Zr segregated is shown in Figure 5: Relative amounts of elements normalised to Ca by wt%d for all materials investigated. A feature of the „pure" alumina samples was the occurrence of a phase containing Al, Y and Zr of around 500 nm in size which was commonly found adjoining a Zr rich region around 100 nm in size. This phase has yet to be identified.

4 Discussion

The microstructure of the materials was as expected. SiC additions decreased grain size and reduced density (Table 2). SiC particles were distributed in inter and intragranular locations.

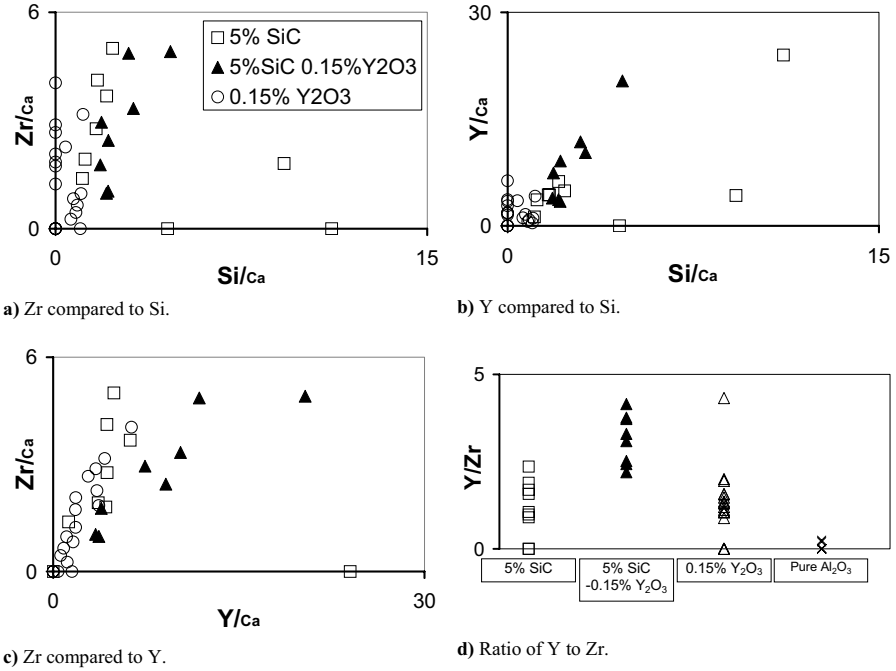

a) Zr compared to Si.

b) Y compared to Si.

c) Zr compared to Y.

d) Ratio of Y to Zr.

Figure 5: Relative amounts of elements normalised to Ca by wt%

However, all materials included Zr rich particles which are expected to have been introduced by the ZrO_2 milling media used in processing.

STEM-EDX analysis of grain boundaries was successful in revealing segregated elements (Figure 3a). Profiles of grain boundaries (Figure 4) allowed the amount of segregant to be quantified. Some spectra included an artefact 0.3 keV lower than the Al peak, with ~ 4 % of the Al intensity. This peak was removed by conditioning of the X-ray detector. The artefact was close to the characteristic energies of Mg and Na so would mask small quantities of these elements. All samples contained Ar, which was used in ion milling samples to electron transparency. This artefact is not expected to effect results.

The average monolayer fraction was between 23 and 36 % for materials made with „easy sintering“ alumina, which shows significant coverage (Table 3). The Si and Ca are expected to be introduced by impurities in the starting powder (Table 1) which segregate to grain boundaries. Si is additionally introduced to some samples by the addition of SiC with a surface layer of SiO_2. The Zr and Y are expected to have been introduced by the incorporation of particles of the milling media which dissolves and segregates to grain boundaries. EDX of the milling media revealed that it is Y_2O_3 stabilised ZrO_2 containing 4 % Y which explains the introduction of Y to grain boundaries in materials with no sintering aid added.

However, the ratio of Si, Ca, Y and Zr in materials made with „easy sintering“ alumina was found to vary by as much as 30 times (Figure 5). No pattern to this variation was observed. Further work is necessary to explain this.

The ratio of Y to Zr at grain boundaries was found to be high in materials made with „easy sintering“ alumina, but low in the „pure“ alumina sample (Figure 5d). This suggests that the way in which Y and Zr segregate is effected by the presence of other elements.

5 Conclusions

The additions to and impurities in alumina have a significant effect on the chemistry of grain boundaries in the materials studied. Segregated elements produce up to a third of a monolayer coverage. 5 vol% SiC addition increases the segregation of silicon from 8 to up to 20% of a monolayer. There is a strong segregation of Y to grain boundaries; the degree of segregation is interdependent on other elements.

The technique used was successful in analysing the composition of grain boundaries. Ongoing investigation of grain boundary chemistry and correlation with grain boundary structure and strength will allow better explanation of the properties of Al_2O_3/SiC nanocomposites.

6 Acknowledgements

The authors would like to acknowledge support from Morgan Advanced Ceramics (Stourport-on-Severn, UK). This work was performed under EPSRC grant number: GR/N06601. JMT acknowledges support from INSS and BNFL.

7 References

[1] K. Niihara, A. Nakahira in Advanced Structure Inorganic Composites (Ed.: P. Vincenzini), Elsevier Science Publishers, 1991, p. 637
[2] J. Zhao, L. C. Stearns, M. P. Harmer, H. M. Chan, G. A. Miller, R. F. Cook, J. Am. Ceram. Soc., 1993, 76, 503–510
[3] C. E. Borsa, S. Jiao, R.I. Todd, R. J. Brook, J. Microsc., 1995, 177, 305–312
[4] R. W. Davidge, R. J. Brook, F. Cambier, M. Poorteman, A. Leriche, D. O'Sullivan, S. Hampsire, T. Kennedy, Brit. Ceram. T., 1997, 96, 121–127
[5] B. Derby, Curr. Opin. Solid St. M., 1998, 3, 490–495
[6] D. Sciti, J. Vicens, A. Bellosi, J. Mater. Sci., 2002, 37, 3747–3758
[7] I. Levin, W. D. Kaplan,D. G. Brandon, T. Wieder, Acta Metall. Mater., 1994, 42, 1147–1154
[8] R. I. Todd, M. A. M. Bourke, C. E. Borsa, R. J. Brook, Acta Mater., 1997, 45, 1791–1800
[9] H. Z. Wu, S. G. Roberts, B. Derby, Acta. Mater., 2001, 49, 507–517
[10] H. Z. Wu, C. W. Lawrence, S. G. Roberts, B. Derby, Acta. Mater., 1998, 46, 3839–3848
[11] A. M. Thompson, H. M. Chan, M. P. Harmer, J. Am. Ceram. Soc., 1995, 78, 567–571
[12] I. A. Chou, H. M. Chan, M. P. Harmer, J. Am. Ceram. Soc., 1996, 79, 2403–2409
[13] S. Jiao, M. L. Jenkins, R. W. Davidge, J. Microsc., 1997, 185, 259–264
[14] H. K. Schmid, J. Microsc., 1999, 194, 192–202

[15] L. P. Ferroni, G. Pezzotti, T. Isshiki, H.-J. Kleebe, Acta Mater., 2001, 49, 2109–2113
[16] R. L. Coble, J. E. Burke in Progress in Ceramic Science, Vol. 3 (ed.: J. E. Burke) Pergamon Press, New York, USA, 1963, p. 197
[17] C. S. Kumar, Ph.D. thesis, University of Limerick, Ireland, 2001
[18] I. A. Vatter, J. M. Titchmarsh, Surf. Interface Anal., 1997, 25, 760–776
[19] M. Rühle, E. Bischoff, O. David, Ultramicrsocopy, 1984, 14, 37–46
[20] D. B. Williams, C. B. Carter, Transmission Electron Microscopy, Plenum Press, USA, 1996
[21] A. M. Cock, R. I. Todd, S. G. Roberts, in preparation
[22] L. Carroll, M. Sternitzke, B. Derby, Acta Mater., 1996, 44, 4543–4552

A Neutron Powder Diffraction Study of FeCo-SiO_2 Nanocomposites

Maria F. Casula, Anna Corrias, Guido Ennas, Sergio Marras and Giorgio Paschina
Dipartimento di Scienze Chimiche, Universita' di Cagliari, 09042 Monserrato (CA), Italy

1 Abstract

Neutron diffraction was used to study the order-disorder tranformation from the α'-CsCl to the α-bcc phase in nanocrystalline equiatomic FeCo alloys dispersed in a silica matrix. The disordered phase or a mixture of the α and α' phases are found in the samples depending on the preparation route of the samples. Neutron diffraction experiments carried out during in-situ heating indicate that the ordered phase forms above 600 °C, below the temperature of 730 °C typical of bulk FeCo alloys.

2 Introduction

Transition metal nanocrystals dispersed in an insulator matrix have attractive magnetic and transport properties for the development of composite-based micro- and nano-devices. In particular, the preparation of alloy nanocrystals allows to tailor the magnetic properties as a function of the composition, since it is well known that alloys have peculiar magnetic properties different form those of single metals.

In the bulk, Fe and Co form alloys over a wide composition range (at room temperature from pure iron to about 75 wt% Co). [1] Due to their technological importance, the properties of FeCo alloys have been extensively studied as a function of composition and temperature, pointing out the presence of discontinuities in the physical properties due to a continuous order-disorder transformation. The phase transition involves the transformation from the ordered α'-CsCl type to the disordered α-bcc type phase which occurs at a maximum temperature of 730 °C for the equiatomic alloy. [2] Although the magnetic behaviour is very similar, the disordered phase has a larger ductility and resistivity and is therefore more suitable for materials processing.

The occurrence of the order-disorder transition in nanostructured iron-cobalt alloys is still largely unexplored. The study of the ordering in nanostructured FeCo alloys is important from the standpoint of potential technological applications and of the understanding of finite size effects on phase transitions.

Neutron powder diffraction, which can be used to identify the ordered α' phase because it gives rise to superlattice reflections [3,4], was used in this work to study the structure of equiatomic FeCo nanocrystals dispersed in a silica matrix. The effect of synthetic parameters on the sol-gel preparation of FeCo-SiO_2 nanocomposites was studied.

3 Experimental

$FeCo-SiO_2$ nanocomposites were prepared in the form of xerogels and aerogels by a sol-gel procedure reported elsewhere. [5, 6] The total metal amount in the nanocomposite (Fe+Co)·100/(Fe+Co+SiO_2) is 10 wt% and the molar ratio between Fe/Co = 1. The preparation route of the xerogel and aerogel samples differs in the precursors of the metal phase and in the drying procedure. Acetate and nitrate salts were used to synthesise xerogels and aerogels respectively. In both cases the gel is prepared by co-hydrolysis of the metal salts and the tetraethoxysilane in ethanolic media under acidic catalysis. Gelation is carried out at ambient conditions and the drying is performed by conventional calcination in the case of the xerogel sample and by high temperature supercritical drying in an autoclave in the case of the aerogel. The final $FeCo-SiO_2$ nanocomposites were prepared by a reduction treatment at 800 °C for 2 hours under H_2 flow; the samples obtained starting from the xerogel and the aerogel will be named hereafter sample X and A respectively.

The structural and morphological characterization was performed by transmission electron microscopy (TEM) and X-ray powder diffraction (XRD).

TEM micrographs were recorded on a JEOL 200CX microscope operating at 200 kV. The samples were dispersed in n-octane and dropped on a conventional carbon-coated copper grid.

XRD spectra were recorded on a X3000 Seifert diffractometer equipped with a graphite monochromator on the diffracted beam using Cu Kα radiation.

Neutron diffraction spectra were collected on the $FeCo-SiO_2$ nanocomposites using the high intensity POLARIS time-of-flight (TOF) diffractometer at the ISIS spallation neutron source (Rutherford Appleton Laboratory in Chilton, UK). The POLARIS experimental station is equipped with in situ-heating apparatus; both the sample can and the furnace are made in vanadium. Neutron diffraction spectra were collected at room temperature both on the X and A nanocomposite samples. The neutron diffraction spectra of the A sample were also collected during an heating-cooling cycle in ultra-high vacuum. In principle, the high intensity of the neutron source and the TOF collection mode allow relatively rapid data collection. Due to the low amount of the metallic phase in the nanocomposite, however, a minimum acquisition time of 6 hours was required for each run.

Rietveld refinements of the neutron diffraction profiles were carried out using the PC version of the GSAS (Generalized Structure Analysis System) program. [7] The variables were the unit cell parameters of the α and α' phase, the parameters of the pseudo-Voigt function used to model the sample contribution to the peak shape and the phase fractions.

4 Results and Discussion

Figure 1 shows the XRD spectra of the X and A samples. The spectra of both samples exhibit the peaks of a nanophase superimposed to a background due to amorphous silica. The crystallite size as estimated from line broadening by the Scherrer formula indicates a crystallite size of 10 nm for both the X and A samples. The peaks of the nanophase can be attributed to the FeCo alloy. It is noteworthy that no other phase is detected by XRD, and in particular no trace of oxides is present.The lattice parameter for the alloy, however, is very similar to the lattice parameter of bcc-Fe (2.857 Å vs 2.886 Å) and it is therefore not possible to state unambiguously the formation of the alloy from the XRD pattern. The formation of the alloy was verified by studying sepa-

rately the Fe and Co environment by exploiting the selectivity of XAS technique. [8] XAS indicates that both Fe and Co in the nanocomposite samples have a bcc environment, confirming therefore the formation of the alloy. A further evidence was obtained by Mössbauer Spectroscopy, which gives parameters typical of the iron nuclei in the FeCo alloy. [9]

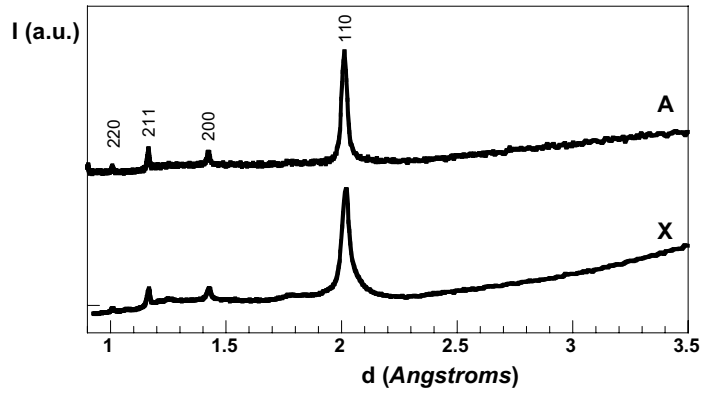

Figure 1: X-Ray diffraction spectra of the X and A FeCo-SiO_2 nanocomposites

Figure 2a and c shows the TEM micrographs of the nanocomposite samples obtained in the bright field mode. In agreement with XRD data, we can observe the presence of alloy nanoparticles dispersed over the amorphous silica matrix. It is noteworthy that the silica matrices in the X and A samples have a different porosity, which is also reflected in the distance between the nanoparticles. In particular, in the A sample the silica has a higher porosity and larger pores, as expected for aerogel samples and confirmed by physisorption measurements [5]. TEM observations indicate that the nanoparticles have a round shape both in sample X and A and that the average size is 12 nm and 10 nm respectively, in agreement with XRD data. The selected area electron diffraction (SAED), reported in Figure 2b and d for the X and A samples respectively, confirms the presence of a bcc-type nanocrystalline phase. High Resolution TEM observations indicate that the nanoparticles are single crystals [10].

The structural data obtained by X-rays and electron diffraction techniques do not allow to verify whether the alloy is present in the ordered (α') or in the disordered (α) phase. The α' phase has a CsCl structure where each Co atom nearest neighbours are always Fe atoms (and vice versa), whereas in the disordered α bcc structure the Co or Fe have random neighbours. The peaks detected by XRD and SAED have Miller indices satisfying the rule $h + k + l = 2n$, whereas the superlattice peaks $h + k + l = 2n + 1$ characteristic of the ordered α' phase would have negligible intensity due to the small difference in the scattering factors of Fe and Co. The superlattice reflections, however, can be detected by neutron diffraction, thanks to the large contrast between the neutron form factors of Fe and Co.

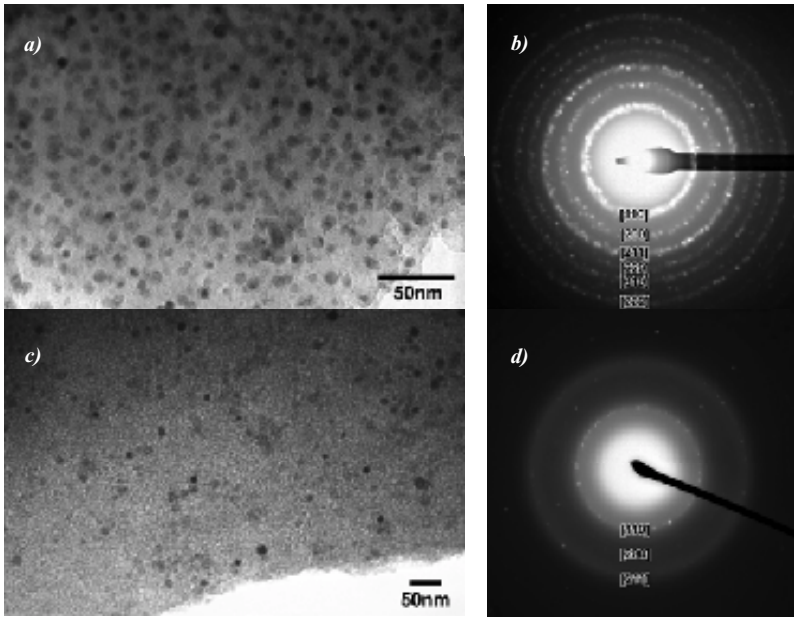

Figure 2: Transmission electron microscopy image and corresponding electron diffraction for the X (*a, b*) and A (*c, d*) samples

Figure 3 shows the neutron diffraction spectra at room temperature for the aerogel and xerogel nanocomposite samples. The small peak at 2.14 Å in the spectra od the X and A samples is the most intense peak of vanadium and arises from the sample holder. The spectrum of the X sample shows the presence of reflections typical of the disordered FeCo alloy. This result is quite interesting since in bulk FeCo alloys the ordered phase is stable up to 730 °C and the or-

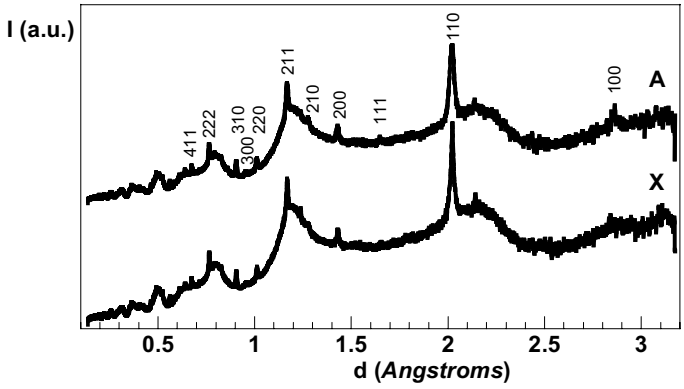

Figure 3: Time-of-flight neutron diffraction spectra of the X and A FeCo-SiO_2nanocomposites at room temperature

dered phase is formed even in severely quenched samples. The diffraction spectrum of the A sample shows the superlattice reflections, indicating the presence of the ordered phase. However, the intensity ratios between the two families of reflections suggests that the disordered phase is also present.

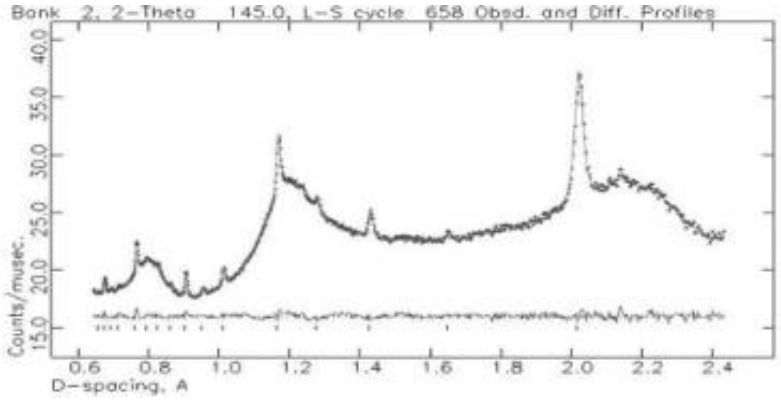

Figure 4: Experimental and calculated neutron diffraction spectra of the A nanocomposite at room temperature as obtained from Rietveld refinement. The difference plot and the peak positions of the α and α' phases are also reported.

Quantitative information concerning the relative amounts of the α' and α phases in the sample, the strain and size contributions to the diffraction profile were obtained by Rietveld analysis. The best fitting, reported in Fig.4, gives relative amounts of the ordered α' and disordered α phase of 43 % and 57 %. The Rietveld profile analysis indicates that strain is negligible, the main contribution to peak broadening being related to finite size effects. The average crystallite size of the ordered alloy is significantly higher than that of the disordered one.

Figure 5 reports the neutron diffraction spectra of sample A during a heating-cooling cycle from RT to 750 °C with steps of 150 °C. These spectra allow to point out several interesting features of the structural evolution of the nanocomposite as a function of temperature. First of all, from the disappearence of the superlattice reflections we can see that above 600 °C all the ordered phase transforms into the disordered one. On cooling, the ordered phase is recovered below 450 °C. Moreover, at 750 °C other nanocrystalline peaks are also observed at 1.53 Å, 1.8 Å, 2.07 Å, 2.17 Å and 2.19 Å, which are retained on cooling. These peaks can be ascribed to the iron silicate fayalite (Fe_2SiO_4) and to the fcc Co phase.

It is likely that the long heating procedure results in an interaction between the alloy nanoparticles and the silica matrix inducing the formation of some iron silicate and the corresponding segregation of the excess Co. In particular, a significant shift of the 110 peak of the FeCo alloy at higher d values is observed with increasing the temperature, due to the change in composition of the alloy towards the Fe_7Co_3 composition and to the convolution with the most intense peak of fcc Cobalt.

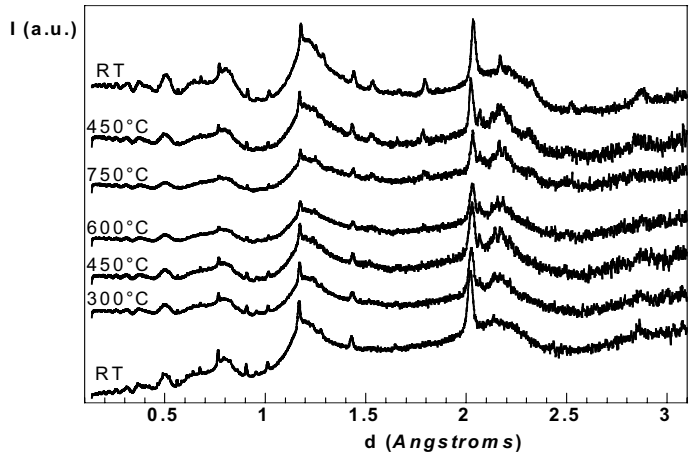

Figure 5: Time-of-flight neutron diffraction spectra of the A nanocomposite during in-situ heating and cooling under vacuum

5 Conclusions

Neutron diffraction confirmed to be a useful tool to investigate the ordering of the FeCo alloy, giving valuable information which could not be deduced from electron or X-Ray diffraction techniques.

It was found that in the X nanocomposite the alloy is mainly present in the disordered form, whereas a mixture (almost equal amounts) of disordered and ordered phases is present in the aerogel. This difference can be tentatively ascribed to the difference in average crystallite size in the two samples, and in particular the disorderd phase seems to be favoured in smaller nanocrystals. In the A sample the disordered phase has smaller nanocrystals than the ordered one, in agreement with the previous picture. The effect of the different precursors used to prepare the X and A samples on the alloy structure, however, cannot be ruled out.

The dispersion of the alloy nanoparticles in the silica matrix allows one to study the order-disorder phase transition during heat treatments minimizing nanocrystal aggregation and growth. On the other hand, the interaction between nanoparticles and the silica matrix can also partially occur as a secondary reaction on heating.

6 Acknowledgements

Ron Smith is gratefully acknowledged for his help in performing the neutron diffraction experiments. This work was supported by the Ministero dell'Istruzione, dell'Università e della Ricerca (MIUR) under contract PRIN 2001038849_004.

7 References

[1] A. Fernandez-Guillermet, High Temp. High Press., 19 (1988) 477
[2] Z. Turgut, M.Q. Huang, K. Gallagher, M.E. McHenry and S.A. Majetich, J. Appl. Phys. 81 (1997) 4039
[3] J.H.J. Scott, K. Chowdary, Z. Turgut, S.A. Majetich, M.E. McHenry, J. Appl. Phys. 85 (1999) 4409
[4] C.G. Shull and S. Siegel, Phys. Rev. 75 (1949) 1008
[5] M.F. Casula, A. Corrias and G. Paschina., J. Mater. Chem., 2002, 12, 1505–1510
[6] G. Ennas, M.F. Casula, A. Falqui, D. Gatteschi, G. Marongiu, G. Piccaluga, C. Sangregorio and G. Pinna, J.Non-Cryst. Solids, 2001, 293–295, 1–9
[7] R. B. Von Dreel and A. C. Larson, in LANSCE Newsletter no. 4, Los Alamos, NM Winter 1988
[8] A. Corrias, M.F.Casula, G. Ennas, S. Marras, G. Navarra and G. Mountjoy, J. Phys. Chem. B, 2003, 107, 3030–3039
[9] G.Concas, F.Congiu, G.Ennas, G. Piccaluga, G.Spano, J. Non-Cryst. Solids, 2003, 330, 234–241
[10] A.Falqui, V. Serin, L. Calmels, E. Snoeck, A. Corrias, G. Ennas, J. Microscopy 2003, 210, 80–88

Acidity Characterization of Nanocyrstalline H-ZSM-5 Zeolites by ^{31}P MAS NMR of Adsorbed Phosphine Oxide Probes

Wen-Hua Chen[a], Shing-Jong Huang[a], Ayyamperumal Sakthivel[a], S. P. Naik[b], Anthony S. T. Chiang[b] and Shang-Bin Liu[a,*]

[a]Institute of Atomic and Molecular Sciences, Academia Sinica, P. O. Box 23-166, Taipei 106, Taiwan, ROC. [b]Department of Chemical and Materials Engineering, National Central University, Chung-Li 320, Taiwan, ROC.

1 Introduction

Nanocrystalline zeolites are known to posses several important characteristics, such as high external surface area, faster mass and heat transfer and less vulnerable to deactivation [1, 2], which render many potential applications, for example, as catalysts or supports for composite materials during industrial processes, fabrication of thin films or membranes as well as ultra-low k materials for next generation electronics etc. [3–6]. In particular, for their applications in catalysis, nanocrystalline zeolites are known to have superior catalytic activity with lower deactivation rate and longer life [2].

Medium-pore ZSM-5 zeolites are suitable catalysts for shape selectivity reactions, which are normally catalyzed by acid sites located predominantly within the intracrystalline pore/channels (typical crystalline size ca. 0.1–10 μm). However, as the crystalline size of the catalyst is reduced to nanometer scale, its catalytic performance should mostly be invoked by extracrystalline molecular diffusion and hence surface reaction should begin to play an important role [7]. Thus, a detailed understanding of the acid features, viz. nature, location, strength and concentration of acid sites, on nanocrystalline catalysts is a demanding task.

A novel solid-state ^{31}P MAS NMR technique developed recently reveals the propensity in simultaneous determination of the types and strengths of acid sites in zeolites and related catalysts using trialkylphosphines or trialkylphosphine oxides as the probe molecules [8-15]. The advantages of using these phosphorus molecules over other more conventional NMR probes, such as pyridine or methylamine, are a higher sensitivity and a wider chemical shift range (> 300 ppm) possessed by the ^{31}P nucleus (I = 1/2, natural abundance 100 %) compared to ^{13}C or ^{15}N. The type (Brønsted vs. Lewis acidity), distribution and strength of acid sites in the porous catalysts can be directly inferred from the variations in the observed ^{31}P NMR resonance. Whereas, as demonstrated in a recent report [16], the locations (internal vs. external) of the acid sites may be differentiated by using suitable probe molecules having different sizes, namely trimethylphosphine oxide (TMPO) and tributylphosphine oxide (TBPO). Unlike TBPO (kinetic diameter ca. 0.82 nm), which can only be adsorbed on the external surfaces of 10-membered ring (10-MR) zeolites such as H-ZSM-5 (pore aperture ca. 0.6 nm), TMPO (ca. 0.55 nm) is capable of entering the channels of the zeolites and hence rendering simultaneous detection of internal and external acidity. In addition, quantitative information of the acid sites (i.e., acid concentration) can further be derived when ^{31}P NMR experiment is performed in conjunction with elemental analysis by ICP-MS.

The objective of this study is to characterize the properties of acid sites in nanocrystalline (size 20–500 nm) H-ZSM-5 zeolites by means of solid-state ^{31}P MAS NMR of adsorbed phos-

phine oxide probes, in conjunction with elemental analysis, diffuse reflectance Fourier-transform infrared spectroscopy (DRIFTS) and solid-state ^{1}H and ^{27}Al MAS NMR.

2 Experimental

2.1 Materials

H-ZSM-5 zeolites with different crystalline size (20–500 nm) were synthesized by various methods (steaming, colloidal and hydrothermal) and experimental conditions [17]. Their structural features were confirmed by powder X-ray diffraction (XRD) and Fourier-transform infrared spectroscopy (FT-IR). Whereas, their Si/Al ratios, crystalline sizes and BET surface areas (and pore volumes) were determined by elemental analysis (ICP-MS), scanning/transmission electron microscopy (SEM/TEM) and N_2 adsorption/desorption measurements (77 K), respectively. The preparation conditions and characteristics of these samples were depicted in Table 1 together with a commercial H-ZSM-5 zeolite (Strem Chemicals Inc.) with an averaged crystalline size of ca. 2.0 μm and Si/Al = 65.

Table 1: Physical and acidic properties of various nanocrystalline H-ZSM-5 Zeolites

Samples	Preparation method	Si/Al	Crystal size (nm)	Surface area (m^2/g)		Pore volume (mL/g)		Percentage of ext. (%)	
				BET	ext.	meso.	micro.	area[a]	acidity[b]
S-80	steaming (80 °C; 22 h)	61	< 50	835	550	0.17	0.04	65.9	19.6
S-100	steaming (100 °C; 22 h)	59	–[c]	337	222	0.07	0.01	65.9	31.4
C-80	colloidal (80 °C; 36 h)	53	270	475	200	0.10	0.10	42.1	17.6
C-100	colloidal (100 °C; 12 h)	57	500	425	150	0	0.12	35.3	3.2
H-125	hydrothermal (125 °C; 24 h)	45	375	569	230	0.10	0.12	40.4	13.6
H-ZSM-5	commerical	65	2,000	–	–	–	–	–	8.3

[a]Data obtained from N_2 adsorption/desorption measurements (77 K).
[b]Data obtained from ^{31}P MAS NMR and ICP-MS.
[c]Undetectable.

2.2 Characterization Methods

All ^{31}P MAS NMR spectra were acquired at a Larmor frequency of 202.46 MHz on a Bruker MSL-500P instrument using a single pulse sequence under the following conditions: pulse-width, 2 μs; recycle delay, 5 s; spinning rate, 10–12 kHz. Prior to the experiment, each sample was subjected to dehydration treatment at 623 K for 48 h under vacuum (10^{-5} Torr). Detailed

procedures involved in preparing samples loaded with various P-containing probe molecules (TMPO and TBPO) and the related experimental setups, have been reported elsewhere [16, 18]. A single pulse sequence was also used for ^{27}Al MAS NMR experiments under a sample spinning rate of 12 kHz; pulse-width 1 μs (p/6), and recycle delay of 500 ms at a resonance frequency of 130.32 MHz. On the other hand, ^{1}H MAS NMR spectra were obtained from dehydrated samples by rotor-synchronized spin-echo pulse sequence operating at a frequency of 500.14 MHz, spinning rate 5 kHz and a recycle delay of 15 s. Tetramethylsilane (TMS), aqueous 85 % H_3PO_4 and 1M Al $(H_2O)_6^{3+}$ solutions were taken as external references for ^{1}H, ^{31}P and ^{27}Al NMR chemical shifts, respectively. To afford the quantitative determination of the acid sites, each adsorbed-loaded sample was also subjected to element analyses by ICP-MS. Infrared spectroscopy (DRIFTS; Bruker IFS-28) was also utilized to characterize acidity. Sample was dehydrated in situ at 473 K for at least 0.5 h before each run.

3 Result and Disscusion

3.1 ^{27}Al MAS NMR

^{27}Al MAS NMR spectra obtained from various hydrated samples are shown in Fig. 1a along with a commercial H-ZSM-5 sample. Hydration treatment was accomplished by placing the samples in a desiccatr under saturated NaCl solution at ambient temperature for at least 3 d. In despite of the presence of small amount of extra-framework (octahedral-coordinated) Al species at ca. 0 ppm, it is clear that majority of Al species are tetrahedrally coordinated in the framework of nanocrystalline H-ZSM-5 zeolites resulting a main resonance peak at ca. 55 ppm, except for the S-80 sample.

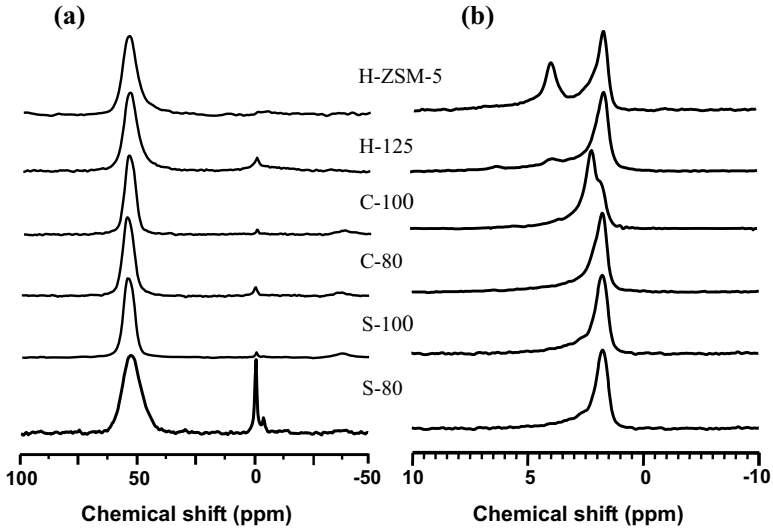

Figure 1: (a) 27 Al and (b) 1H MAS NMR spectra obtained from various nanocrystalline H-ZSM-5 zeolites

3.2 ^{1}H MAS NMR and DRIFT spectroscopy

Solid-state ^{1}H MAS NMR and DRIFT spectroscopic techniques are commonly used for determining the types of hydroxyl groups in dehydrated solid acid catalysts. In terms of their local structure types, ^{1}H NMR signals of the silanol groups (SiOH) normally have chemical shifts of 1.2–2.2 ppm, the hydroxyl protons on extra-framework aluminum species (AlOH) should appear at chemical shifts of 2.6–3.6 ppm, whereas the bridging hydroxyl groups (SiOHAl) cover the range 3.6–7.0 ppm [19]. The bridging OH groups, which act as the proton donor (Brønsted acid) sites, are responsible for catalyzing chemical reactions. On the other hand, the IR absorption peaks at 3740, 3650, and 3600 cm^{-1} can be assigned to hydroxyl vibration (O-H stretching) bands of SiOH, AlOH, and SiOHAl groups, respectively [20].

Figure 1b displays the ^{1}H MAS NMR spectra of various dehydrated nanocrystalline samples together with the commercial H-ZSM-5 sample. That the spectrum obtained from the commercial sample exhibits two resonance lines at 3.9 and 1.9 ppm, whereas only a single resonance at 1.9 ppm was observed from the other samples indicating that the ^{1}H MAS NMR failed to detect Brønsted acidity in the nanocrystalline samples. This is attributed due to the presence of excessive amount of silanols than bridging hydroxyl groups. Similar observations were found for the DRIFT spectra of dehydrated nanocrystalline samples (not shown), in which the absorption band responsible for the bridging hydroxyl groups (at 3600 cm^{-1}) is barely visible.

3.3 ^{31}P MAS NMR of Adsorbed TMPO and TBPO

Additional ^{31}P MAS NMR was invoked to verify the acid features in nanocrystalline H-ZSM-5 zeolites using TMPO and TBPO as the probe molecules. It has been proposed that, upon adsorbing phosphine oxides on an acid catalyst, the base guest molecules may readily interact with Brønsted acid sites to form hydrogen-bonded complexes. The formation of such complexes is provoked by O–H bonding of partially negative-charged oxygen atoms on the organic oxide probe molecule and the bridging hydroxyl groups (which act as proton donor) in zeolite adsorbents [14, 16]. Consequently, the density of the electron cloud surrounding the ^{31}P nucleus neighboring to the oxygen atom on the phosphine oxides decreases with increasing strength of the Brønsted acid sites, which in turn causes the ^{31}P resonance to shift towards downfield (higher chemical shift) direction. In other words, ^{31}P NMR resonance having a higher chemical shift should reflects Brønsted acidity with a higher acidic strength.

^{31}P MAS NMR spectra obtained from samples respectively loaded with TMPO and TBPO are depicted in Fig. 2. The dashed curves represent results of spectral simulation by Gaussian deconvolution method. The shaded peaks, which represent signals arising from physisorbed TMPO or TBPO guest molecules, are irrelevant to Brønsted acidity and hence their contribution may be subtracted and disregarded during quantitative analyses. It is noted that, dramatic changes in the distribution of acid sites (^{31}P resonance peaks) in nanocyrstalline H-ZSM-5 prepared by different methods may be seen compared with the commercial H-ZSM-5 sample. For example, the ^{31}P MAS NMR spectra of TMPO adsorbed on the nano-sized H-ZSM-5 zeolite synthesized by steaming method (S-80 and S-100) show only two distinct resonance at 71 and 66 ppm, whereas three resonance were found in commercial H-ZSM-5 and up to seven peaks were found responsible for TMPO interacting with Brønsted acid sites for samples prepared by colloidal (C-80 and C-100) and hydrothermal (H-125) methods. In the case of adsorbed TBPO,

only one type of acid site (74 ppm) can be identified for sample prepared by steaming and colloidal methods, whereas three peaks (at 91, 74 and 69 ppm) were found responsible for external acidity for the commercial H-ZSM-5 and samples prepared by hydrothermal method (H-125). Quantitative information of acid sites can further be derived by incorporating results obtained from elemental analyses of Si, Al and P by ICP-MS. This is made possible by assuming the total peak areas responsible for Brønsted acid sites is 100 % (excluding physisorbed peak) and a one-on-one (1 : 1) correspondence of adsorbed each phosphine oxide with one acid site. A detailed analysis procedure can be found elsewhere [16]. Accordingly, the concentrations of internal vs. external acid sites arise from acid sites having the same acidic strength (chemical shift) for various samples can be inferred, as depicted in Table 2.

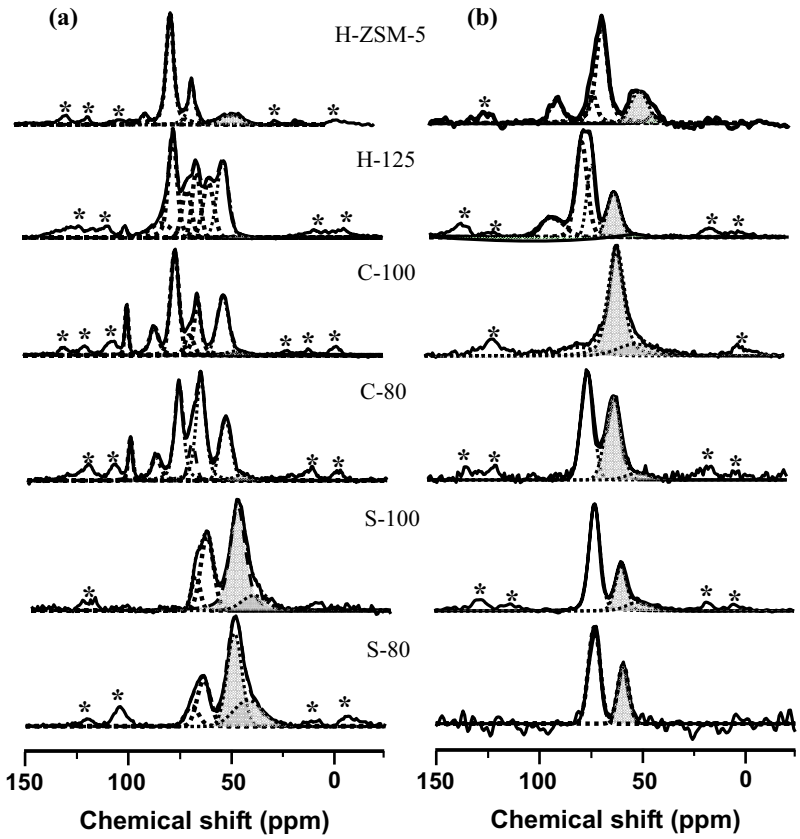

Figure 2: ^{31}P MAS NMR spectra obtained from commercial and various nanocrystalline H-ZSM-5 zeolites loaded with (a) TMPO and (b) TBPO. The shaded peaks represent physisorbed TMPO or TBPo, the asterisks denote spinning side-bands.

Table 2: ^{31}P MAS NMR chemical shift assignments and distribution of acid sites of various nanocrystalline H-ZSM-5 Zeolites loaded with TMPO and TBPO probe molecules

(Δδ; ppm)[a]	61	47	38	32	27	21	15	10	4
TMPO (internal + external)									
Chemical shift (ppm)	100	86	77	71	66	60	54	49[d]	43[d]
Sample[b]									
S-80		–	–	30.0% (0.029, –)	70.0 % (0.049, 0.019)	–	–	Y	Y
S-100	–	–	–	23.9 % (0.017, –)	76.1 % (0.031, 0.022)	–	–	Y	Y
C-80	5.6 % (0.011, -)	7.4 % (0.015, –)	27.1 % (0.054, –)	8.3 % (0.016, –)	31.4 % (0.028, 0.035)	–	20.2 % (0.040, –)	Y	–
C-100	6.9 % (0.015, -)	10.7 % (0.023, –)	34.0 % (0.074, –)	6.6 % (0.014, –)	16.3 % (0.029, 0.007)	–	25.5 % (0.055, –)	Y	–
H-125	2.0 % (0.006, -)	8.2 % (0.015,0.008)	25.1 % (0.070, –)	11.9 % (0.034, –)	14.0 % (0.020, 0.019)	15.8 % (0.033,0.011)	23.0 % (0.064, –)	Y	–
H-ZSM-5	–	3.5 % (0.003,0.002)	69.8 % (0.108, –)	–	– (–, 0.002)	26.7 % (0.032,0.009)	–	–	Y
TBPO (external)									
Chemical shift (ppm)	–	91	–	–	74	69	–	58[d]	49[d]
Sample[c]									
S-80	–	–	–	–	100 %	–	–	Y	–
S-100	–	–	–	–	100 %	–	–	Y	Y
C-80	–	–	–	–	100 %	–	–	Y	Y
C-100	–	–	–	–	100 %	–	–	Y	Y
H-125	–	20.7 %	–	–	50.2 %	29.1 %	–	Y	Y
H-ZSM-5	–	15.4 %	–	–	17.6 %	67.0 %	–	–	Y

[a]Data (Δδ ± 3 ppm) refer to the corresponding chemical shift differences with respect to crystalline TMPO (39ppm) or TBPO (47 ppm).
[b]Values on top represent relative concentration of acid sites (%); data in parenthesis (*int*, *ext*) give the amounts of internal and external acid sites (± 0.002 mmol/g cat.), respectively.
[c]Values specifically represent relative concentration of external acid sites (%).
[d]Resonance arise from physisorbed TMPO or TBPO.

In an earlier study [16], we have shown that the respective ^{31}P resonance observed from TMPO and TBPO adsorbed on acid sites with the same acidic strength can be correlated by the chemical shift difference ($\Delta\delta \pm 3$ ppm) between the observed chemical shift with respect to that

of their crystalline bulks, namely 39 ppm for TMPO and 47 for TBPO. Accordingly, experimental results respectively obtained from TMPO (which is capable of probing both internal and external acidity) and TBPO (which can only probe external acidity) can be correlated, as the result, qualitative and quantitative information of both internal and external acidity can be obtained. For example, for sample H-125, up to seven peaks can be resolved from the ^{31}P NMR of adsorbed TMPO, namely 100, 86, 77, 71, 66, 60 and 54 ppm (in order of decreasing acid strength), whereas only three resonance can be identified in the case of adsorbed TBPO (i.e., 91, 74 and 69 ppm). The latter three resonance, being having a respective $\Delta\delta$ value of 44, 27 and 22 ppm can thus be correlated to the three resonance at 86, 66 and 60 ppm obtained from TMPO, which is found to have a similar respective $\Delta\delta$ value of 47, 27 and 22 ppm. On the other hand, for the same system (TMPO/H-125), the other peaks with chemical shift of 100, 77, 71 and 54 ppm, which corresponds to respective $\Delta\delta$ value of 61, 38, 32 and 15 ppm (see Table 2) are not visible in spectrum obtained from TBPO/H-125. Thus, these peaks may be ascribed due to TMPO adsorbed on acid sites strictly located in the intracrystalline channels of sample H-125.

By comparing the results obtained from various samples in Table 2, it is indicative that, in terms of acidic strength, nanocrystalline H-ZSM-5 samples prepared by different methods follow the trend: C-100 > C-80 > H-125 > S-80 ≥ S-100. That is, colloidal method is superior in preparing nanocrystalline H-ZSM-5 catalysts having higher overall acidic strengths. In view of total (internal and external) acidity, a value of 0.156, 0.280, 0.217, 0.199, 0.070 and 0.097 is found for commercial H-ZSM-5, H-125, C-100, C-80, S-100 and S-80, respectively. Nanocrystalline H-ZSM-5 samples prepared by the hydrothermal or colloidal methods therefore are capable of producing catalysts having the overall acid properties analogous to commercial zeolite. However, unlike H-125, which observed three different types of external acidity similar to commercial H-ZSM-5, only one type of external acid site was found for samples prepared by steaming and colloidal methods, resulting an overall increase in external acidity typically by 2-4 folds compared to the commercial sample (see Table 1). Moreover, while a consistent increase in external surface area with decreasing crystalline size, samples prepared by steaming methods seem to be more favorable for promoting external surface area and external acidity compared to that prepared by colloidal or hydrothermal methods.

4 Conclusion

The acidic properties of nanocrystalline H-ZSM-5 zeolites synthesized under various conditions, namely by steaming, colloidal and hydrothermal methods at different temperatures have been characterized by solid-state ^{31}P NMR of adsorbed phosphine oxide probe molecules (TMPO and TBPO). Both qualitative and quantitative information of Brønsted acid sites may be obtained when the results are incorporated with N_2 adsorption/desorption, ^{1}H and ^{27}Al MAS NMR, DRIFT and elemental analysis by ICP-MS. It is found that steaming method is more favorable for preparing nano-sized H-ZSM-5 samples with smaller crystalline size and improved eternal acidity. Whereas samples prepared by colloidal or hydrothermal methods are more superior for preparing catalysts with broader distribution of acid sites that having a higher overall acidic strengths. The unique methodology reports here is capable of obtaining the detailed acid features of nano-sized solid acid catalysts simultaneously, including their acid type, location, concentration and strength of acid sites, which may not be achieved using conventional techniques.

5 Acknowledgements

The financial support of this work by the National Science Council, Taiwan, R.O.C. (NSC91-2113-M-001-030 to SBL) is gratefully acknowledged. The authors also thank Profs. H. M. Kao and T. C. Tsai for helpful discussions.

6 References

[1] S. B. Pu, T. Inui, Zeolites 1996, 17, 334–339
[2] M. Yamamura, K. Chaki, T. Wakatsuki, H. Okado, K. Fujimoto, Zeolites 1994, 14, 643–649
[3] S. Mintova, S. Mo, T. Bein, Chem. Mater. 1998, 10, 4030–4036
[4] G. Cho, J. S. Lee, D. T. Glatzhofer, B. M. Fung, W.L. Yuan, E. A. O'Rear, Adv. Mater. 1999, 11, 497–499
[5] C. S. Tsay, A. S. T. Chiang, AIChE J. 2000, 46, 616–62
[6] Z. Wang, H. Wang, A. Mitra, L. Huang, Y. Yan, Adv. Mater. 2001, 13, 746–749
[7] D. Fraenkel, Ind. Eng. Chem. Res. 1990, 29, 1814–1821
[8] L. Baltusis, J. S. Frye, G. E. Maciel, J. Am. Chem. Soc. 1986, 108, 7119–2120
[9] L. Baltusis, J. S. Frye, G. E. Maciel, J. Am. Chem. Soc., 1987, 109, 40–46
[10] J.H. Lunsford, W. P. Rothwell, W. Shen, J. Am. Chem. Soc. 1985, 107, 1540–1547
[11] J. H. Lunsford, Top. Catal. 1997, 4, 91–98
[12] B. Zhao, H. Pan, J. H. Lunsford, Langmuir 1999, 15, 2761–2765
[13] B. Hu, I. D. Gay, Langmuir 1999, 15, 477–481
[14] E. F. Rakiewicz, A. W. Peters, R. F. Wormsbecher, K. J. Sutovich, K. T. Mueller, J. Phys. Chem. B 1998, 102, 2890–2896
[15] J. P. Osegovic, R. S. Drago, J. Phys. Chem. B 2000, 104, 147–154
[16] Q. Zhao, W. H. Chen, S. J. Huang, Y. C. Wu, H. K. Lee, S. B. Liu, J. Phys. Chem. B 2002, 106, 4462–4469
[17] S. P. Naik, J. C. Chen, Anthony S. T. Chiang, Micropor. Mesopor. Mater. 2002, 54, 293–303
[18] W. H. Chen, T. C. Tsai, S. J. Jong, Q. Zhao, C. T. Tsai, I. Wang, H. K. Lee, S. B. Liu, J. Mol. Catal. A 2002, 181, 41–55
[19] M. Hunger, Cat. Rev.-Sci. Eng. 1997, 39, 345–393
[20] A. Auroux, V. Bolis, P. Wierzchowski, P.C. Gravelle, J.C. Védrine, J. Chem. Soc. Faraday Trans. I 1979, 75, 2544–2555

Fabrication of Multilayer Ultrathin Films through Layer-by-Layer Assembly of Delaminated MnO_2 Nanosheets and Polyelectrolytes

Lianzhou Wang, Yasuo Ebina, Kazunori Takada, Takayoshi Sasaki *
Advanced Materials Laboratory, National Institute for Materials Science, 1-1 Namiki, Tsukuba, Ibaraki 305-0044, Japan and CREST, Japan Science and Technology Agency (JST).

1 Introduction

Assembly of nanostructured transition metal oxides to form ordered architectures is of great interest in the fields of materials and chemistry. [1, 2] Thin films of the materials is one of the most desirable forms due to their advantages with respect to characterization and applications. The layer-by-layer self-assembly technique has provided an effective route for the fabrication of multilayer ultrathin films containing various inorganic/organic building blocks. [3–6] The technique is based on alternate adsorption of oppositely charged monolayers from their aqueous solutions. The resulting films generally have well-defined architecture and controllable thickness on a nanometer level, which may find potential applications including optical and electrochemical fields.

Manganese oxides have extensive applications as ion-exchanger, catalysts, and energy conversion materials. [7–9] Thin films of manganese oxides are also of great interest because they are suitable for optical, electrochemical and electronic studies, as well as their applications. [10–12] Various thin films of manganese oxides with submicro- to micrometer thickness have been fabricated using sol-gel, brushing, and spin/dip coating procedures, [13, 15] while rare reports focused on the fabrication of films through the LBL strategy. One exception is the LBL fabrication of manganese oxide nanoparticles (size: 2-8 nm), while control over film thickness remained to be improved. [15] We have recently reported the successful delamination of a layered manganese oxide of $K_{0.45}MnO_2$. [17] Redoxable unilamellar nanosheets of MnO_2 with a crystallographic thickness of ca 0.5 nm and a lateral dimension of sub-micrometers have been obtained. In this work, we report on the fabrication of multilayer ultrathin films using the sequential LBL deposition of MnO_2 nanosheets and polycations and their electrochemical performance examination. The molecular thickness and crystalline nature of the MnO_2 nanosheets render the films well-defined ultrathin architecture (tens of nanometer in thickness) and promising electrochemical properties.

2 Experimental

2.1 Reagents and Materials

Reagents, such as NaOH, K_2CO_3, Mn_2O_3, polyethylenimine (PEI) and poly(diallyldimethyl-ammonium) (PDDA) chloride, were of analytical grade. Ultrapure water with resistivity of 18.2 MΩ cm was obtained from a Milli-Q water purification system, and used throughout the experi-

ments. Colloidal suspension of delaminated MnO_2 nanosheets was prepared according to our recently reported procedure. [17]

2.2 Fabrication of Ultrathin Films

The cleaning of solid substrates, such as Si wafers, quartz glass slides, and indium-doped tin oxide (ITO)-coated glasses was carried out according to the previously described procedures. [6] Ultrathin films were fabricated by applying the LBL assembly procedure as follows: the substrates were precoated with PEI by immersion in an aqueous solution of PEI (2.5 g dm^{-3}) at pH = 9 for 20 min and then the PEI-primed substrates were dipped in a colloidal suspension (0.01–0.16 g dm^{-3}, pH = 8) of MnO_2 nanosheets for 20 min, followed by water washing. Then the substrate was immersed in a solution of PDDA (pH = 9, 20 g dm^{-3}) for 20 min and washed with water again. The above procedure was repeated for a desired number of cycles to obtain multilayer films of PEI/MnO_2/(PDDA/MnO_2)$_{n-1}$.

2.3 Characterizations

Ultraviolet-visible (UV-vis) absorption spectra were collected using a Hitachi U-4000 spectrometer equipped with an integrating sphere detection system. The surface topography of the monolayer films was examined using a Seiko SPA400 atomic force microscope (AFM) in tapping mode with silicon-tip cantilevers (20 N m^{-1}). X-ray diffraction (XRD) data were acquired by a Rigaku Rint 2000 powder diffractometer with Cu Kα radiation. Fourier transform infrared (FT-IR) spectra were measured with a Digilab S-45 spectrometer in transmission mode. X-ray photoelectron spectra (XPS) were recorded on a Physical Electronics XPS-5700 spectrometer with Al Kα X-ray line (1486.6eV). X-ray absorption near edge spectra (XANES) were obtained with synchrotron-radiated X-ray using an extended X-ray absorption fine-structure facility installed at beam line 12c at the photon factory in Tsukuba, Japan. Cyclic voltammograms (CV) were measured in a three-electrode glass-cuvette cell using a Solartron SI-1287 computer-controlled potentiostat. Thin films assembled on the ITO-coated glass slide were used as working electrodes. An Ag/Ag^+ (0.49 V vs. standard hydrogen electrode) electrode and a glassy carbon were used as reference and counter electrodes, respectively. CV experiments were performed from −1.3V to 0.9V at a scan rate of 5–200 mV s^{-1} using 0.1 mol dm^{-3} $LiClO_4$ in propylene carbonate (PC) as electrolyte with N_2 gas bubbling.

3 Results and Discussion

3.1 LBL Assembly of Multilayer Films

The growth of self-assembled thin films was initiated by coating a substrate with cationic PEI, followed by alternate adsorption of colloidal oppositely charged MnO_2 nanosheets and PDDA. The deposition parameters are of importance for the fabrication of multilayer films with a well-defined architecture. Optimum deposition conditions of PEI and PDDA for film fabrication, such as pH value, duration time and concentration, have been well established; [6] we therefore

examined the effect of the suspension conditions of MnO_2 nanosheets on the film growth. The film growth can be monitored by UV-vis spectra. Polyelectrolytes of PEI and PDDA gave negligible UV-Vis spectral contribution, while a broad absorption band centered at around 375 nm after the adsorption of MnO_2 nanosheets was observed, which is the feature of delaminated MnO_2 nanosheets. [17] Figure 1 presents the influence of suspension concentration of MnO_2 nanosheets on the UV-Vis peak-top absorbance after the deposition of the first PEI/MnO_2 bilayer. The absorbance of MnO_2 increased with increasing the MnO_2 suspension concentration up to 0.08 g dm^{-3}. Further increment of the concentration did not lead to apparent enhancement of UV absorbance, suggesting a similar amount of MnO_2 deposited on the substrate surface in this concentration range. The pH value of MnO_2 suspension is another important factor for film fabrication. Our experimental results revealed that pH value of 8 led to a maximum optical absorbance of MnO_2. Consequently, the MnO_2 concentration of 0.08 g dm^{-3} and pH = 8 were selected for the deposition of films.

Figure 2 shows topographic image of the first deposited layer of MnO_2 nanosheets on a PEI-coated surface of Si wafer. PEI themselves were not perceptible. The surface was covered with irregularly shaped sheet-like crystallites with lateral size ranged from 100 to several hundreds of nanometers. The surface coverage of nanosheets is about 88 % with some overlapping area. A section analysis revealed their molecular nature, showing an average thickness of ca 0.80 nm.

The progressive growth of multilayer films under the optimized conditions was examined by UV-vis adsorption measured after each deposition cycle. The nearly linear increment of peak-top absorbance suggests that a nearly equal amount of MnO_2 nanosheets was deposited in each coating cycle (Figure 3), indicating the successful LBL assembly of multilayer ultrathin films of

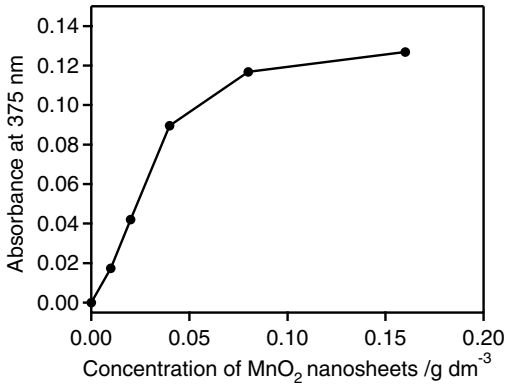

Figure 1: UV-vis absorbance at 375 nm of the first PEI/MnO_2 bilayers as a function of MnO_2 nanosheet concentration. Concentration of PEI solution: 2.5 g dm^{-3}; pH value of solution: pH = 9 for PEI, and pH = 8 for MnO_2 nanosheets; deposition time: 20 min each.

MnO_2. A total absorbance of ca. 0.95 after deposition of 10 bilayers on both sides of quartz was attained. The LBL growth of the multilayer films was also examined by XRD measurements. A broad Bragg peak centered at $2\theta = 9.6^{o}$ for the ultrathin films deposited on quartz glasses was detected after numbers of deposition cycles and its peak intensity enhanced progressively with increasing assembly cycles (Figure 4). This feature can be principally explained by the superlat-

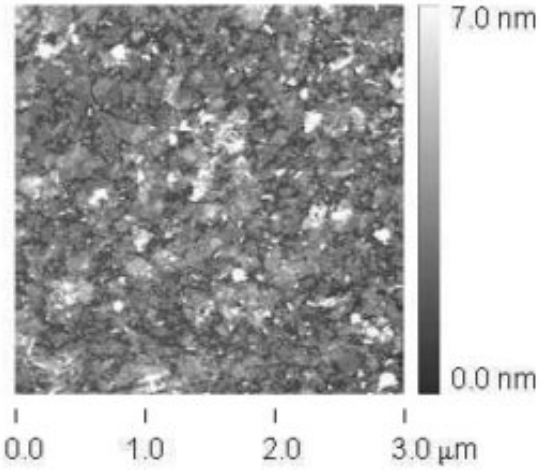

Figure 2: Tapping-mode AFM image of MnO_2 nanosheets deposited on PEI pre-coated Si wafer. Nanosheet concentration: 0.08 g dm^{-3}; pH value of solution: pH = 9 for PEI, and pH = 8 for MnO_2 nanosheets; dipping time: 20 min each.

tice reflection of inorganic-organic repeating layer pairs of PDDA/MnO_2. The multilayer repeating distance was about 0.92 nm. Considering the MnO_2 nanosheets has a crystallographic thickness of 0.52 nm, [17] the thickness of the PDDA layer should be ca 0.4 nm. This thickness is reasonable for PDDA layers in film systems. [6]

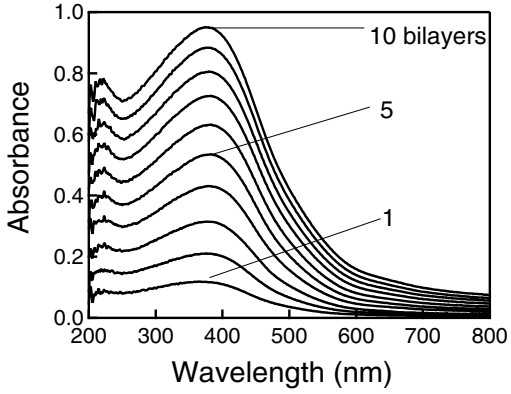

Figure 3: UV-vis absorption spectra of multilayer films of PEI/MnO_2/$(PDDA/MnO_2)_{n-1}$ prepared on quartz glass substrate. Nanosheet concentration: 0.08 g dm^{-3}; pH value of solution: pH = 9 for PEI and PDDA, and pH = 8 for MnO_2 nanosheets; deposition time: 20 min for each.

3.2 Characterizations of the Films

The inorganic component of Mn in the film was examined by XANES studies (Figure 5). Strong absorption in the main-edge region of the Mn K-edge spectra can be assignable as the dipole-allowed transitions from the core 1s level to unoccupied 4p states. [18] The multilayer film

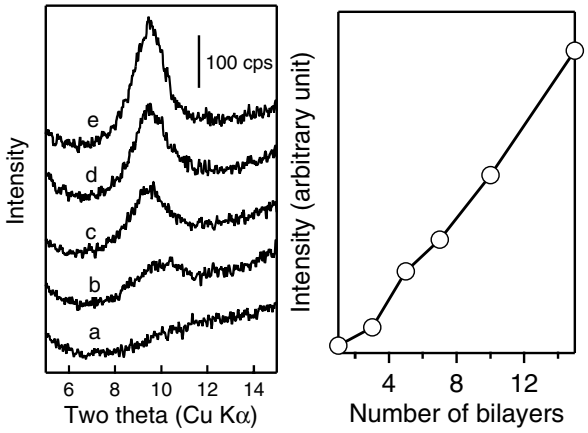

Figure 4: XRD patterns of (a) as-prepared multilayer thin films of PEI/MnO_2/(PDDA/ $MnO_2)_{n-1}$ and (b) their peak intensity as a function of bilayer number. Here, *n* is 1 for (a), 3 for (b), 5 for (c), 10 for (d), and 15 for (e), respectively.

exhibited an edge energy of ~ 6558 eV, which is nearly the same as that for the reference MnO_2, but apparently different from that for Mn_2O_3. This suggests that the oxidation state of manganese in nanosheets is close to that in $Mn^{IV}O_2$. FT-IR spectra for the multilayer films (see Figure 6) provided the evidence for organic species in the films. The bands at 1356, 1467, 2866, 2930, 2960, and 3036 cm^{-1} are assignable to the $–CH_2$ and $–CH_3$ groups for PDDA or PEI. [19] A sharp bending vibration of water at ca. 1605 cm^{-1} together with a broad band centered at around 3450 cm^{-1} suggests the presence of hydrated water in the film.

The composition of a thin film of PEI/MnO_2(PDDA/$MnO_2)_9$ was examined by XPS studies. The survey scan spectra for the film exhibited peaks assignable to Mn (653.7 eV for Mn $2p_{1/2}$ and 641.8 eV for Mn $2p_{3/2}$), C (284.9 eV for 1s), N (401.8 eV for 1s) and O (530.5 for 1s) [20] (Figure 7). Quantitative analysis indicated the atomic ratio: C, 32.1 %. N, 2.5 %; Mn, 20.6 %; O, 41.1 %. The Mn/O ratio of 1.99 is in excellent agreement with the stoichiometry of MnO_2. On the other hand, the C/N ratio deviated from the theoretical value of 8 for PDDA molecules, which can be due to the contamination of surface carbon as often observed in XPS analysis. [21]

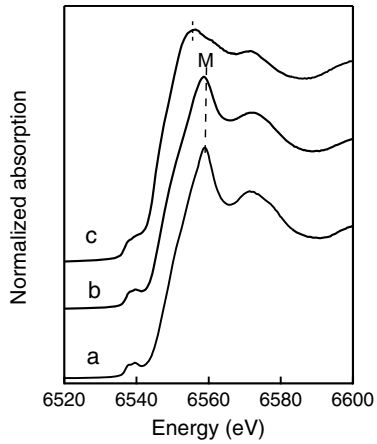

Figure 5: Mn K-edge XANES spectra for (a) as-prepared thin film of PEI/MnO_2/(PDDA/MnO_2)$_9$, references (b) MnO_2 and (c) Mn_2O_3. M represents main peak in XANES

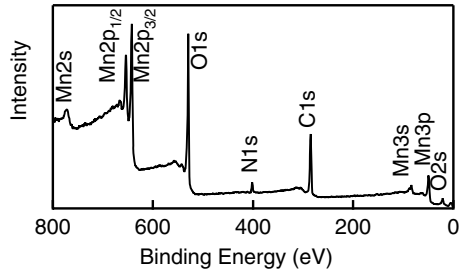

Figure 6: FT-IR spectra for an as-prepared multilayer thin film of PEI/MnO_2/(PDDA/ MnO_2)$_9$. The circles represent the signals arising from PDDA or PEI.

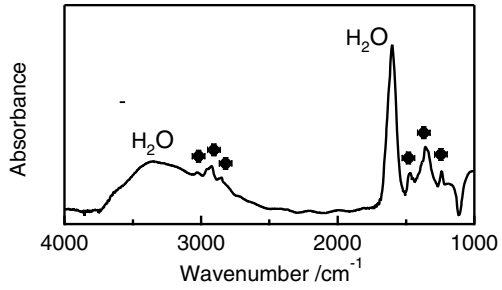

Figure 7: Survey XPS data for an as-prepared multilayer thin film of PEI/MnO_2/(PDDA/MnO_2)$_9$

3.3 Electrochemical Properties

CV measurements started from the rest potential (E_{Ag/Ag^+} = –0.1–0.1 V) to a negative direction. The CV of a monolayer electrode (Figure 8a) revealed a reduction peak at –0.66 V vs. Ag/Ag^+ on the negative scan and two oxidation peaks at –0.36 V and 0.23 V vs. Ag/Ag^+ on the positive scan, indicating that the nanosheet film undergoes reduction reaction in one step and oxidation process in two steps. The peak current increased linearly with increasing scan rate from 5 mV s^{-1} to 100 mV s^{-1}, as is shown in Figure 8b, suggesting that the electroactive species adsorbed on the electrode, i.e. MnO_2 nanosheets, are responsible for the redox processes. The quantitative electron transfers were estimated to be (1.7–1.8) $\cdot 10^{-9}$ mol cm^{-2} for both the oxidation and the reduction reactions derived from the integrated peak areas of Figure 8a. Assuming the electrode surface was covered with a perfect monolayer, a deposited amount of the nanosheets is estimated to be ~ 2.1 $\cdot 10^{-9}$ mol cm^{-2}. [22] This value is close to that for the calculated electron transfers during CV, indicating that predominated manganese oxide on the electrode should be electroactive. These redox peaks should be attributable to the electrochemical conversion between Mn^{IV} and Mn^{III} in the film. To our knowledge, this should be the first example to provide the CV characteristic of the fundamental units of layered manganese oxides, which should be of importance for the further understanding of electrochemical behavior for low-dimensional nanomaterials.

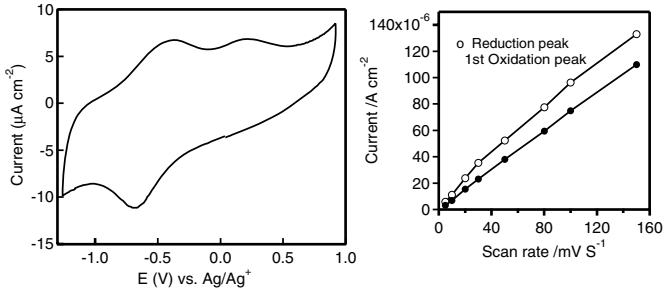

Figure 8: (a) Cyclic voltammogram (scan rate: 10 mV s^{-1}) and (b) scan rate dependence of monolayer films of PEI/MnO_2 on ITO glass slide in 0.1 mol dm^{-3} $LiClO_4$/PC electrolyte (potential range: –1.3V–0.9V; second cycle).

4 Conclusions

Multilayer ultrathin films composed of novel manganese oxide nanosheets and polyelectrolytes have been successfully fabricated on flat substrates using the alternate LBL procedure. Characterizations support the well-defined architecture of hybrid nanocomposite films. Cyclic voltammogram data demonstrated the electrochemical redox behavior of the MnO_2 nanosheets.

5 References

[1] J. Z. Zhang, Z. L. Wang, J. Liu, S. W. Chen, G. Y. Liu, Self-Assembled Nanostructures, Kluwer Academic/Plenum Publisher: New York. 2003

[2] J. H. Fendler, Nanoparticles and Nanostructured Films: Preparation, Characterization and Applications, Wiley Publisher, 1998

[3] G. Decher, Science 1997, 277, 1232–1237

[4] T. Cassagneau, J. H. Fendler, T. E. Mallouk, J. Am. Chem. Soc. 1998, 120, 7848–7859

[5] F. Caruso, H. Mohwald, J. Am. Chem. Soc. 1999, 121, 6039–6046

[6] T. Sasaki, Y. Ebina, T.Tanaka, M. Harada, M. Watanabe, Chem. Mater. 2001, 13, 4661–4667

[7] Y. F. Shen R. P. Zerger, R. N. DeGuzman, S. L. Suib, L. MaCurdy, D. I. Potter, C. L. O'Young, Science 1993, 260, 511–514

[8] Q. Feng, H. Kanoh, K. Ooi, J. Mater. Chem. 1999, 9, 319–334

[9] A. R. Armstrong, P. G. Bruce, Nature 1996, 381, 499–500

[10] S. R. Segal, S. H. Park, S. L. Suib, Chem. Mater. 1997, 9, 98–104

[11] T. E. Mallouk, J. A. Gavin, Acc. Chem. Res. 1998, 31, 209–217

[12] J. W. Long, L. R. Qadir, R. M. Stroud, D. R. Rolison, J. Phys. Chem. B 2001, 105, 8712–8717

[13] S.-C. Pang, M. A. Anderson, T. W. Chapman, J. Electrochem. Soc. 2000, 147, 444–450

[14] H. Kanoh, W. P. Tang, Y. Makita, K. Ooi, Langmuir, 1997, 13, 6845

[15] Y. Ratieuville, W. L.Wu, D. Lincot, J. Vedel, L. T. Yu, J. Electrochem. Soc. 1999, 146, 3161–3167

[16] Y. Lvov, B. Munge, O. Giraldo, I. Ichinose, S. L. Suib, J. F. Rusling, Langmuir, 2000, 16, 8850–8857

[17] Y. Omomo, T. Sasaki, L. Z. Wang, M. Watanabe, J. Am. Chem. Soc. 2003, 125, 3568-3575

[18] T. Ressler, S. L. Brock, J. Wong, S. L. Suib, J. Phys. Chem. B 1999, 103, 6407–6420

[19] G. Socrates, Infrared Characteristic Group Frequencies; 2nd ED.; John Wiley & Sons: Chichester, 1994

[20] J. Moulder, W. Stickle, P. Sobol, K. Bomben, Handbook of X-ray Photoelectron Spectroscopy; Chastain, J., Ed; Perkin-Elmer Corp.: Eden Prairie, MN, 1992

[21] T. Sasaki, Y. Ebina, K. Fukuda, T. Tanaka, M. Harada, M. Watanabe, Chem. Mater. 2002, 14, 3524–3530

[22] The MnO_2 nanosheet has a two-dimensional hexagonal unit cell (a ~ 0.3 nm) that contains one formula weight of MnO_2. The unit cell area S_{uc} is 0.078 nm^2 (= 0.3 · 0.3 · sin 120°). Accordingly, the deposited amount M can be calculated as: $M = 1/(N_a \cdot S_{uc})$, where N_A is Avogadro's number.

Generation of Nanostructured Materials from Thin Films of Block Copolymer Assembles

A. Sidorenko*[1], I. Tokarev[1], R. Krenek[1], Y. Burkov[2], D. Schmeisser[2], S. Minko[3], M. Stamm[1]
[1]Institut für Polymerforschung, Dresden, Germany
[2]Brandenburgische Technische Universität, Cottbus, Germany
[3] Department of Chemistry, Clarkson University, Potsdam, USA

1 Introduction

Methods of fabrication of ordered arrays of nanowires/nanorods are in the focus of many investigations. Such nanostructures are considered to be of significant interest for both fundamental and application aspects. Several approaches have been proposed based on the self-organization phenomenon.[1–3] Anodic porous alumina films have been shown to be effective template for electrodeposition of Ni, Co, Fe and Ag.[4–6] Depending on the anodization conditions, they demonstrate pores diameter on the range of 20–200 nm and ordered crystal-like domains spatially extended over 20–100 periods. One significant drawback of the alumina templates is the presence of thin insulating layer of Al_2O_3. To overcome this luck, the impulse electrodeposition regime was successfully applied. In the course of the investigation, several helpful empirical rules and electrochemical regimes were developed to improve the quality of the nanowire arrays.[4, 5]

An elegant method of fabrication of arrays of nanodots was proposed by Möller et. al.[7–9] They explored the micellization of block copolymers (BC) to form a layer of ordered nanoparticles on solid substrate. Successive conversion of BC nanostructured layer leads to nanopatterning of the substrate surface and can be used for fabrication of the nanodots [10].

Thurn-Albrecht et. al. convincingly demonstrated several examples of nanowires preparation using self-organization in thin films of poly(styrene-b-methyl methacrylate) (PS-PMMA) [11, 12]. They used external electric field to align the cylinders of minor block (PMMA) of asymmetrical PS-PMMA block copolymer in the direction perpendicular to the substrate plane and etched the PMMA cylinders selectively with UV light. Obtained template films of about a micron thickness were loaded with Co via electrochemical deposition in DC regime. Also, the BC based templates were loaded via sputtering with clusters of Cr and Au resulting in arrays of Cr and Au/Cr nanodots. Magnetization measurements undoubtedly demonstrated the effect of ordering and orientation of nanowires/nanodots of ferromagnetic material [11].

Recently, we have published the results of the investigation of self-organization in thin films of BC supramolecular assembly (SMA). Based on the O. Ikkala approach [13, 14], we have synthesized SMA from poly(styrene-b-4-vinylpyridine) (PS-PVP) using hydrogen bonding of low molar mass additive (2-(4'-hydroxybenzeneazo)benzoic acid, HABA) with pyridine fragment of PVP (Figure 1) [15]. The SMA demonstrates ability to form smooth thin films on solid substrate. PS-PVP+HABA is able to fast self-organization via vapor annealing in non-selective solvent (1,4-dioxane) with perpendicular alignment of hexagonally packed cylinders of minor component (PVP+HABA) dispersed in the matrix of PS. Another important feature of the PS-PVP+HABA system is insensitivity in respect to the substrate surface. We have obtained nicely

structured films on polar (Si/SiO_2), metal (Cr, Cr/Au, Ni) and non-polar (poly(1,2-butadiene), PBd) surfaces. Moreover, rinse of thin films of the SMA in selective for HABA solvent results in ordered array of channels oriented perpendicularly to the substrate plane.[15] In this contribution, we present the results of electrochemical deposition through the nanotemplate prepared from SMA thin films and discuss fine details of metal electrodeposition in nanopores.

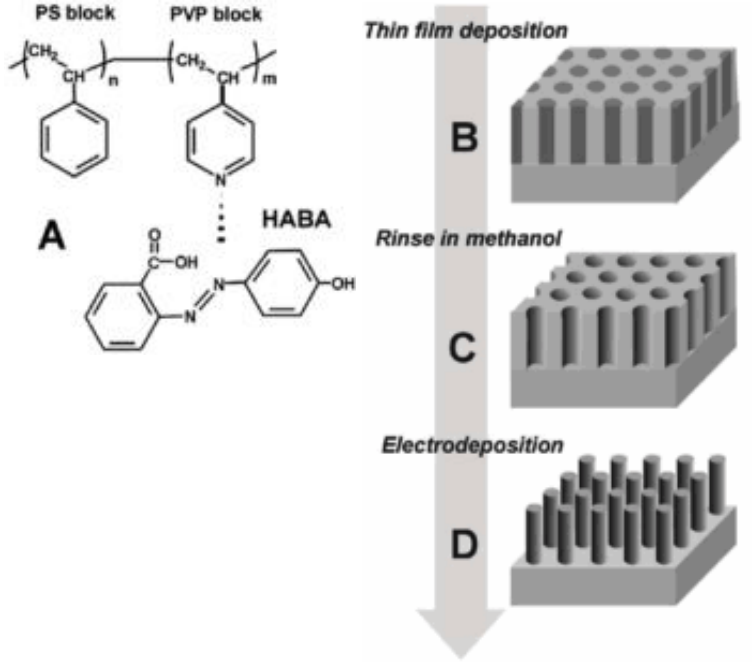

Figure 1: The SMA based approach for metal nanowire array fabrication: chemical composition (a), microphase separation in thin films of SMA (b), nanotamplate (c), array of nanowires/nanorods

2 Experimental Section

2.1 Materials

Poly(styrene-*block*-(4-vinylpyridine)) (PS-PVP) with number average molecular masses (M_n) : PS 35500 g/mol, PVP 3680 g/mol, $M_w / M_n = 1.06$ for both blocks, was purchased from Polymer Source, Inc. 2-(4'-hydroxybenzeneazo)benzoic acid (HABA) was purchased from Sigma-Aldrich. Solvents – 1,4-dioxane, chloroform, THF, toluene, methanol, dichloromethane – were purchased from Acros Organics and used as is. Silicon wafers {100} and {111} were cleaned successively in an ultrasonic bath (dichloromethane) for 15 min and "piranha" bath (30 % H_2O_2, 70 % of H_2SO_4, *chemical hazard*) for 40 min at 82 ºC, then thoroughly rinsed with Millipore water and dried in argon flow.

2.2 Fabrication of Nanotemplates

PS-PVP and HABA (1 mole HABA : 1 mole 4-vinylpyridine monomer unit) were dissolved separately. Then PS-PVP solution was drop-by-drop added to HABA solution, while heating close to the boiling point of the solvent in ultrasonic bath. The heating was very important for the reproducible formation of SMA. The resulted solution (the range of the total concentration PS-PVP + HABA from 0.1 % to 3 % wt., the fraction of HABA 17.8 % wt.) was kept overnight to complete hydrogen bonding. Thin films were prepared by dip-coating from the filtered solutions. Dip-coating was performed with the rates ranging from 0.1 to 1.0 mm/s. The "vapor annealing" was performed for 10–20 min to improve the ordering in the SMA films. Nanotemplates were fabricated by selective extraction of HABA with methanol.

2.3 Characterization of the Ordered Thin Films

Thickness of the polymer films was measured by a SE400 ellipsometer (SENTECH Instruments GmbH, Germany) with 632.8 nm laser at 70º incident angle.

AFM imaging was performed by a Dimension 3100 (Digital Instruments, Inc., Santa Barbara) scanning force microscope and a CP (Park Scientific Instrument, Inc) in the tapping mode. The tip characteristics are: spring constant 1.5–3.7 N/m, resonant frequency 45÷65 Hz, tip radius about 10 nm.

2.4 Templating of Nanomembranes

Nickel electrodes have been prepared via successive sputtering of Cr as adhesive layer (5 nm thick) and Au layer (30–50 nm thick). Ni films of 30nm thick were deposited on top of Au electrodes by electrodeposition in galvanostatic regime using Watts bath as described elsewhere. Chromium electrodes were prepared via direct sputtering of 30nm thick Cr layer onto Si wafers. Both Cr and Ni depositions reveal low roughness (rms roughness less then 2 nm on 1 μm^2). A sputter-coater by Tectra GmbH (Germany) was used. Si{111} doped wafers were used without modification showing atomically smooth surface (less then 0.2 nm on 1 μm^2 rms roughness) and high enough electroconductivity. Ni was loaded into the cylindrical channels of the membrane via electrodeposition in the galvanostatic mode using an Autolab/PGSTAT30 with the Watts bath, an Ag/AgCl reference electrode, and a platinum wire counter electrode.

2.5 X-ray Photoelectron Emission Microscopy

X-ray photoelectron emission microscopy (XPEEM) and Near Edge X-ray Absorption Fine Structure (NEXAFS) spectroscopy measurements were performed at Berlin Synchrotron Source (BESSY II). The spectromicroscopic characterization by PEEM was performed with a FOCUS-IS PEEM (Omicron). The setup was equipped with a CCD camera. The camera total intensity is used to record the NEXAFS signal which in principle can be used to obtain local spectroscopic information from the PEEM images as this information can be collected pixel re-

solved (μ-NEXAFS). The instrument is operated at the BESSY-U49/2 beam line which provides energies in the range of 100 ÷ 1200 eV with an energy resolution of approximately 0.1 eV.

3 Results and Discussion

AFM imaging of SMA templates based on thin films PS-PVP+HABA undoubtedly demonstrates nice ordering of hexagonally packed channels oriented perpendicularly to the substrate surface (Figure 2). The channels of 8–10 nm are equally distributed over the entire film surface with periodicity of 25 nm. However, the fine structure of the template at the polymer-substrate interface remains uncovered while the AFM tip penetration into the channels is limited by the tip and pore geometry and typically is less then the template film thickness (5–10 nm penetration depth and 20–100 nm film thickness). Also, ellipsometry analysis of the templates with hollow channels gives evidence of the porous structure of the films. In deed, two parameter optimisation of ellipsometry data in the frame of two-layer model (Si/SiO_2/polymer) gives the effective refractive index of the polymer layer n = 1.49–1.53. The n value is sufficiently lower then the refractive index of PS-PVP (1.59). Applying the Bruggeman model for assymetrical porous nanostructures, we estimated the pore fraction in the thin polymer films from the effective refractive index n measured with ellipsometry using the following equation: [16]

$$\left(\frac{\varepsilon_{\text{eff}} - \varepsilon_1}{\varepsilon_2 - \varepsilon_1}\right)\left(\frac{\varepsilon_2}{\varepsilon_{\text{eff}}}\right)^{1/3} = 1 - f$$

where ε_{eff}, ε_1 and ε_2 are dielectric constants of the entire film (effective), pore material, and matrix material, respectively, $\varepsilon_i = n_i^2$, and f is the volume fracture of the pores. The estimated volume fraction of the pores in the membrane f is on the range of 0.099–0.165. It is lower then the concentration of HABA in the initial mixture (17.8 %). One of the reasons of this disagreement

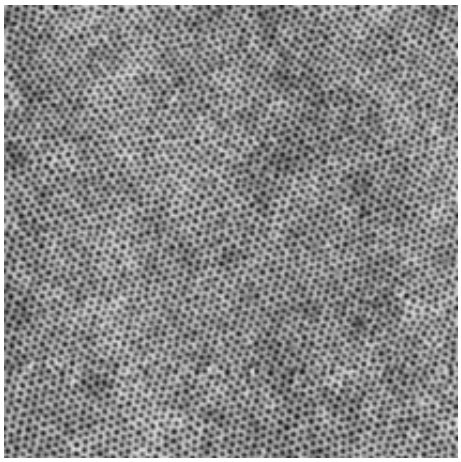

Figure 2: AFM image of nanotemplate from PS-PVP+HABA thin (40 nm) film after methanol rinse. Lateral scale 1.5 × 1.5 μm^2, vertical scale 20 nm.

is presence of disordered polymer layer as found for many BC thin films. Thus, neither ellipsometry nor AFM of the SMA templates gives reliable information on the substrate-polymer interface. Meanwhile, the structure of this interface is a key question of SMA film application as templates for nanodots/nanowires fabrication. We have performed the series of direct experiments with electrodeposition of metal through the SMA templates to clarify the situation.

First, we started with Ni electrodes covered with the SMA template obtained as described above. We optimized the conditions of electrodeposition in terms of current density and deposition time. Figure 3 shows the array of Ni nanorods obtained in galvanostatic regime at 0.3 mA/cm^2 current density for 1000 sec. The deposition potential reveals only minor changes during the electrodeposition in the range of –0.75V to –0.79V. Hexagonally aligned rods of 10–20 nm high are clearly seen as well as some fraction of lacunas. Using flooding procedure applied to AFM images of the deposition, we found the lacuna surface fraction in the range of 5–20 %. At the same time, the micron size Ni clusters are scattered over the surface. The similar results were obtained on Cr electrodes covered with the SMA template. It is worth to note that increase of deposition time or current density results in sufficient increase of Ni clusters of several micron size on top of the nanotemplate.

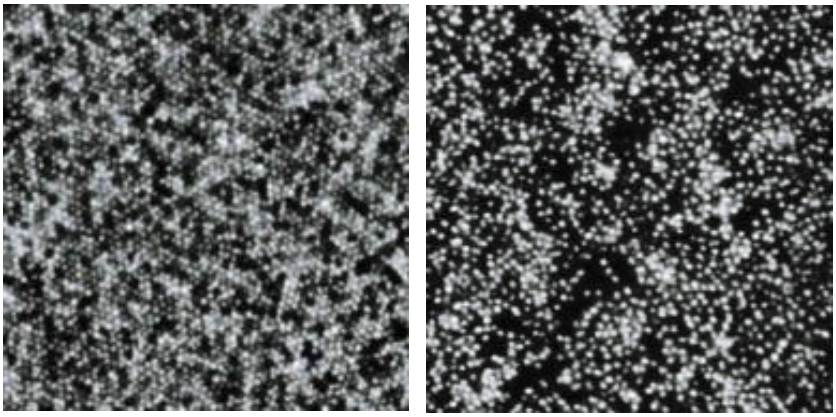

Figure 3: AFM image of Ni nanorods electrodeposited through SMA nanotemplate on Ni (top) and Si{111} electrodes. SMA template is removed. Lateral scale 1.5 × 1.5 μm^2, vertical scale 20 nm.

Also, we performed electrochemical deposition of Ni through the SMA nanotemplate on Si{111} electrode. The deposition potential varies during deposition on the range of –1.0 V to –1.05V at 0.3 mA/cm^2 current density applied in DC galvanostatic regime. We explain the overpotential increase as compared with Ni electrode by presence of thin film of SiO_2 native layer interfering the electrodeposition in DC regime. We believe this is the reason why electrodeposition in DC regime results in very rough covering consisted of Ni clusters of micron size. In deed, nucleation rate is much lower then growth and overpotential value is higher in case of insulating thin layer on top of the electrode. It results in fast growth of rare clusters and overload of the separated nanotemplate channels as described in details elsewhere [17]. To overcome the effect of insulating SiO_2 layer, we applied impulse galvanostatic regime as proposed by Gösele et. al. [4]. We modified the AC galvanostatic deposition parameters for thin nanotemplates and

optimized the condition. The impulse galvanostatic deposition was performed at the conditions as shown on the Table 1. The resulting Ni nanostructure on Si{111} is shown on Figure 3. Ni nanodots of 5–20 nm high are clearly seen as well as sufficient surface lacunas. The estimation of lacuna surface with flooding procedure gives the lacuna fraction on the range of 40–60 %.

Table 1: Parameters of impulse electrodeposition of Ni on Si{111}. 50 scans performed

Step	Current density, mA/cm^2	Step duration, sec	Potential, *V*
1	–5.0	0.02	–5.0 ÷ –5.5
2	2.0	0.01	3.0 ÷ 3.5
3	0.0	0.97	–0.45 ÷ –0.55

The comparison of Ni electrodeposition conditions and morphology of nanostructures obtained on Ni and Si{111} demonstrates the effect of thin insulating layer on the deposition process. In order to visualize the found effect, we performed Ni electrodeposition onto mosaic Cr electrode partially covered with insulating layer of poly(1,2-butadiene) (PBd). For that, thin film of PBD with addition of 5% of photoinitiator, i.e. benzophenon, was spin-coated onto Cr covered wafer and illuminated with UV light (365 nm mercury lamp) through TEM grid of 12 μm periodic square pattern. After washing with toluene, the 60 nm thick cross-linked PBD squares were revealed with large scale AFM (Figure 4a). Micromapping ellipsometry showed that the shadowed location is free Cr surface. We deposited the SMA thin (70 nm) film on top of Cr mosaic electrode and completed it into nanotemplate with methanol rinse. Afterward, we performed Ni electrodeposition through the nanotemplate in galvanostatic DC regime (0.3 mA/cm^2, 1000 s) as described above and removed the polymer template in nonselective solvent (chloroform). Obtained samples were investigated with AFM and XPEEM. The AFM image is shown on Figure 4b. It demonstrates PBd film squares with space between them covered with Ni nanorods. Also, there are several clusters of Ni of micron size and lacunas rarely seen on the Ni covering.

The NEXAFS measurements of Ni deposition were performed prior the XPEEM measurements to find the exact Ni2p bonding energy as well as the peak width. The result of subtraction of XPEEM images before (851.5 eV) and after (854.0 eV) Ni2p peak from the image required at the Ni2p peak (853.0 eV) is shown on the Figure 4c. It undoubtedly demonstrates distribution of Ni in the space between the PBd masked electrode surface. Thus, we obtained two scale hierarchy patterning combining electrode photolithography with insulating layer and nanotemplating.

4 Conclusions

Based on the phenomenon of microphase separation in thin films of SMA, we fabricated nanotemplates with hexagonally ordered channels aligned perpendicular to the substrate surface. We demonstrated that the nanotemplates are able to be loaded with metals, e. g. Ni, via electrodeposition to form arrays of ordered metal nanorods. Using Si{111} electrodes with thin insulating layer of SiO_2, we found sufficient increase of the Ni^{2+}/Ni overpotential value. It results in very unequal deposition condition. However, the deposition in impulse regime allows to over-

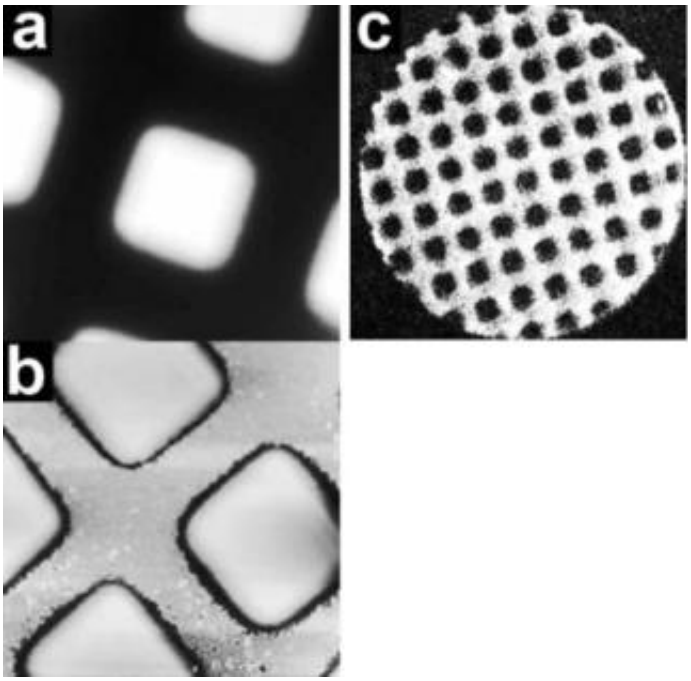

Figure 4: AFM images of PBd masked Cr electrode before (a) and after (b) Ni templated deposition, lateral size 25 × 25 μm^2, vertical scale 70 nm, and XPEEM image with Ni2p contrast (c), 120 × 120 μm^2 lateral scale

come partially the effect of insulator layer. Also, we performed electrodeposition of Ni onto the electrode covered with micron insulating polymer mask followed with nanotemplate and obtained two scale hierarchy pattern of Ni nanorods.

5 Acknowledgement

BMBF (grant 05KS1BPA/4) is gratefully acknowledged for financial support.

6 References

[1] I. W. Hamley, Nanotechnology 2003, 14, R39

[2] H.X. He, N.J. Tao, Electrochemical fabrication of metal nanowires in Encyclopedia of Nanoscience and Nanotechnology, Eds., N.S. Nalwa, American Scientific Publishers, in press, 2003

[3] J. C. Hulteen, C. R. Martin, Template Synthesis of Nanoparticles in Nanoporous Membranes, in Nanoparticles in Solids and Solutions. Ed.: J. Fendler, Willey, 1998, Chapter 10, p. 235–260

[4] K. Nielsch, F. Müller, A.-P. Li, U. Gösele. Adv. Mater. 2000, 12, 582–586

[5] a) J. Choi, K. Nielsch, M. Reiche, R.B. Wehrspohn, U. Gösele, J. Vac. Sci. Technol. B 2003**,** 21, 763
b) G. Sauer, G. Brehm, S. Schneider, K. Nielsch, R. B. Wehrspohn, J. Choi, H. Hofmeister, U. Gösele, J. Appl. Phys. 2002**,** *91,* 3243
c) K. Nielsch, R. B. Wehrspohn, S. F. Fischer, H. Kronmüller, J. Barthel, J. Kirschner, T. Schweinboeck, D. Weiss, U. Gösele, MRS Symp. Proc. 2002, *705*, Y9.3.1
[6] a) S.-Z. Chu, K. Wada, S. Inoue, S. Todoroki, Y. K. Takahashi, K. Hono, Chem. Mater. 2002, 14, 4595–4602
b) R. M. Metzger, V. V. Konovalov, M. Sun, T. Xu, G. Zangari, B. Xu, M. Benakli, W.D. Doyle, IEEE Trans. Magn. 2000, 36, 30–35
[7] J. Spatz, S. Mössmer, M. Möller, M. Kocher, D. Neher, G. Wegner, Adv. Mater. 1998, 10, 473
[8] J. P. Spatz, A. Roescher, M. Möller, Adv. Mater. 1996, 8, 337
[9] J. P. Spatz, T. Herzog, S. Mössmer, P. Ziemann, M. Möller, Adv. Mater. 1999, 11, 149
[10] M. Haupt, S. Miller, R. Glass, M. Arnold, R. Sauer, K. Thonke, M. Möller, J.P. Spatz. Adv. Mater. 2003, 15, 829–831
[11] T. Thurn-Albrecht, J. Schotter, G.A. Kästle, N. Emley, T. Shibauchi, L. Krusin-Elbaum, K. Guarini, C.T. Black, M.T. Tuominen, T.P. Russell. Science 2000, 290, 2126–2129
[12] T. Turn-Albrecht, R. Steiner, J. DeRouchey, C. M. Stafford, E. Huang, M. Bal, M. Tuominen, C.J. Hawker, T.P. Russell Adv. Mater. 2000, 12, 787
[13] R. Mäki-Ontto, K. de Moel, W. de Odorico, J. Ruokolainen, M. Stamm, G.ten Brinke, O. Ikkala. Adv. Mater. 2001, 13, 117–121
[14] J. Ruokolainen, R. Mäkinen, M. Torkkeli, R. Serimaa, T. Mäkelä, G. ten Brinke, O.T. Ikkala. Science 1998, 280, 557
[15] A. Sidorenko, I. Tokarev, S. Minko, M. Stamm, J. Am. Chem. Soc. 2003, 125, 12211–12216
[16] D. A. G. Bruggeman, Ann. Phys. 1990, *24*, 636
[17] M. E. T. Morales, V. Buschmann, D. Dobrev, R. Neumann, R. Scholz, I. U. Schuhert, J. Vetter, Adv. Mater. 2001, 13, 62–65

Authors

Subject Index*

* The page numbers refer to the first page of the respecting article